THE EQUATORIAL ELECTROJET: RADAR OBSERVATIONS AND MODELING

A Dissertation

Presented to the Faculty of the Graduate School

of Cornell University

in Partial Fulfillment of the Requirements for the Degree of

Doctor of Philosophy

by

Esayas Belay Shume

August 2006

© 2006 Esayas Belay Shume

ALL RIGHTS RESERVED

THE EQUATORIAL ELECTROJET: RADAR OBSERVATIONS AND MODELING

Esayas Belay Shume, Ph.D.

Cornell University 2006

This dissertation describes a theoretical, experimental, and modeling investigation of the equatorial electrojet. We review low latitude ionospheric current models, synthesizing developments from the early times until the present. We then show how to utilize equatorial electrojet irregularities to infer E region electron density and wind profiles from coherent scatter radar experiments. The procedure involves a numerical model of the equatorial ionosphere that relates the vector electric field and current density to the winds.

We present electron densities inferred in the equatorial electrojet inferred using a new bistatic radar system installed between Paracas and Jicamarca, Perú. The radar system monitors density profiles using a coherent scatter radar technique that utilizes the Faraday rotation of the scattered signal. Radar measured density profiles are validated by comparing with other electron density measures.

A three dimensional electrostatic potential model of the equatorial ionosphere in a magnetic dipole coordinate system is described. The model incorporates realistic ionospheric conductivities, electric fields, winds, and includes anamalous collision effects. The model utilizes bistatic radar measured densities, coherent scatter spectral measurements made at large zenith angles, and electric fields derived from 150 km echo drifts. The model is also constrained by magnetometer

records.

We next present a technique for extracting zonal winds in the equatorial electrojet from the Doppler shifts of type II radar echoes measured by a narrow beam, obliquely oriented antenna at the Jicamarca Radio Observatory. The wind profiles were retrieved by combining the 3-D model with theory and measurements of type II echo Doppler shifts. The amplitude and phasing of the calculated wind profiles are in general agreement with satellite and rocket-borne wind measurements. We have used height varying type I radar echoes and large-scale electrojet irregularities inferred from interferometric imaging to validate wind profiles estimates derived from type II echoes.

BIOGRAPHICAL SKETCH

Esayas Belay Shume joined the graduate school of Cornell University in the Spring of 2002. Before joining Cornell, he has attended the graduate program of the Department of Physics and Astronomy at Clemson University from Fall 2000 to Fall 2001. He has got a Master of Science degree from the Department of Physics, the University of Tromsø (Norway) specializing in Space Plasma Physics. He obtained a Bachelore of Science degree majoring in Physics and minoring in Mathematics from the Department of Physics in the College of Natural Sciences at the Addis Ababa University of his native country, Ethiopia. He has also gotten a Master of Education degree specializing in Physics Education from the School of Graduate Studies of Addis Ababa University.

ACKNOWLEDGEMENTS

I would like to thank members of my Special Committee, Prof. D. L. Hysell, Prof. M. C. Kelley, and Prof. L. D. Brown. My special gratitude goes to my Special Committee Chair, Prof. D. L. Hysell, for his constant support, accessibility, and constructive suggestions throughout my Ph.D. study. His examplary hard work has been a motivation for me. Prof. Hysell thanks for teaching me radar and satellite data analysis, and ionospheric modeling techniques. Many thanks to the director, Dr. Jorge L. Chau, and the staff of the Jicamarca Radio Observatory for their prompt communication and for providing me radar data for my research. I would also like to thank members of the Space Plasma Physics research group at Cornell. Thanks for Girma Hailu and Samson Hagos for their friendship. Thanks to Fabiano Rodrigues for his companionship. The Snee Hall community thanks for your hospitality. Last but not least, I would like to thank my brother Kidanu Belay Shume for his nonstopping prayer and encouragements.

TABLE OF CONTENTS

LIST OF FIGURES

LIST OF TABLES

Chapter 1

Introduction

1.1 Objectives of the dissertation

Volumes of data have been gathered utilizing incoherent and coherent scatter radar techniques with the 50 MHz radar at the Jicamarca Radio Observatory (JRO) in Peru, located at 2° north magnetic latitude (-11.76° geographic latitude, -76.87° geographic longitude). In incoherent scatter mode, the radar routinely measures electron density, electron and ion temperatures, plasma composition, plasma drifts, etc., in the equatorial F region out to $\sim$ 2000 km altitude or more. In coherent scatter mode, the radar relies on scattering from field aligned plasma irregularities. Doppler velocities of equatorial electrojet plasma irregularities, spread F irregularities, and so-called 150 km echoes are among the phenomena observed when the radar operates in coherent scatter mode. Interference from non-thermal fluctuations from the electrojet and spread F makes the application of incoherent scatter radar techniques for extracting ionospheric parameters impossible. Inverting coherent scatter radar data to derive electric fields and other physical parameters is meanwhile difficult due to a lack of understanding of the governing functional relationships between the coherent scatter radar signals and the underlying plasma morphology, dynamics and energetics.

In this dissertation, we show how to utilize equatorial electrojet irregularities to probe the E region ionosphere and to infer physical parameters such as electron density and wind profiles from coherent scatter radar observations. The inferred electron densities and winds are vital inputs for calculating ionospheric conductivities and dynamo fields, respectively. The conductivities and dynamo fields are

themselves vital components of an accurate model of the dynamic structure of the equatorial ionosphere. The inferred winds are also helpful for interpreting so-called type I radar echoes. The broad objective of this dissertation is therefore to integrate coherent scatter radar observations with numerical ionospheric models so as to improve our understanding of the plasma physics of the equatorial ionosphere.

Keeping these broad research strategies in mind, this dissertation addresses the following specific issues pertinent to the structure of the equatorial electrojet region.

1.1.1 Specific goals

Coherent scatter radar returns from equatorial electrojet irregularities are employed to estimate electron density profiles in the equatorial E region. The estimated electron density profiles are then utilized in a three dimensional electrostatic potential model. The 3-D model is forced by parameterized global and local winds and constrained by coherent and incoherent scatter radar data from JRO. The model is then used to infer zonal wind profiles in the equatorial electrojet. The model can be employed to analyze and study electric fields, currents, and plasma irregularities in the equatorial ionosphere comprehensively.

Making use of coherent and incoherent scatter radar observations from the Jicamarca Radio Observatory in combination with a realistic computational model, we will pursue the following objective.

1. Daytime E region electron density profiles derived from a bistatic coherent scatter radar experiment that utilizes the Faraday rotation of the coherently scattered signal are evaluated. As mentioned above, the conventional incoherent scatter radar technique for extracting plasma parameters such as

plasma density, etc., is not applicable due the widespread presence of equatorial electrojet irregularities. Consequently, E region ionospheric parameters have been out of reach of radar remote sensing. Snapshots of E region electron density profiles have been reported in the past in conjunction with rocket experiments. However, their temporal and seasonal variability have not been explored. Here, E region electron density profiles measured by a small, low power bistatic coherent scatter radar operating between Jicamarca (transmitter) and Paracas (receiver) in Peru are reported. The technique for estimating densities is described, and results are summarized.

2. An oblique-looking 50 MHz coherent scatter radar system at Jicamarca with a narrow-beam antenna pattern routinely monitors the equatorial electrojet region and measures Doppler velocities of type I and type II radar echoes. Type I and II radar echoes are generally thought to be signatures of the Farley-Buneman (two-stream) and gradient-drift instabilities, respectively. Theoretically, the Doppler velocities of type II radar echoes are predicted by a linear dispersion relation for gradient-drift instabilities. Experimentally, Doppler velocities of type II radar echoes are measured by the radar system mentioned above at JRO. An electrostatic potential model, combined with the linear dispersion relation for electrojet plasma irregularities and driven by incoherent scatter radar data, is used to predict the Doppler shifts of the type II echoes as a function of background parameters. Here, we present an inversion strategy for extracting zonal wind velocity profiles through an iterative comparison of the radar Doppler measurements with the predicted Doppler shifts. The numerical potential model and the techniques for inferring zonal wind profiles are described.

3. The Doppler shifts of type I radar echoes, with respect to the neutral wind frame of reference, are generally thought to saturate at the ion acoustic speed. This is explained in part by linear theory. In the Earth's frame, where observations of type I radar echoes are carried out, type I Doppler shifts are expected to be further shifted by the line-of-sight projection of the neutral wind velocity. In this dissertation, Doppler shift measurements of electrojet irregularities from the vertically looking Jicamarca antenna and Doppler shifts from the oblique coherent scatter radar are compared with the linear dispersion relation for electrojet instabilities and zonal wind profile estimates to gain physical insights into the spectral characteristics of type I radar echoes.

1.2 Organization of the dissertation

The objectives of the dissertation are presented above. In order to place the study in context, a brief introduction to some fundamental definitions and concepts pertaining to the terrestrial ionosphere (with emphasis on the equatorial ionosphere) is presented in Chapter 2. Also in Chapter 2, the equatorial E region ionosphere is reviewed. The equatorial electrojet current is described at length. The current, which causes the electrojet medium to be unstable, is derived by treating the plasma as a multi-component fluid and assuming force equilibrium. Global and local sources of dynamo electric fields which drive the electrojet are considered in the derivation. The linear dispersion relation for electrojet plasma irregularities is derived from the two fluid momentum and continuity equations using plane-wave analysis. The Farley-Buneman and gradient drift instabilities as excitation mechanisms for type I and type II radar echoes, short and long wavelength plasma

irregularities, and two-step and wave mode coupling processes are described.

In Chapter 3, various numerical modeling strategies for the equatorial ionosphere are reviewed. The review includes: the thin-shell dynamo model, a two-dimensional flux tube integrated ionosphere model in the magnetic equatorial plane, a three dimensional ionosphere model based on equipotential and electrostatic approximations, etc. The models provide a foundation for the analysis that follows.

In Chapter 4, the use of a bistatic coherent radar system at the Jicamarca Radio Observatory developed for inferring equatorial E region electron density is described. The technique for inferring density profiles is based on the quasilongitudinal approximation of electromagnetic wave propagation in a cold magnetoplasma. The Faraday angle of the coherently scattered signal is analyzed to estimate electron density profiles. The measured density profiles are compared and contrasted with other electron density estimating techniques.

In Chapter 5, an electrostatic potential model of the equatorial ionosphere in magnetic dipole coordinates is described. The computational model is based on the divergence free current condition in a plasma. The model is used to calculate perturbation vector electric fields and currents flowing in the equatorial ionosphere. Using coherent scatter radar data, the three-dimensional model is employed to infer zonal wind profiles in the electrojet region. The calculated wind profiles are compared and contrasted with satellite wind estimates. The temporal behavior of the calculated wind profiles is analyzed vis-á-vis the characteristics of tidal oscillations in the upper atmosphere.

In Chapter 6, type I radar echoes observed at the JRO are compared with the linear dispersion relation for electrojet irregularities and inferred zonal neutral

winds in the equatorial electrojet to gain physical insights into the observed oblique type I Doppler shifts. In Chapter 7, conclusions and future research plans are presented.

1.3 List of reviewed publications

1. Shume, E. B., D. L. Hysell, and J. L. Chau, Zonal wind profiles in the equatorial electrojet derived from phase velocities of type II radar echoes, ***Journal of Geophysical Research (Space Physics)***, *110, A12308, doi:10.1029/2005JA011210*, 2005.

2. Shume, E. B, D. L. Hysell, and J. L. Chau, Electron density profiles in the equatorial E region ionosphere derived from a bistatic coherent scatter radar experiment in Perú, ***Geophysical Research Letters***, *32, L01107, doi:10.1029/2004GL021715*, 2005.

3. Shume, E. B. and D. L. Hysell, Spectral analysis of plasma drift measurements from the *AE-E* satellite: evidence of an inertial subrange in equatorial spread F, ***Journal of Atmospheric and Solar-Terrestrial Physics***, *66, 57 - 65*, 2004.

Chapter 2

Background

2.1 The terrestrial ionosphere

The geospace environment is immersed in incoming electromagetic radiation and streaming particles of solar as well as astrophysical origin. The incident electromagnetic radiation and particles modify the terrestrial environment in a substantial way. Short wavelength components of the radiation (ultraviolet and shorter: wavelengths less than 100 nanometers) ionize atmospheric gases enveloping the Earth and cause plasma production. The radiation penetrates deep toward the surface of the Earth, ionizing and exciting neutral constituents of the atmosphere until the energy of the incoming photons is exhausted. Simultaneously, the plasma produced in the process collides with the neutral gases of the atmosphere, and production of ionization is countered by dissociative and radiative recombination. The resulting net, weakly ionized plasma (coexisting with the geomagnetic field and the neutral atmosphere) surrounding the Earth is referred to as the terrestrial ionosphere. The number density of the ionospheric plasma can range from a thousand to a million plasma particles per cubic centimeter ($[10^3 - 10^6]$ cm^{-3}). In addition, precipitating particles can be a source of ionization and are also known to be vital for exciting the northern (*auroral borealis*) and southern lights (*auroral australis*). These auroral emissions occur in the Earth's high latitude ionosphere (commonly) provided that geophysical conditions are conducive.

At distances more than one-third of the radius of the Earth, the plasma as well as the neutral atmosphere are rarified such that the mean free path of the particles is much larger than the cyclotron radii. Electron and ion mean free paths

are about 10^4 and 10^2 times larger than electron and ion cyclotron radii, respectively, (or equivalently neutral-particle and charge-charge collision frequencies are smaller compared to electron and ion cyclotron frequencies); consequently, the geomagnetic field controls the motion of plasma particles, defining the boundary of the outermost region of geospace known as the terrestrial magnetosphere.

Traversing down from the magnetosphere toward the Earth's surface, the neutral atmospheric concentration rapidly increases (approximately 4 - 6 orders of magnitude larger than the plasma number density at low altitudes), giving rise to frequent plasma-neutral collisions through resonant and non-resonant interactions. At low altitudes, due to frequent plasma-neutral collisions, the neutral atmosphere competes with the geomagnetic field in controlling plasma motion in the ionosphere. These properties define the terrestrial ionosphere.

The dynamics governing the behavior of the terrestrial ionospheric plasma varies considerably with altitude as well as latitude. These issues are addressed in subsequent sections.

2.2 Ionospheric layers

The intensity of ionizing radiation grows exponentially with altitude, whereas, since atmospheric neutral gases are bound by Earth's gravitational attraction, the neutral density decays with altitude. The decline of ionization potential energy and growth of neutral number density with decreasing altitude towards the surface of the Earth produce vertical inhomogeneity in ionization concentration or plasma number density. Conventionally, the ionosphere is vertically labeled according to the letter based taxonomy: the D, E, and F layers. The F region ionosphere includes the altitude region from about 150 km to a third of the Earth's radius and

has a peak plasma number density around about 400±50 km. The F region peak number density has a typical daytime value of about 10^6 cm^{-3} for solar maximum conditions. The E region ionosphere extends from about 80 to 150 km altitude with a decline in ionization below about 120±5 km. Typical E region noon-time peak density can be about 10^5 cm^{-3} at 106 km under solar maximum conditions. The E region ionosphere is the home of large ionospheric current systems and plasma instabilities. The D region ionosphere extends from about 50 to 80 km. The motion of the highly rarified D region plasma is controlled by neutral atmospheric turbulence.

Vertical profiles of electron number density calculated utilizing the International Reference Ionosphere (IRI) model specifications [*National Space Science Data Center*, 2001], are plotted in Figure 2.1 (panel I) and Figure 2.2. The figures show typical daytime profiles for solar minimum and maximum conditions. It is evident from the figures that the plasma density declines during solar minimum conditions. Figure 2.2 is an enlarged version of Figure 2.1, panel I. The IRI model profiles are imperfect but give a general idea of the characteristics of ionospheric parameters. The IRI model specification is an empirical model encompassing data from ionosonde, incoherent scatter radar, rocket, and satellite measurements [*Bilitza*, 1990].

2.3 Ionospheric composition

Typical plasma composition profiles for the Earth's ionosphere are displayed in Figure 2.1, panel II. The compositions were derived from the IRI model. The figure shows how plasma composition in the ionosphere varies with altitude. This inhomogeneity is introduced by different weights of ionospheric species, including

electrons, and by the quasineutrality condition and the resulting ambipolar electric field. Plasma composition depends also on rates of recombinative/radiative chemical processes as well as the intensity of ionizing radiation and ionization cross-sections.

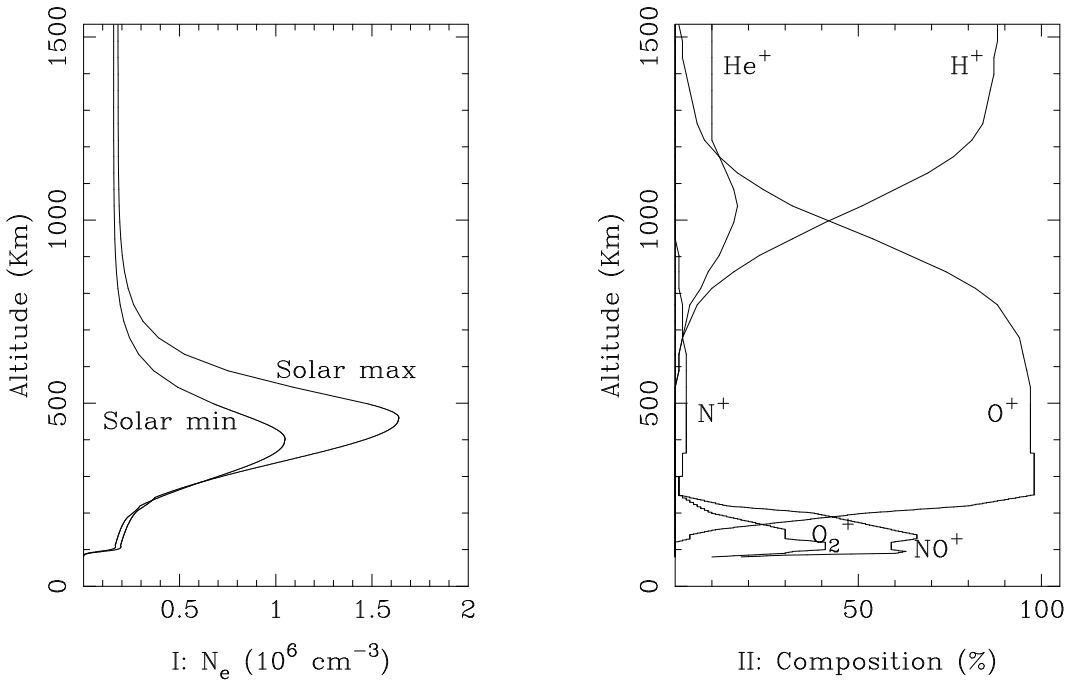

Figure 2.1: I. Electron density profiles for solar maximum and minimum conditions. II. A typical plasma composition profiles. The profiles were derived from the IRI model specification.

The composition between the lower E region and the lower F region is dominated by molecular ion species, namely, O_2^+ and NO^+. An enlarged version of Figure 2.1 (panel II) emphasizing E and bottomside F regions plasma composition is displayed in Figure 2.3. From the lower F region through about 600 km, the ionosphere is mainly populated by atomic oxygen ions, O^+. The reason for

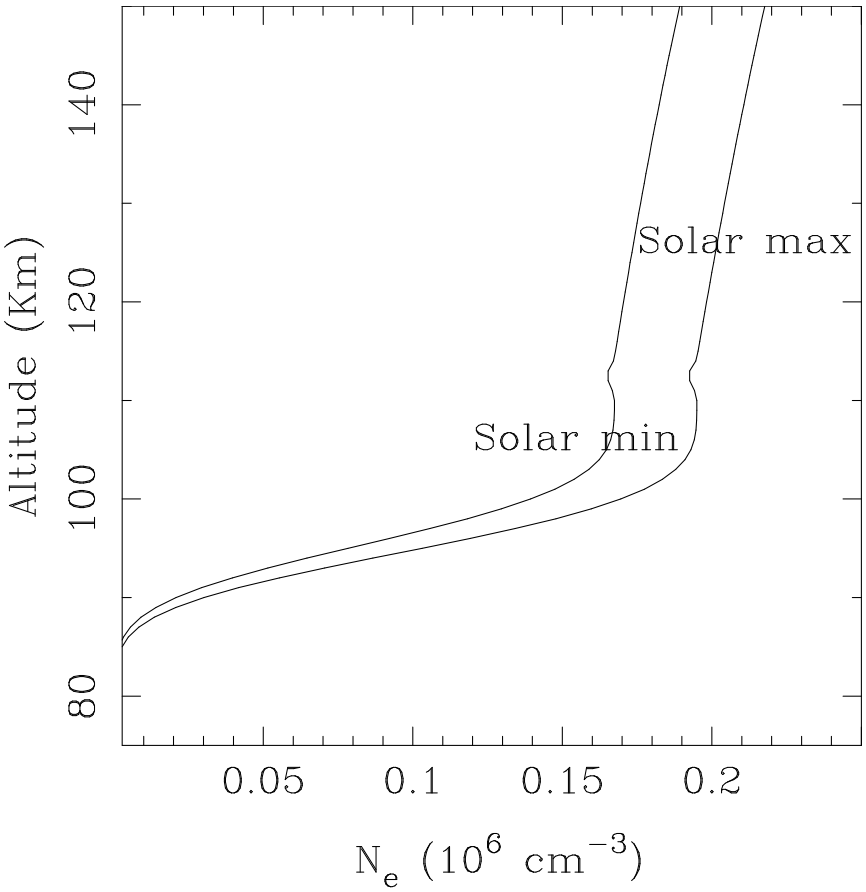

Figure 2.2: Electron density profiles of the E region for solar maximum and minimum conditions. The profiles were derived from the IRI model.

the latter is due to (i) molecular ion species having a larger rate of recombination with electrons than atomic ion species, (ii) the decrease in the molecular number density at those altitudes, and (iii) the availability in larger quantity of the much lighter atomic oxygen, O, for ionization. Above about 600 km and extending to the magnetosphere, the ionosphere is largely a proton plasma, H^+, along with a small fraction of He^+.

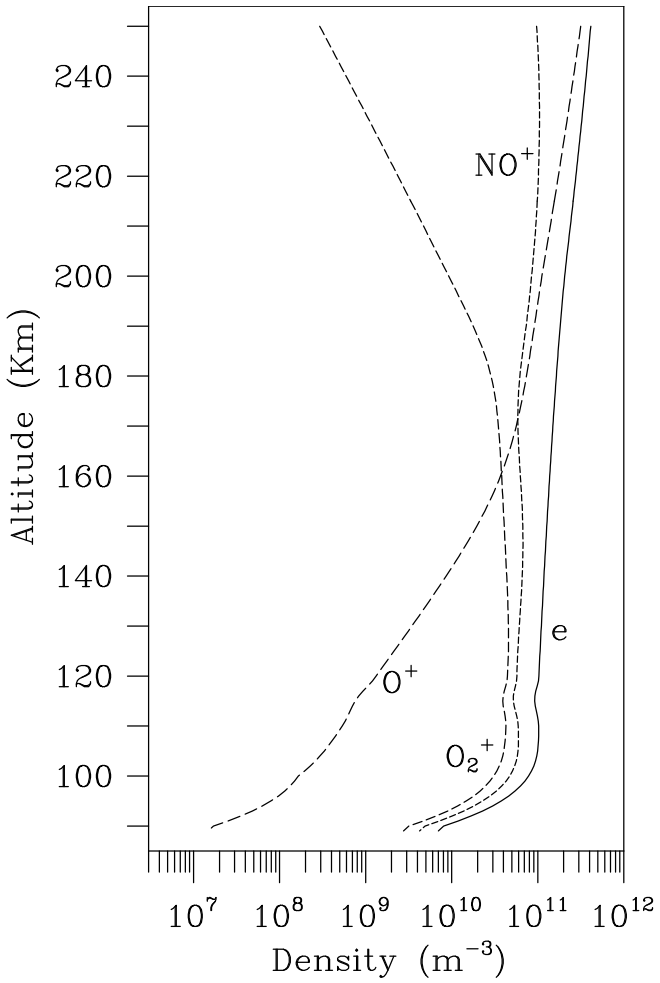

Figure 2.3: Dominant species of the E and bottomside F regions plasma composition. The profiles were derived from the IRI model.

2.4 Plasma dynamics versus altitude

The dynamics of the ionospheric plasma is also inhomogeneous with altitude. The dynamics at various altitudes are mainly determined by the simultaneous interaction of the neutral atmosphere and the geomagnetic field with the plasma. Altitudinal variations of plasma composition also plays a role in the inhomogeneity of the plasma dynamics.

2.4.1 The velocity equation

The dynamics of each plasma constituent is determined by internal forces of interaction among the various constituents as well as external forces acting on the volume occupied by the plasma. The plasma is assumed to be in force equilibrium since temporal and spatial variations of inertial motion of plasma components are ignorable compared to the characteristic parameters of the plasma medium such as the cyclotron, collision and plasma frequencies. The macroscopic motion of the plasma changes slowly compared to the microscopic characteristics of the plasma. The steady state assumption holds for analyzing the dynamics of the background plasma. For analysis of ionospheric waves, instabilities, and irregularities, where the main issue is growth and decay of perturbations in plasma parameters, the plasma might not be considered to be in a steady state condition.

Therefore, neglecting inertia, the law of acceleration for plasma species of type α, a component of the multi-fluid plasma, can be written as,

$$0 = n_\alpha q_\alpha(\mathbf{E} + \mathbf{V}_\alpha \times \mathbf{B}) - \kappa_B T_\alpha \nabla n_\alpha + n_\alpha m_\alpha[\mathbf{g} - \sum_{\beta \neq \alpha} \nu_\alpha \left(\mathbf{V}_\alpha - \mathbf{V}_\beta\right)] \qquad (2.1)$$

where, the plasma species α can be either an electron, $e = \mathrm{e}^-$, or an ion, $i = \mathrm{O}_2^+$, NO^+, O^+, etc. The quantities, n_α, m_α, and q_α, are plasma number density, mass, and charge of plasma species of type α, respectively. The first term is the Lorentz force acting on the plasma. The pressure gradient force, the second term, is derived from an ideal gas equation of state with an isothermal temperature (T_α) assumption, and κ_B is Boltzmann's constant. The gravitational field vector is denoted by $\mathbf{g}$. $\mathbf{V}_\alpha$ is the velocity of plasma species α, $\mathbf{V}_\beta$ is the velocity of ionospheric constituent of type β, $\mathbf{U}$ represents a neutral wind velocity vector, and ν_α is a collision frequency parameter.

In the lower ionosphere below the F region peak, plasma constituents are generally outnumbered by the higher concentration of neutral atmosphere gases. Collision frequencies between neutral gases and plasma particles are therefore dominant compared to Coulomb collisions. Our research is primarily focused on the dynamics in the equatorial E region where this assumption holds easily.

Assuming the above and using the definition $\mathbf{V}_{\alpha\mathbf{n}}$=$\mathbf{V}_\alpha - \mathbf{U}$, the velocity of plasma species α with respect to the neutral wind frame, (2.1) can be transformed to a neutral wind frame as,

$$0 = n_\alpha q_\alpha \mathbf{E_n} + n_\alpha q_\alpha \mathbf{V}_{\alpha\mathbf{n}} \times \mathbf{B} - \kappa_B T_\alpha \nabla n_\alpha + n_\alpha m_\alpha \mathbf{g} - n_\alpha m_\alpha \nu_\alpha \mathbf{V}_{\alpha\mathbf{n}} \tag{2.2}$$

where $\mathbf{E_n}$ is an the electric field in a frame reference moving with the neutral wind. The transformation, $\mathbf{E_n} \simeq \mathbf{E} + \mathbf{U} \times \mathbf{B}$, relates the Earth and the neutral wind frames. The neutral wind speed, $|\mathbf{U}|$, obviously belongs to a non-relativistic category. The electric fields, $\mathbf{E}$ and $\mathbf{U} \times \mathbf{B}$, are measured with respect to the Earth's frame. The electric fields in question are a background electric field caused by the solar driven global dynamo and a dynamo electric field caused by local thermospheric winds, respectively. Sources of ionospheric electric fields are discussed later in this chapter.

The perpendicular velocity component, $\mathbf{V}_{\alpha\mathbf{n}\perp}$, in the neutral wind frame of reference can be derived from (2.2),

$$\begin{aligned}
\mathbf{V}_{\alpha\mathbf{n}\perp} &= \frac{\Omega_\alpha \nu_\alpha}{|\mathbf{B}|(\Omega_\alpha^2 + \nu_\alpha^2)}(\mathbf{E}_\perp + \mathbf{U} \times \mathbf{B}) + \frac{\Omega_\alpha^2}{|\mathbf{B}|(\Omega_\alpha^2 + \nu_\alpha^2)}(\mathbf{E} + \mathbf{U} \times \mathbf{B}) \times \hat{\mathbf{b}} \\
&- \frac{\nu_\alpha^2}{\Omega_\alpha^2 + \nu_\alpha^2} d_\alpha \frac{\nabla_\perp n_\alpha}{n_\alpha} - \frac{\Omega_\alpha \nu_\alpha}{\Omega_\alpha^2 + \nu_\alpha^2} d_\alpha \frac{\nabla n_\alpha \times \hat{\mathbf{b}}}{n_\alpha} \\
&+ \frac{\nu_\alpha}{\Omega_\alpha^2 + \nu_\alpha^2} \mathbf{g}_\perp + \frac{\Omega_\alpha}{\Omega_\alpha^2 + \nu_\alpha^2} \mathbf{g} \times \hat{\mathbf{b}}
\end{aligned} \tag{2.3}$$

where $\Omega_\alpha = \frac{q_\alpha |\mathbf{B}|}{m_\alpha}$ is the cyclotron frequency containing the sign of the charge of the species α and $\hat{\mathbf{b}} = \frac{\mathbf{B}}{|\mathbf{B}|}$. The subscripts $\perp$ and $\parallel$ denote vector components perpendicular and parallel to $\mathbf{B}$, respectively, and $d_\alpha = \frac{\kappa_B T_\alpha}{m_\alpha \nu_\alpha}$ is a parallel diffusion coefficient, the diffusion coefficient plasma constituents would have been governed by, had they been unmagnetized.

In the presence of divergent currents, however, electric fields in equation (2.3) are modified to incorporate polarization electric fields arising from the plasma quasineutrality requirement. The net motion of the ionospheric plasma is then determined by the cumulative electric field which is a vector aggregate of the polarization and the background electric fields.

The component of the plasma velocity in longitudinal direction in the neutral wind frame, $V_{\alpha n\parallel}$, is obtained by taking the projection of the vector velocity, (2.2), along the geomagnetic field lines,

$$V_{\alpha n\parallel} = \left(\frac{q_\alpha}{m_\alpha \nu_\alpha}\right) |\mathbf{E}_\parallel| - d_\alpha \frac{|\nabla_\parallel n_\alpha|}{n_\alpha} + \frac{|\mathbf{g}_\parallel|}{\nu_\alpha} \tag{2.4}$$

2.4.2 Plasma dynamic characteristics

What do (2.3) and (2.4) indicate abut the dynamics of the plasma in the ionosphere? How does the vector velocity, $\mathbf{V}_{\alpha\mathbf{n}} = \mathbf{V}_{\alpha\mathbf{n}\perp} + \mathbf{V}_{\alpha\mathbf{n}\parallel}$, behave in the D, E, and F regions of the ionosphere?

Equation (2.3) indicates that plasma particles moves in a direction transverse to the geomagnetic field because of the action of a combination of the Lorentz, pressure gradient, and gravitational forces.

***D* region:**

In this region, $\nu_\alpha \gg \Omega_\alpha$, and plasma species undergo multiple collisions with the neutral atmosphere constituents before completing a gyration. Under such circumstances, equations (2.3) and (2.4) can be approximated by $\mathbf{V_{\alpha n}} \simeq \mathbf{0}$ or $\mathbf{V}_\alpha \simeq \mathbf{U}$. This implies that there is no relative motion between the neutral wind and the plasma. The plasma has a short memory of the presence of either an electric field or the geomagnetic field. The above arguments are also supported by the fact that conductivities in the D region are too meager to support significant currents.

***E* region:**

In this region, $\Omega_e \gg \nu_e$, and the motion of electrons is therefore controlled by the geomagnetic field. For electrons, in the perpendicular direction, equation (2.3) reduces to $\mathbf{V_{en\perp}} \simeq \frac{(\mathbf{E}+\mathbf{U}\times\mathbf{B})\times\hat{\mathbf{b}}}{|\mathbf{B}|}$, and $\mathbf{V_{e\perp}} \simeq \frac{\mathbf{E}\times\hat{\mathbf{b}}}{|\mathbf{B}|}$. The dominant motion of electrons is therefore a drift across both the geomagnetic and electric fields. However, for E region ions (dominantly O_2^+ and NO^+), $\nu_i > \Omega_i$, ion gyration rates are small compared to ion-neutral collisions, and the ions are marginally magnetized or unmagnetized. The use of this in equation (2.3) suggests that ions primarily move with the neutral wind. In addition, they move in the direction of the electric field. Ions do not $\mathbf{E} \times \mathbf{B}$ drift, since they are unmagnetized. Hence, unlike the case of D region, where the rarified plasma is strongly coupled to the neutral atmosphere, in the E region, ions and electrons carry out independent motion. The separation of ions and electrons resulting from the disparity in their motion gives rise to strong, anisotropic ionospheric current in the E region.

***F* region:**

In this region, $\Omega_\alpha \gg \nu_\alpha$, and both electrons and ions undergo much more frequent gyrations than collisions - they are magnetized. This is because the lighter atomic oxygen ions, O^+, have higher cyclotron frequencies, while the decay of the neutral atmosphere density causes a decrease in plasma-neutral collision frequencies. In this case, the second term in equation (2.3), the cross-field velocities, can be approximated by, $\mathbf{V_{e\perp}} \simeq \mathbf{V_{i\perp}} \simeq \frac{\mathbf{E}\times\hat{\mathbf{b}}}{|\mathbf{B}|}$. Electrons and ions gyrate in opposite senses, but their guiding center motions undergo charge independent drift in the same direction, preventing the generation of current. However, where ion-neutral collisions are not negligible in comparison to ion cyclotron frequencies, a current may be set up in the direction of the electric field, since electrons are completely magnetized.

In the parallel direction, plasma motion is not constrained by the Lorentz force. Consequently, (i) geomagnetic field lines are considered to be equipotential lines. Figure 2.4 shows that conductivities along the geomagnetic field are much larger than in transverse directions. Electrostatic potential differences between two points in space are invariant and can be communicated rapidly along magnetic field lines [*Farley*, 1959, 1960]. (ii) plasma density structures are likely to be anisotropic. The higher rate of parallel diffusion compared to perpendicular diffusion tends to annihilate plasma density structures in the direction of the magnetic field. Except below the bottomside *E* region where the equipotential approximation breaks down, and both parallel and perpendicular diffusion components behave the same way, parallel plasma motion with respect of the neutral wind given by (2.4) is negligible in much of the Earth's ionosphere. Parallel plasma velocity is largely caused by winds blowing in the parallel direction. However, parallel currents are

required in the ionosphere to neutralize perpendicular current divergence.

2.5 Ionospheric currents

The flow of electric currents in the upper atmosphere was confirmed by ground-based magnetic field fluctuation records as early as the 1880's. These currents flowing in the ionosphere are caused by differential drifts among the various constituents of the plasma. The differential drifts are due to a disparity in the responses by the various plasma components to interactions with force fields: electric and geomagnetic fields, the neutral atmosphere wind field, the gravitational field, plasma pressure gradients, etc. Ionospheric conductivities are direction dependent due to the presence of the geomagnetic field, and hence the ionospheric current is anisotropic.

The current density vector, $\mathbf{J}$, is defined as an algebraic sum of the current densities of each plasma species α,

$$\begin{aligned} \mathbf{J} &= \sum_{\alpha} n_\alpha q_\alpha \mathbf{V}_\alpha \\ &= \sum_{\alpha} n_\alpha q_\alpha (\mathbf{V}_\alpha - \mathbf{U}) \\ &= \sum_{\alpha} n_\alpha q_\alpha \mathbf{V}_{\alpha\mathbf{n}} \end{aligned} \tag{2.5}$$

In equation (2.5), we have employed the fact that relative velocities are frame independent for speeds $|\mathbf{U}|$ much less than the speed of light. This approximation is applicable for most of the solar-terrestrial environment.

Substituting equations (2.3) and (2.4) for each plasma species in the last line of equation (2.5), we obtain an expression for the anisotropic ionospheric current

density:

$$\begin{aligned}\mathbf{J} &= \sigma_P(\mathbf{E}_\perp + \mathbf{U}\times\mathbf{B}) + \sigma_H\hat{\mathbf{b}}\times(\mathbf{E}+\mathbf{U}\times\mathbf{B}) + \sigma_\circ\mathbf{E}_\parallel \\ &- \left(d_P\nabla_\perp n + d_H\nabla n\times\hat{\mathbf{b}} + d_\circ\nabla_\parallel n\right) \\ &+ e_P\mathbf{g}_\perp + e_H\mathbf{g}\times\hat{\mathbf{b}} + e_\circ\mathbf{g}_\parallel \end{aligned} \tag{2.6}$$

The coefficients, σ_P, σ_H, and $\sigma_\circ$ are the Pedersen, Hall and direct or parallel conductivities, respectively. They are defined in terms of a summation of the contribution from all plasma components.

$$\sigma_P = \sum_\alpha \left(\frac{n_\alpha q_\alpha}{B}\right)\frac{\nu_\alpha\Omega_\alpha}{\Omega_\alpha^2+\nu_\alpha^2} \tag{2.7}$$

$$\sigma_H = \sum_\alpha \left(-\frac{n_\alpha q_\alpha}{B}\right)\frac{\Omega_\alpha^2}{\Omega_\alpha^2+\nu_\alpha^2} \tag{2.8}$$

$$\sigma_\circ = \sum_\alpha \frac{n_\alpha q_\alpha^2}{m_\alpha\nu_\alpha} \tag{2.9}$$

The quantities d_P, d_H, and $d_\circ$, which are coefficients of pressure gradient driven currents, are defined in terms parallel diffusivity, d_α,

$$d_P = \sum_\alpha \frac{q_\alpha\nu_\alpha^2}{\Omega_\alpha^2+\nu_\alpha^2}d_\alpha \tag{2.10}$$

$$d_H = \sum_\alpha \frac{q_\alpha\nu_\alpha\Omega_\alpha}{\Omega_\alpha^2+\nu_\alpha^2}d_\alpha \tag{2.11}$$

$$d_\circ = \sum_\alpha q_\alpha d_\alpha \tag{2.12}$$

The quantities e_P, e_H, and $e_\circ$, which are coefficients of pressure gradient driven currents, are defined as,

$$e_P = \sum_\alpha \frac{n_\alpha q_\alpha\nu_\alpha}{\Omega_\alpha^2+\nu_\alpha^2} \tag{2.13}$$

$$e_H = \sum_{\alpha} \frac{n_\alpha q_\alpha \Omega_\alpha}{\Omega_\alpha^2 + \nu_\alpha^2} \tag{2.14}$$

$$e_\circ = \sum_{\alpha} \frac{n_\alpha q_\alpha}{\nu_\alpha} \tag{2.15}$$

The first, second, and third terms in (2.6), are known as the Pedersen, Hall, and parallel (or direct) currents, respectively. They are in the direction of the electric field, in the direction perpendicular to both the electric and magnetic fields, and in the direction parallel to the magnetic field, respectively. In the absence of an applied magnetic field, the expression of a longitudinal isotropic current in a regular conductor, $\mathbf{J} \simeq \left(\frac{ne^2}{m_e \nu_e}\right) \mathbf{E}$, is recovered. The anisotropic property of the ionospheric current is introduced by the geomagnetic field.

Plasma pressure gradients drive thermal and diamagnetic currents, as shown in (2.6). Thermal currents are driven by plasma gradients in the direction of gradients themselves. Diamagnetic current flows in a direction mutually perpendicular to the gradient and the magnetic field.

Plasma pressure gradient currents generally flow to annihilate particle pressure accumulation. Horizontal and vertical thermal currents, $-d_P \nabla_\perp n$, flow antiparallel to a positive plasma density gradient according to (2.6). In the equatorial electrojet setting, this current component flows vertically downwards below the E region peak, and upward above the peak and the valley region. Horizontally, it flows away from the local noontime meridian line toward the morning and evening sectors. Diamagnetic current component is represented by $-d_H \nabla n \times \hat{\mathbf{b}}$ in (2.6). The direction of the vertical diamagnetic current flow depends on its spatial location relative to the local noon time line. It flows vertically upward in the morning sector and downward in the after noon sector. Had the diamagnetic current been the sole source of ionospheric current, it would have caused vertical current shear

around the noon time meridian plane, and possibly a magnetic field aligned to the noon meridian plane. Thermal currents in the parallel direction is expected to be very small since density gradients in that direction are destroyed by the high rate of longitudinal diffusion. Analysis of the dynamics given above is based on the behavior of the background plasma density profiles in the equatorial E region.

Gravity driven current components, the last three terms in (2.6), are not negligible, although small compared to other current sources. Close to the magnetic equator where the dip angle is negligible, gravity drives two current components, namely, a vertically downward current in the direction of gravity vector, and a component mutually orthogonal to gravity and geomagnetic field lines. Outside the geomagnetic equator, gravity has a projection along geomagnetic field lines, and consequently, the gravitational field drives current in the parallel direction. The fact that the vertical component of gravity driven current flows vertically downward means, it is in opposition to any net vertically upward current outsourcing from the equatorial E to F region.

2.6 Ionospheric conductivities

Ionospheric daytime conductivity profiles calculated utilizing equations (2.7) through (2.9) are displayed in Figure 2.4. To calculate the profiles: collision frequencies were derived from a model by *Richmond* [1972] which in turn utilizes the MSIS-E-90 (Mass Spectrometer Incoherent scatter) model [*National Space Science Data Center*, 1990] to derive neutral densities and temperatures; geomagnetic field components derived from the IGRF (International Geomagnetic Reference Field) model [*National Space Science Data Center*, 2002] were used to calculate cyclotron frequencies. In the E region, electron density profiles were derived from the Chap-

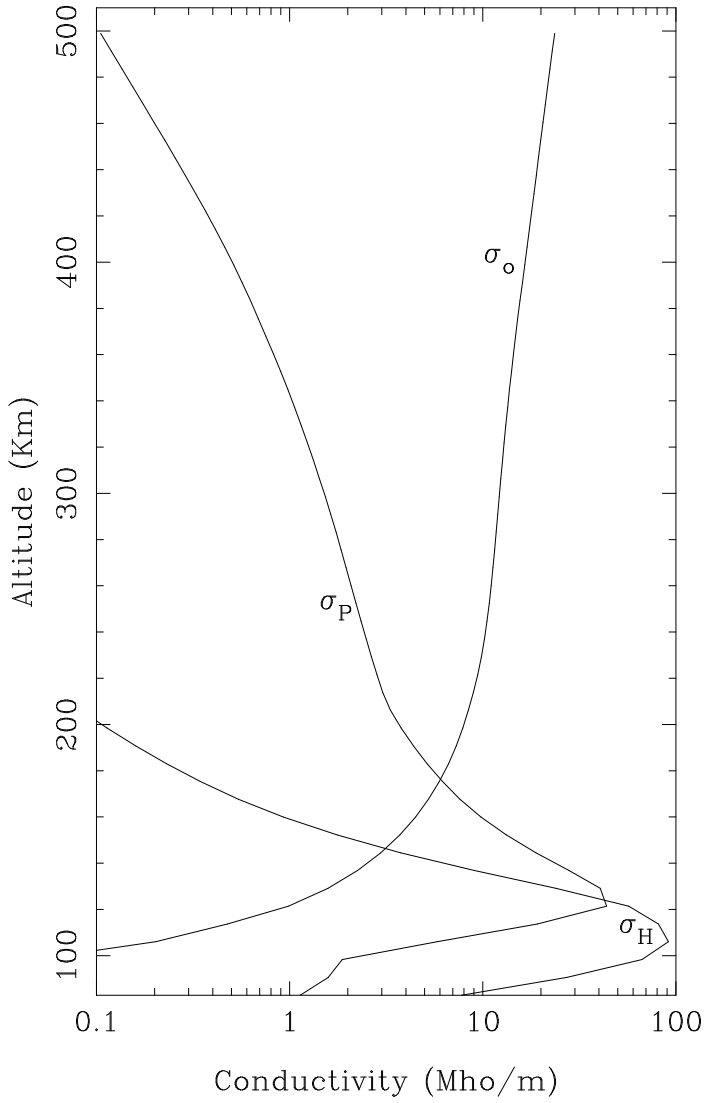

Figure 2.4: Typical daytime vertical profiles of Hall, Pedersen and parallel conductivities of the ionosphere. The Hall (σ_H) and Pedersen (σ_P) conductivities are multiplied by a factor of 10^4.

man function, and in the F region, electron density profiles and plasma composition were represented by the IRI model.

As shown in Figure 2.4, the Hall conductivity peaks around 105 km. Accord-

ingly, the Hall current is confined in a narrow altitude range in the E region. The Pedersen conductivity, on the other hand, extends from the lower E region and falls gently to F region heights. This might be because the coupling between the neutral atmosphere and ions decays slowly in the direction of the electric field compared to the cross-field direction (or the Hall direction). Pedersen current therefore flows in the F region. The direct (or parallel) conductivity increases with altitude since collision frequencies fall with altitude such that the motion of plasma particles is not impeded.

The ratio of longitudinal to Pedersen conductivities in the F region can be approximately written as,

$$\frac{\sigma_P}{\sigma_\circ} \simeq \frac{\nu_e \nu_i}{\Omega_e \Omega_i} \tag{2.16}$$

The magnitude of the ratio $\frac{\nu_e \nu_i}{\Omega_e \Omega_i}$ decreases with altitude. We will see later in this chapter that the ratio is defined by $\Psi_\circ$, which is related to the anisotropy factor, Ψ, defined by equation (2.46). At F region heights, therefore, Pedersen conductivities compete with longitudinal conductivities if the latter is scaled by $\Psi_\circ$.

The conductivity profiles are such that both Hall and Pedersen currents are supported in the E region. The equatorial and polar E regions in particular exhibit strong currents that can be utilized as a source of energy to excite plasma instabilities. In the F region, Pedersen currents flow but Hall currents are suppressed.

An integral component in the definition of conductivities is the plasma number density, which can be described in a quasineutral plasma as $n \simeq n_e \simeq \sum_\beta n_\beta$, the β summation running over all ion species. Efforts to model conductivity profiles with the ultimate objective of an accurate modeling of electric fields and hence

plasma dynamics of the ionosphere depend on the accurate estimation of plasma density profiles and other parameters. Plasma density profiles are regularly measured using incoherent scatter radar (ISR) measurements. The presence of plasma irregularities (equatorial/auroral electrojet and spread F, for instance) in the ionosphere is, however, an impediment for the ISR technique. Plasma density profiles consequently are poorly known in regions where irregularities occur persistently. Electron density profile measurements in the equatorial electrojet are among the issues addressed in this dissertation. The dissertation presents a technique for inferring electron density profiles in the equatorial E region utilizing plasma density irregularities themselves for radar scattering.

2.7 Plasma dynamics versus latitude

Global solar heating and tidal winds are major sources of polarization electric fields in the low and mid latitude ionospheres. Winds cause relative motion between ionospheric charged particles, and polarization electric fields are produced to oppose net charge accumulation, making the ionosphere a generator. Since the high latitude ionosphere is connected to the magnetosphere and interplanetary space by means of magnetic field lines, it has direct access to convection electric fields generated in the magnetosphere and the solar wind, and the ionosphere therefore also acts as a load. Winds can be a source of electric fields at high latitudes. However, dynamo fields are generally much smaller than convection electric fields.

The geometry of the geomagnetic field also influences the way plasma behaves at various latitudes. Near the magnetic equator, the magnetic dip angle is very small such that magnetic field lines are nearly horizontal. The horizontal geometry of the geomagnetic field has the effect of amplifying the vertical polarization electric

field that drives the equatorial electrojet. An eastward electric field generated by the global dynamo causes a vertically downward Hall current in the E region. However, the Hall current is restricted to a narrow strip of altitudes due to the behavior of the Hall conductivity (Figure 2.4), and the current therefore polarizes the strip. A vertical polarization field is set up to negate the charge accumulation made possible by the horizontal geometry of the geomagnetic field.

At mid-latitudes, the dominant plasma irregularity phenomena are so-called quasiperiodic radar echoes. These echoes, coming from altitudes between 90 and 120 km, are believed to be associated with sporadic E layers. Neutral wind shear and the associated Kelvin-Helmholz instabilities are proposed to be responsible for vertical transport of ionization. Given this physical scenario, gradient drift instabilities may generate the plasma irregularities that give rise to the observed quasiperiodic radar echoes [*Larsen*, 2000].

At high latitudes, magnetic field lines are almost perpendicular to the surface of the Earth. Given a perpendicular magnetic field geometry, an eastward convection electric field mapped from the magnetosphere, drives an equatorward Hall current in an auroral arc. An auroral arc is associated with an area of enhanced particle precipitation and conductivity. Outside the arc, the conductivities are determined by background plasma processes and are small compared to those inside the arc. A Hall current driven by the east-west electric field is greater inside the arc than outside. This scenario gives rise to charge build up on the edge of the arc at the north-south boundaries. A polarization electric field is established, in the north-south plane, to oppose charge accumulation. The polarization electric field is among the components that drives the strong east-west current known as the auroral electrojet.

2.8 Electric fields

Polarization electric fields are generated so as to preserve divergence free current in the ionosphere. Electric fields generated by the wind dynamo mechanisms drive current and set the ionospheric plasma into vertical and horizontal motion.

2.8.1 The terminator electric field

On the dayside of the Earth, neutral gases in the upper atmosphere are heated by the Sun. In response to pressure gradient generated by solar heating, atmospheric gases expand towards low pressure regions. Neutral gases expanding vertically upward drive a zonal Pedersen current, $\sigma_P(\mathbf{U} \times \mathbf{B})$, flowing toward dawn as shown by a broken arrowed curve in Figure 2.5. This mechanism of generating a Pedersen current is applicable for both the E and F regions.

The Pedersen current flowing toward the morning sector is mainly carried by ions. Electrons are left behind the ions since they are magnetized. The Pedersen current is therefore prone to accumulate positive charge at the dawn terminator, and negative charge at the dusk terminator as shown schematically in Figure 2.5. This is because the conductivities fall sharply beyond the morning and evening solar terminators. Divergence free current requirement in a plasma opposes net charge accumulation at the terminators by setting up a zonal polarization electric field, $\mathbf{E}_\circ$, shown in Figure 2.5. The polarization field is directed from the dawn terminator to the dusk terminator; its direction is eastward during the day and westward at night.

The diurnal zonal polarization electric field produced by the current termination mechanisms which exists in both the E and F regions is called the terminator

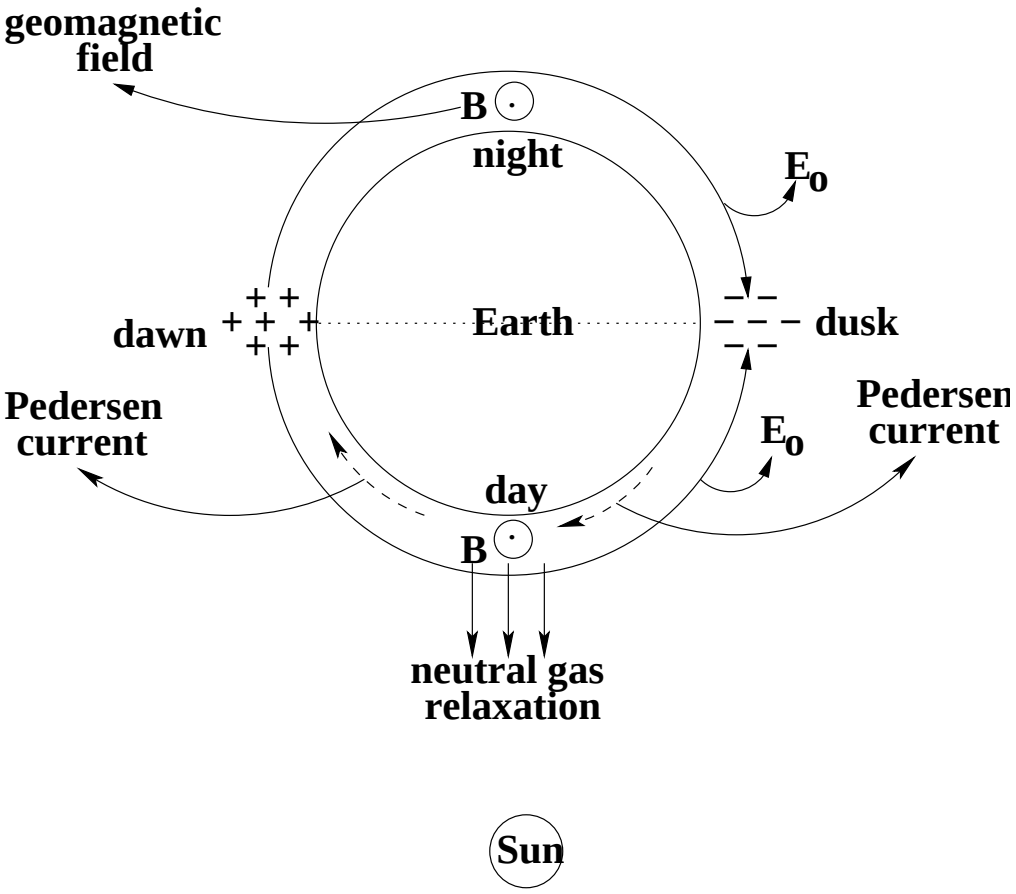

Figure 2.5: Schematic representation of the terminator electric field. The geomagnetic lines of force shown by $\odot$ are directed out of the page. The figure shows a cross section of the equatorial plane looking down the North pole from space. Reproduced from *Kelley* [1989].

electric field. The terminator electric field has a seasonal as well as a solar cycle variability, having a larger magnitude during equinoxes and solar maximum conditions [*Fejer*, 1991]. The zonal electric field of the equatorial ionosphere is enhanced in magnitude around sunset before a westward polarity reversal, giving rise to so called prereversal enhancement phenomena. The zonal electric field is among the

crucial elements for driving the equatorial electrojet. The large scale plasma uplift (descent) during the day (night) in the equatorial ionosphere, happening during quiet geophysical conditions, is caused by the terminator electric field.

However, local tidal winds could affect the diurnal pattern of drifts by reversing the polarity and changing the magnitude of vertical drifts (zonal electric fields). In addition, storm-time disturbance dynamo fields can influence the magnitude and direction of vertical drifts [*Blanc and Richmond*, 1980; *Scherliess and Fejer*, 1997; *Fuller-Rowell et al*, 2002].

The diurnal behavior of the quiet-time terminator electric field at F region heights has been observed using incoherent scatter radar techniques at JRO [*Fejer*, 1991].

2.8.2 Vertical polarization electric fields

During quiet-times, zonal drifts are westward (upward electric field) during the day, and eastward (downward electric field) at night. What are the physical mechanisms for generating the observed diurnal vertical electric field structure? Analysis of the origin of vertical electric fields in the equatorial F region presented in the following paragraphs is based on *Rishbeth* [1971], *Kelley* [1989], *Rishbeth* [1997], and *Heelis* [2004].

The projection of the current density vector, equation (2.6), in the direction of $\hat{\mathbf{z}}$, a unit vector in the vertical direction, in the equatorial F region can be written as,

$$\hat{\mathbf{z}} \cdot \mathbf{J} = \hat{\mathbf{z}} \cdot \sigma_P (\mathbf{U} \times \mathbf{B}) = \sigma_P u B \tag{2.17}$$

where $u = \mathbf{U} \cdot \hat{\mathbf{x}}$, the projection of the wind vector in the zonal direction.

Equation (2.17) represents an upward Pedersen current flowing in the F region driven by an eastward wind field. Due to the finite thickness of the Pedersen conductivity layer, the vertical current given by (2.17) is divergent.

The vertical polarization field, E_p, developed to keep the current non-divergent is given by *Kelley* [1989]; *Heelis* [2004]. The physics of dynamo field generation in the F region is contained in this equation,

$$E_p = -\frac{uB\Sigma_P^F}{\Sigma_P^F + \Sigma_P^E} \tag{2.18}$$

where Σ_P^E and Σ_P^F are magnetic field line integrated E and F region Pedersen conductivities, respectively.

During the day, parallel currents flow along the highly conducting magnetic field lines and through the off-equatorial E region to offset current divergence. The current keeps flowing, and polarization electric fields generated by the F region dynamo are short-circuited by the conducting E region, since the E to F region Pedersen conductivity ratio is much larger than one during the day. The main source of E_p in the F region is the E region tidal wind dynamo situated off the equatorial region. The E region is a generator, $\mathbf{J} \cdot \mathbf{E} < \mathbf{0}$, and the F region is a load, $\mathbf{J} \cdot \mathbf{E} > \mathbf{0}$, during the day. (The situation is reversed at night). In response to the polarization field, F region ions and electrons drift westward with a speed $V_e = V_i = \frac{E_p}{B}$ during the day.

During the evening, conductivities in the E region decay rapidly compared to the F region due to the high rate of molecular recombination. In this case, the dynamo electric field created by the F region dynamo remains intact, owing to a significant reduction in the short-circuiting effect of the E region. The F region dynamo produces polarization electric fields to counter charge accumulation. The motion of plasma in the F region is such that its drift nearly matches wind velocity,

$V_e = V_i = \frac{E_p}{B} \simeq u$. This results in a reduction of ion drag on the wind, leading to an increased eastward wind velocity at night and the possible cause of the so-called superrotation phenomena in the upper atmosphere.

In the equatorial E region, the eastward background electric field, generated by the dawn-dusk polarization mechanism discussed above drives a vertically downward Hall current. The Hall current is divergent because of the finite thickness of the Hall conductivity layer. This arrangement demands an upward polarization electric field to neutralize net charge accumulation at the boundaries. The field is directed upward during the day and downward at night. A vertical Pedersen current driven by an eastward (westward) wind reduces (amplifies) the vertical electric field produced by the terminator electric field.

2.8.3 On the role of zonal winds

A projection of the total vector current density, $\mathbf{J}$, given by (2.6), in the zonal direction, $\hat{\mathbf{x}}$,

$$\hat{\mathbf{x}} \cdot \mathbf{J} = \hat{\mathbf{x}} \cdot \Big(\sigma_P (\mathbf{E} + \mathbf{U} \times \mathbf{B}) + \sigma_H \hat{\mathbf{b}} \times (\mathbf{E} + \mathbf{U} \times \mathbf{B}) \Big) \tag{2.19}$$

In equation (2.19), the vector electric field, $\mathbf{E}$, consists of a background and perturbation parts. The background component of the electric field vector could be estimated from either 150 km echo vertical Doppler shifts or ISR vertical drifts at the Jicamarca Radio Observatory (JRO) in Perú [*Chau and Woodman*, 2004]. However, realistic modeling of the perturbation component of electric fields, which are related to both the global and local wind dynamos, is challenging, since it requires knowledge of realistic behavior of local wind profiles themselves in the electrojet region.

Zonal wind measurements from rocket chemical release experiments are generally characterized by large amplitude and short wavelength oscillations with dominant eastward directed winds at the center of the electrojet [*Larsen and Odom*, 1997; *Larsen*, 2002]. The WINDII instrument onboard UARS satellite has similar phase characteristics as the rocket data, but the amplitudes of the satellite data are generally small. In this dissertation, we use radar Doppler measurements of electrojet irregularities to infer zonal wind profiles in the electrojet. Doppler measurements of electrojet irregularities are routinely carried out at the JRO. Analysis of temporal characteristics of zonal winds and dynamo behaviors are made possible by the availability of the radar Doppler data. Zonal winds modulate electric field structures and Doppler shift characteristics of the irregularities. The contribution of local dynamo in generating the electrojet current and instabilities might, however, be small in comparison to the background zonal electric field.

2.9 The equatorial electrojet

The equatorial electrojet (and current flow in the ionosphere in general) is evident in the regular daily oscillations seen in geomagnetic field records. A physical explanation for the fluctuation of geomagnetic fields from their background values was put forward by Belfour Stewart in the 1880's [*Forbes*, 1981; *Rishbeth*, 1997] as follows: the periodical geomagnetic field perturbation is due to motion of conducting air in the Earth's upper atmosphere caused by the action of neutral atmosphere dynamo. Since then, the flow of current in the upper atmosphere has been attributed to wind dynamo processes.

However, quantitative investigations and analysis of the physical mechanisms of the electrojet current did not come forward before the 1960's. A number of studies

including *Rishbeth* [1971], *Richmond* [1973a, b], *Fambitakoye et al* [1976], *Forbes and Lindzen* [1976a, b], *Reddy and Devasia* [1981], *Reddy et al* [1987], *Richmond* [1995], and *Hysell et al* [2002] have pursued the problem by modeling the low latitude E region electric field and current structures and have contributed immensely to our knowledge of the equatorial electrojet and the low latitude ionosphere.

2.9.1 Definitions

The dominant motions of plasma particles in the E region are characterized by coupling of ions with the neutral atmosphere through collisional interactions, $\mathbf{E} \times \mathbf{B}$ drifting electrons, and the contribution of the neutral atmosphere to a differential drift between electrons and ions, constituting a current. The resulting current is not generally divergence free and causes net charge accumulation in the plasma. Since the scale lengths of interest here are much bigger than the Debye length, which can be approximately of the order of a centimeter, the ionosphere maintains plasma quasineutrality by establishing polarization electric fields. The dynamo electric fields, generated by the neutral wind field actions, in combination with the Hall and Pedersen conductivities, drive currents in the E region ionosphere.

The equatorial electrojet is driven by a combination of the horizontal geometry of the geomagnetic field at the magnetic equator, anisotropy in ionospheric conductivities, the confinement of the Hall conductivity in a narrow slab, global solar-driven dynamo action, and the resulting horizontal and vertical polarization electric fields [*Richmond*, 1973a, b; *Forbes*, 1981].

The equatorial electrojet is the second largest current system, second in strength to auroral electrojet, in the terrestrial ionosphere. The net equatorial electrojet can have a magnitude as large as 100 kA or, equivalently, can cause about a 100

nT deflection in the horizontal component of the geomagnetic field measured by magnetometer on the ground at local noon.

The regular course of the electrojet is eastward during the day. At night, the direction of the current is reversed to westward, and its magnitude is severely reduced due to reduction of conductivity after sunset. The electrojet current reverses from its normal course during the so called counterelectrojet condition [*Hanuise et al*, 1979].

The equatorial electrojet is confined to a narrow slab of latitudes, extending from about -2° magnetic South to +2° magnetic North. Vertically, the current is confined to a narrow band from about 95 to 115 kilometers of altitude and peaks at about 108 kilometer, coinciding, approximately with the altitude of the Hall conductivity peak (Figure 2.4). Beyond ±2° magnetic latitudes, the magnetic dip angle is no longer negligible, and gravitational and pressure gradient forces have finite components in the direction of the magnetic field and force plasma particles to slide along field lines to higher equatorial latitudes. Therefore, for finite dip angles, the formation of the polarizing conductivity boundaries, which is an integral component in the setup of the electrojet current, might be missing.

2.9.2 Mechanism of the electrojet current

A zonally eastward primary electric field (caused by a global solar heating dynamo) drives a Pedersen current in the direction of the electric field along with a downward Hall current (dynamo fields driven by local winds are not considered here for the sake of simplicity). A secondary polarization electric field generated by the mechanism discussed earlier in this chapter drives a zonal Hall current in the direction of the original electric field. It also drives an upward Pedersen current in

the direction of the secondary field to cancel the downward Hall current. The aggregate of the zonal Pedersen and Hall currents lead to an amplified current called the equatorial electrojet. The amplification is done by so-called Cowling conductivity factor. The equatorial electrojet makes the E region ionosphere unstable and produces multi-spatial scale field-aligned plasma irregularities. The horizontal geometry of the geomagnetic field near the magnetic equator contribute to the amplification of the polarization electric field and the current.

2.9.3 A simple model of the equatorial electrojet current

A simplified expression for the equatorial electrojet current, J_x, derived from the current density (2.6), is given below,

$$J_x = \sigma_c E_x + d_{c1}\frac{\partial n}{\partial z} - d_{c2}\frac{\partial n}{\partial x} + e_c g \tag{2.20}$$

In deriving (2.20), we have assumed that vertical ionospheric currents are suppressed, the upward Pedersen current driven by the secondary field completely cancels the downward Hall current driven by the primary field, and neutral winds are suppressed for the moment. The zonal electric field, E_x, could have background and polarization components. Plasma density gradients in the zonal and vertical directions are given by $\frac{\partial n}{\partial x}$ and $\frac{\partial n}{\partial z}$, respectively.

The coefficients in (2.20) are defined as,

$$\sigma_c = \sigma_P \left(1 + \frac{\sigma_H^2}{\sigma_P^2}\right) \tag{2.21}$$

$$d_{c1} = d_H \left(1 + \frac{d_P}{d_H}\frac{\sigma_H}{\sigma_P}\right) \tag{2.22}$$

$$d_{c2} = d_P \left(1 - \frac{d_H}{d_P}\frac{\sigma_H}{\sigma_P}\right) \tag{2.23}$$

$$e_c = (e_H + e_P) \tag{2.24}$$

The major contribution to the electrojet current comes from the first term in (2.20). The ordinary zonal Pedersen current, $\sigma_P E_x$, is amplified to become $\sigma_c E_x$, σ_c being so called Cowling conductivity. The factor $\frac{\sigma_c}{\sigma_P} = 1 + \frac{\sigma_H^2}{\sigma_P^2} \simeq 1 + \frac{\nu_i^2}{\Omega_i^2}$, where the ratio $\frac{\nu_i}{\Omega_i}$ can be about 10 - 30 in the E region. The zonal Pedersen current is therefore amplified by about a factor of 100 - hence the strength of the equatorial electrojet. Since the second term in (2.20), $\frac{d_P}{d_H} \simeq \frac{\Omega_e}{\nu_e}$ in the E region, the contribution of density gradient driven current could be important depending on the scale size in question. On the other hand, $\left(\frac{d_H}{d_P}\right)\left(\frac{\sigma_H}{\sigma_P}\right) \simeq \frac{\nu_e \nu_i}{\Omega_e \Omega_i} = \Psi_\circ < 1$ at the center of the electrojet, the third term could decrease the strength of the electrojet, though by a small amount. The last term in (2.20) represents zonal part of gravity driven current.

2.10 Coherent scatter radar observation of electrojet irregularities

Radar and *in situ* probing techniques have been of great help for extracting plasma parameters in the terrestrial ionosphere. Radar observations for ionospheric studies have been in place since the 1930s and, as a result, our knowledge regarding plasma dynamics, plasma irregularities, plasma compositions etc. has expanded.

Radar ionospheric probing relies on scattering of an incident radio wave by either thermal fluctuations or nonthermal density irregularities in the ionospheric plasma. Radar scattering occurs according to Bragg's condition for constructive interference. In case of monostatic radar, which is the most typical scenario, backscattered signals from thermal or nonthermal fluctuations spaced by half the

wavelength of the incident electromagnetic wave interfere with each other constructively.

The scattered signal at the receiver contains a wealth of information in terms of drifts, densities, temperatures etc., which can be used to characterize the properties of the plasma. Depending on the nature of the scattering medium, two types of radar techniques, namely, coherent and incoherent scatter, can be employed for probing the ionosphere. A brief description of the two scattering techniques is presented below.

2.10.1 Incoherent scatter radar probing

A radar that detects thermal fluctuations of the medium utilizes the incoherent scatter technique. The physical basis of the incoherent scatter radar technique is a modified version of Thomson scattering, the re-radiation of incident radio waves by ionospheric free electrons. Since electrons are correlated to other electrons and ions via electrostatic waves (Langmuir and ion-acoustic waves), incoherent scattering is not actually incoherent. The electron scattering cross-section is so small, in the region of $10^{-28}\mathrm{m}^2$, that an incoherent scatter radar system must be very sensitive to detect the weak incoherent scatter signal. The technique, therefore, requires a high power transmitter, a large antenna, sensitive receivers etc. The incoherent scatter spectrum comprises three spectral lines, namely, the ion, plasma and gyro lines. The ion line is used to infer plasma density, electron and ion temperatures, plasma drifts, composition, etc. The offset of the plasma line is proportional to the electron plasma frequency and hence might be used to estimate the plasma density of the medium. The gyro line appears at an offset frequency proportional to the electron cyclotron frequency and might therefore be helpful in estimating the geomagnetic

field. In practice, plasma parameters are estimated by comparing autocorrelation functions of the received signal with a theoretical plasma autocorrelation function (a Fourier transform of the incoherent scatter spectrum) in a least-square sense.

2.10.2 Coherent scatter radar probing

In the ionosphere, coherent scatter comes from field-aligned irregularities: the equatorial and auroral electrojet, sporadic E layers, and equatorial spread F among their sources. The Doppler shifts of irregularities are commonly estimated from coherent scatter spectra at Jicamarca and elsewhere. The measured Doppler shifts are associated with the phase speeds of the waves producing the scatter. Coherent scatter radars can sometimes also be used to estimate ionospheric electron density profiles and other background parameters. In Chapter 4, we show electron density profiles in the equatorial E region estimated from the Faraday rotation of coherent scatter from the electrojet.

2.10.3 Type I and type II coherent scatter radar echoes

Coherent scatter radar echoes from short wavelength field aligned plasma irregularities in the equatorial electrojet are of two kinds, namely, type I and II. Figure 2.6 and Figure 2.7 are examples of type I and II radar spectra, respectively. The spectra were observed utilizing a narrow beam 50MHz (corresponding to 3 meter density irregularities) oblique coherent scatter radar experiment conducted at the JRO on September 22, 2003 and March 22, 2003, respectively. The Doppler spectra shown in the figures represent coherent scatter radar echoes from various range gates in the scattering volume.

The salient features of type I and type II radar echoes were summarized in

reviews by *Fejer and Kelley* [1980] and *Farley* [1985]. We have listed some of the major ones below. These charactersitics are applicable to equatorial electrojet irregularities:

1. Both type I and II radar echoes come from highly field aligned irregularities. The irregularities causing the scattering are confined in a two-dimensional plane perpendicular to the geomagnetic field. Coherent scatter radar returns from the electrojet are insignificant for radar pointing directions, more than about 1° off the perpendicular direction.

2. The Doppler velocities of type I echoes do not seem to follow equation (2.44). They rather appear to follow the marginal growth condition of the Farley-Buneman instability, the first term in equation (2.45). On the other hand, it appears that, the Doppler velocity of type II echoes is described by the linear dispersion relation (2.44).

3. Type II echoes are observed by coherent scatter radar whenever the density gradient has a positive projection along the electric field. This condition is not important for observing type I echoes.

4. Type I echoes are characterized by a narrow Doppler spectrum, whereas the width of a type II spectrum is generally much wider and might be proportional to Doppler frequency of the type II echoes.

5. During counter electrojet conditions (when the electrojet is reversed from its normal direction), type II echoes are not observed due to absence of a positive component of density gradient along the electric field. The type I echoes seem to be unaffected by the counter electrojet effect, however.

6. According to the linear theory, the Farley-Buneman instability mechanism can account for the excitation of type I echoes at 3 meter wavelengths. Type II

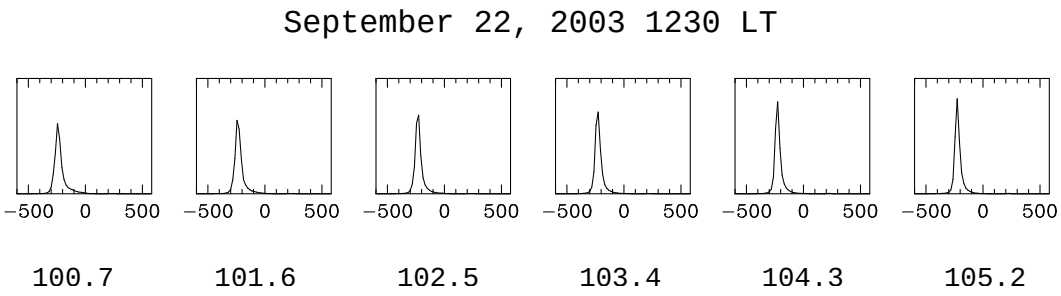

Figure 2.6: Type I radar spectra measured by the oblique coherent scatter radar system at JRO. Normalized power is plotted versus Doppler velocity in meters per second. Altitudes in kilometers corresponding to each spectrum are shown below the boxes. Power is normalized by aggregate of power in each Doppler bin.

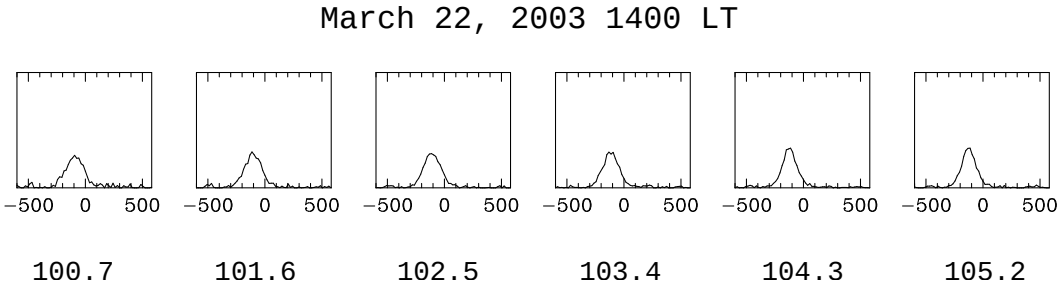

Figure 2.7: Type II radar spectra measured by the oblique coherent scatter radar system at JRO. Normalized power is plotted versus Doppler velocity in meters per second. Altitudes in kilometers corresponding to each spectrum are shown below the boxes. Power is normalized by aggregate of power in each Doppler bin.

echoes are linearly stable at meter scales, however. Short wavelength irregularities causing type II radar echoes are thought to be driven by a nonlinear mode coupling processes involving intermediate wavelength gradient drift irregularities. Small scale Farley-Buneman irregularities are also generated by nonlinear mode coupling

processes.

Type I and II radar echoes discussed above are taken mainly to be caused by primary Farley-Buneman and secondary gradient-drift processes. Further discussion of the generation mechanism of the irregularities causing the radar scattering will be presented in the next section.

2.11 Equatorial electrojet plasma irregularities

We have mentioned earlier in this chapter that, in the E region, ions are collisional, and electrons are magnetized. This scenario, combined with the zero magnetic dip angle at the magnetic equator, produces the equatorial electrojet current. The free gravitational potential energy stored in the F region excites equatorial spread F by the Rayleigh-Taylor mechanism. Likewise, the free electrostatic potential energy stored in the equatorial electrojet is released by exciting gradient-drift and Farley-Buneman instabilities owing to unequal drift between electrons and ions. The electrojet excites a broadband spectrum of field aligned plasma irregularities generated by the Farley-Buneman and gradient-drift instability mechanisms. The plasma irregularities have wavefronts aligned with the geomagnetic field. The Farley-Buneman and gradient-drift instabilities are aspect sensitive since their growth is highly confined to a plane perpendicular (within $\pm 1^{\circ}$) to the geomagnetic field.

With multi-spatial scales, ranging from meters to kilometers, electrojet plasma irregularities have been detected by coherent scatter radars (at JRO and else where), and in rocket experiments. Radar returns from the electrojet have been gathered from elevation angles in the plane perpendicular to the geomagnetic field. Linear and nonlinear electrojet instability theories have been formulated [*Farley*

and Balsley, 1973; *Sudan et al*, 1973; *Fejer et al*, 1975; *Sudan*, 1983a, b; *Farley et al*, 1981; *Kudeki et al*, 1982; *Farley*, 1985; *Kudeki et al*, 1987] for the purpose of analyzing and interpreting characteristics of the Doppler spectra (Doppler shifts and widths). Linear instability theory explains a great deal but not all of the characteristics of the radar echoes.

2.11.1 The linear local theory of electrojet irregularities

We use a linear local analysis and a fluid formalism to derive the dispersion relation of electrojet instabilities. In practice, variations in background parameters with altitude creates inhomogeneity in the electrojet and demands nonlocal analysis. The irregularities interact with the inhomogeneous medium and the oscillation frequency of the waves varies with altitude, for example. In many instances, however, the difference in irregularity characteristics revealed by local and nonlocal theories is not significant. Stated in more specific terms, for very fast growing small scale modes, the inhomogeneity does no have time to affect irregularities before they are saturated [*Drexler*, 2004].

The following assumptions are employed in the derivation of the linear dispersion relation of electrojet plasma irregularities: (i) electrons are considered to be massless and electron inertia is neglected, (ii) the plasma quasi-neutrality is assumed since the wavelengths of interest are much larger than the Debye length, (iii) electric fields are electrostatic, (iv) electrons are magnetized and ions are unmagnetized, and (v) fluid equations, namely, the momentum and continuity equations for a two component plasma will be employed.

The momentum equation for species α can be written as,

$$n_\alpha m_\alpha \frac{d\mathbf{V}_\alpha}{dt} = n_\alpha q_\alpha(\mathbf{E} + \mathbf{V}_\alpha \times \mathbf{B}) - \nabla P_\alpha - n_\alpha m_\alpha \nu_{\alpha\beta} (\mathbf{V}_\alpha - \mathbf{U}) \tag{2.25}$$

Here, we ignore the influence of gravity compared to other terms. The fluid pressure for species α is denoted by P_α.

The continuity equation for species α is

$$\frac{\partial n_\alpha}{\partial t} + \nabla \cdot (n_\alpha \mathbf{V}_\alpha) = Q_\alpha - L_\alpha = Q_\alpha - \beta n_\alpha^2 \tag{2.26}$$

where Q_α and $L_\alpha = \beta n_\alpha^2$ are the production and loss rates, respectively. The loss rate is assumed to be proportional to the square of n_α in the E region where the neutral atmosphere is relatively denser. The proportionality constant is a recombination coefficient β.

We have employed the standard linearization technique. Ionospheric parameters characterizing the plasma are expressed in terms of a combination of the equilibrium value and a linear perturbation term, which is assumed to be small compared to equilibrium value,

$$\begin{aligned} n_\alpha &= n_{\alpha\circ} + \lambda n_{\alpha 1} \\ T_\alpha &= T_{\alpha\circ} + \lambda T_{\alpha 1} \\ \mathbf{V}_\alpha &= \mathbf{V}_{\mathbf{D}\alpha} + \lambda \mathbf{v}_{\alpha\mathbf{1}} \\ \mathbf{E} &= \mathbf{E}_\circ - \lambda \nabla \mathbf{\Phi} \\ P_\alpha &= P_{\alpha\circ} + \lambda p_{\alpha 1} \end{aligned} \tag{2.27}$$

The quantity λ is an expansion parameter. The zero order drift velocity is given by $\mathbf{V}_{\mathbf{D}\alpha}$. The parameters $n_{\alpha\circ}$, $\mathbf{E}_\circ$, and $P_{\alpha\circ}$ are equilibrium values whereas $n_{\alpha 1}$, $T_{\alpha 1}$, $\mathbf{v}_{\alpha\mathbf{1}}$, and $p_{\alpha 1}$ are perturbed quantities. The perturbed electric field is written in terms of the gradient of an electrostatic potential Φ.

In adiabatic processes obeying the ideal gas equation of state, the plasma pressure and plasma density are related by,

$$P_\alpha = C n_\alpha^{\gamma_\alpha} \tag{2.28}$$

where C is a constant of proportionality and γ_α is the ratio of specific heat capacities.

Combining (2.28) with the linearized pressure (2.27), the pressure gradient becomes,

$$\nabla P_\alpha = \gamma_\alpha \kappa_B T_{\alpha\circ} \nabla n_{\alpha\circ} + \lambda[\gamma_\alpha \kappa_B (T_{\alpha 1} \nabla n_{\alpha\circ} + T_{\alpha\circ} \nabla n_{\alpha 1})] \tag{2.29}$$

where $P_{\alpha\circ}$ and $p_{\alpha 1}$ are given by the first term in (2.29), and sum of the second and third terms in (2.29), respectively.

Substituting the above linearized quantities, (2.27), into the force and continuity equations, (2.25) and (2.26), we obtain,

$$\begin{aligned}(n_{\alpha\circ} + \lambda n_{\alpha 1}) m_\alpha \frac{d(\mathbf{V}_{D\alpha} + \lambda \mathbf{v}_{\alpha\mathbf{1}})}{dt} &= n_\alpha q_\alpha (\mathbf{E}_\circ - \lambda \nabla \mathbf{\Phi} + (\mathbf{V}_{\mathbf{D}\alpha} + \lambda \mathbf{v}_{\alpha\mathbf{1}}) \times \mathbf{B}) \\ &- \nabla (P_{\alpha\circ} + \lambda p_{\alpha 1}) \\ &- (n_{\alpha\circ} + \lambda n_{\alpha 1}) m_\alpha \nu_{\alpha\beta} \left((\mathbf{V}_{\mathbf{D}\alpha} + \lambda \mathbf{v}_{\alpha\mathbf{1}}) - \mathbf{U} \right)\end{aligned} \tag{2.30}$$

$$\frac{\partial (n_{\alpha\circ} + \lambda n_{\alpha 1})}{\partial t} + \nabla \cdot ((n_{\alpha\circ} + \lambda n_{\alpha 1})(\mathbf{V}_{\alpha\circ} + \lambda \mathbf{v}_{\alpha\mathbf{1}}) = Q_\alpha - \beta (n_{\alpha\circ} + \lambda n_{\alpha 1})^2 \tag{2.31}$$

Ignoring the second and higher order terms (terms containing λ^2, λ^3 etc.), and neglecting electron inertia, the zero order momentum equation in (2.30) can be written as,

$$0 = n_{\alpha\circ} q_\alpha (\mathbf{E}_\circ + \mathbf{V}_{\mathbf{D}\alpha} \times \mathbf{B}) - \nabla P_{\alpha\circ} - n_{\alpha\circ} m_\alpha \nu_\alpha (\mathbf{V}_{D\alpha} - \mathbf{U}) \tag{2.32}$$

Equating the first order term equation in the expansion (order of λ) in (2.30) to zero,

$$\begin{aligned} n_{\alpha\circ} m_\alpha \left(\frac{\partial \mathbf{v}_{\alpha 1}}{\partial t} + \mathbf{V}_{\mathbf{D}\alpha} \cdot \nabla \mathbf{v}_{\alpha\mathbf{1}} \right) &= n_{\alpha 1} q_\alpha (\mathbf{E}_\circ + \mathbf{V}_{\mathbf{D}\alpha} \times \mathbf{B}) + n_{\alpha\circ} q_\alpha (-\nabla \mathbf{\Phi} + \mathbf{v}_{\alpha\mathbf{1}} \times \mathbf{B}) \\ &- \nabla p_{\alpha 1} - n_{\alpha\circ} m_\alpha \nu_\alpha \mathbf{v}_{\alpha 1} - n_{\alpha 1} m_\alpha \nu_\alpha (\mathbf{V}_{D\alpha} - \mathbf{U}) \end{aligned} \tag{2.33}$$

Combing (2.32) and (2.33), the zeroth and first order terms in the momentum equation expansion,

$$n_{\alpha\circ}m_\alpha\left(\frac{\partial \mathbf{v}_{\alpha 1}}{\partial t}+\mathbf{V}_{\mathbf{D}\alpha}\cdot\nabla\mathbf{v}_{\alpha 1}\right) = n_{\alpha\circ}q_\alpha(-\nabla\mathbf{\Phi}+\mathbf{v}_{\alpha\mathbf{1}}\times\mathbf{B})-\nabla p_{\alpha 1} + \frac{n_{\alpha 1}}{n_{\alpha\circ}}\nabla P_{\alpha\circ}-n_{\alpha\circ}m_\alpha\nu_\alpha\mathbf{v}_{\alpha 1} \tag{2.34}$$

Following similar procedures used for the momentum equation linearization, the zeroth and first order continuity equations become,

$$\frac{\partial n_{\alpha\circ}}{\partial t}+\nabla\cdot(n_{\alpha\circ}\mathbf{V}_{\mathbf{D}\alpha})=Q_\alpha-\beta n_{\alpha\circ}^2 \tag{2.35}$$

$$\frac{\partial n_{\alpha 1}}{\partial t}+\nabla\cdot(n_{\alpha\circ}\mathbf{v}_{\alpha\mathbf{1}})+(\mathbf{V}_{\mathbf{D}\alpha}\cdot\nabla)n_{\alpha 1}=-2\beta n_{\alpha\circ}n_{\alpha 1} \tag{2.36}$$

Presuming that nonlocal effects might not be important in the development of instabilities, the perturbed quantities in (2.27) can be assumed to have a plane wave solution, $\sim\exp[i(\mathbf{k}\cdot\mathbf{r}-\omega t)]$, where $\mathbf{k}$ and ω are wave vector and frequency, respectively.

The following notations and assumptions will be employed: the coordinates (x,y,z), in the zonal, north, and vertical directions, respectively, with, $(\hat{x},\hat{y},\hat{z})$, unit vectors in the respective direction, $n_e\simeq n_i=n_\circ$, and $n_{e1}\simeq n_{i1}=n_1$, a westward propagating wave, $\mathbf{k}=k\hat{x}$, the background ionosphere does not vary temporally, the background plasma drifts in the zonal direction. Some of these assumptions are made for mathematical simplicity and the generality of the results will not be lost.

The complex wave frequency is described as $\omega=\omega_k+i\gamma_k$, where ω_k and γ_k are the frequency and growth rate, respectively.

Applying the above set of assumptions to (2.34) and to the first order continuity

equation (2.36), we obtain,

$$\begin{aligned} -[i(\omega - kV_{D\alpha}) - \nu_\alpha](v_{\alpha 1x}\hat{x} + v_{\alpha 1z}\hat{z}) &= -ik\frac{q_\alpha}{m_\alpha}\Phi\hat{x} + \Omega_\alpha(-v_{\alpha 1x}\hat{z} + v_{\alpha 1z}\hat{x}) \\ &- ik\frac{\gamma_\alpha \kappa_B T_{\alpha\circ}}{m_\alpha}\frac{n_{\alpha 1}}{n_{\alpha\circ}}\hat{x} \end{aligned} \tag{2.37}$$

$$-i(\omega - kV_{D\alpha})\frac{n_{\alpha 1}}{n_{\alpha\circ}} + ikv_{\alpha 1x} + \frac{1}{n_{\alpha\circ}}\frac{dn_{\alpha\circ}}{dz}v_{\alpha 1z} = -2\beta n_{\alpha\circ}\frac{n_{\alpha 1}}{n_{\alpha\circ}} \tag{2.38}$$

Resolving (2.37) into its component and writing both (2.37) and (2.38) for the electron and ion species, we get a system of linear simultaneous equations with unknowns, v_{e1x}, v_{e1z}, v_{i1x}, Φ, and $\frac{n_1}{n_\circ}$.

$$\begin{aligned} ikv_{e1x} + \frac{1}{L_{n_{\circ z}}}v_{e1p} + [2\beta n_\circ - i(\omega - kV_{De})]\frac{n_1}{n_\circ} &= 0 \\ ikv_{i1x} + [2\beta n_\circ - i(\omega - kV_{Di})]\frac{n_1}{n_\circ} &= 0 \\ \nu_e v_{e1x} + \Omega_e v_{e1z} - ik\frac{e}{m_e}\Phi + ik\frac{\gamma_e \kappa_B T_{e\circ}}{m_e}\frac{n_1}{n_\circ} &= 0 \\ -\Omega_e v_{e1x} + \nu_e v_{e1z} &= 0 \\ +[i(\omega - kV_{Di}) - \nu_i]v_{i1x} - ik\frac{e}{m_i}\Phi - ik\frac{\gamma_i \kappa_B T_{i\circ}}{m_i}\frac{n_1}{n_\circ} &= 0 \end{aligned} \tag{2.39}$$

In writing the above set of equations, we have assumed the vertical perturbed ion motion to be zero. The vertical density gradient scale length of the background plasma is defined as $\frac{1}{L_{n_{\circ z}}} = \frac{1}{n_\circ}\frac{dn_\circ}{dz}$.

The nontrivial solution of the above system of equations is obtained by equating the determinant of the coefficient matrix to zero from which ω_k and γ_k can be determined.

The Doppler frequency can be derived from,

$$\begin{aligned} \omega_k - kV_{De} + \Psi_\circ(\omega_k - kV_{Di}) &= \frac{1}{kL_{n_{\circ z}}\Omega_i}\left(\left[(\omega_k - kV_{Di})^2 - k^2C_s^2\right]\right) \\ &- \frac{1}{kL_{n_{\circ z}}\Omega_i}\nu_i(\gamma_k + 2\beta n_\circ) \end{aligned} \tag{2.40}$$

where $C_s^2 = \frac{\kappa(\gamma_e T_{e\circ} + \gamma_i T_{i\circ})}{m_i}$, C_s is the ion acoustic speed.

Assuming further that the growth rate to be much less than both the wave oscillation frequency, $\gamma_k \ll \omega_k$, and the ion collision frequency, $\gamma_k \ll \nu_i$, and using (2.43) in (2.40), the Doppler shift can be written as,

$$\omega_k - kV_{De} \simeq -\Psi_\circ \left(1 + \frac{\Omega_e^2}{\nu_e^2} \frac{1}{k^2 L_{n_{\circ z}}^2}\right) (\omega_k - kV_{Di}) \tag{2.41}$$

In cases of radar observation at the Jicamarca Radio Observatory, wavelengths of interest (meter scale) are much less than the background gradient scale length, $\frac{1}{kL_{n_{\circ z}}} \ll 1$. So, despite the fact that $\Omega_e \simeq 100\nu_e$ in the electrojet region, Doppler velocities of a westward propagating plasma irregularity can be derived from (2.41),

$$\frac{\omega_k}{k} \approx \frac{(V_{De} + \Psi_\circ V_{Di})}{1 + \Psi_\circ} \tag{2.42}$$

where the definitions $\Psi_\circ = \frac{\nu_e \nu_i}{\Omega_e \Omega_i}$ was used.

Applying the above assumptions to the solution of the system of equations (2.39), the growth rate can be written as,

$$\gamma_k \simeq \frac{\Psi_\circ}{(1 + \Psi_\circ)} \left(\frac{1}{\nu_i} \left[(\omega_k - kV_{Di})^2 - k^2 C_s^2\right] + \frac{\Omega_e}{\nu_e} \frac{1}{kL_{n_{\circ z}}} (\omega_k - kV_{Di})\right) - 2\beta n_\circ \tag{2.43}$$

The gradient scale length needs to be positive, $L_{n_{\circ z}} > 0$, for growth; otherwise the second term in (2.43) will contribute negatively and cause damping.

The results of the linear theory explain some of the behavior of short wavelength electrojet irregularities. Due to decreasing electron/ion collision frequencies with altitude, the parameter $\Psi_\circ$ decreases, and the Doppler velocity increases with altitude and approaches the limiting velocity, the electron drift velocity, at the top of the electrojet. The linear dispersion relation for electrojet irregularities has been instrumental for interpreting the Doppler spectra observed at the JRO.

2.11.2 Farley-Buneman instability

A straight forward generalization of the frequency (2.42) and growth rate (2.43) of the irregularities in terms of vector relative drift between ions and electrons $\mathbf{V_D} = \mathbf{V_{De}} - \mathbf{V_{Di}}$, can be written as [*Fejer et al*, 1975],

$$\omega_k \simeq \frac{\mathbf{k} \cdot \mathbf{V_D}}{1 + \Psi} + \mathbf{k} \cdot \mathbf{V_{Di}} \tag{2.44}$$

$$\gamma_k \simeq \frac{1}{1 + \Psi} \left[\frac{\Psi}{\nu_i} \left(\left(\frac{\mathbf{k} \cdot \mathbf{V_D}}{1 + \Psi} \right)^2 - k^2 C_s^2 \right) + \frac{\nu_i k_\perp}{\Omega_i L_{n_{\circ z}} k^2} \left(\frac{\mathbf{k} \cdot \mathbf{V_D}}{1 + \Psi} \right) \right] - 2\beta n_\circ \tag{2.45}$$

where Ψ is the anisotropy factor which is defined as,

$$\Psi = \Psi_\circ \left(\frac{k_\perp^2}{k^2} + \frac{\Omega_e^2}{\nu_e^2} \frac{k_\parallel^2}{k^2} \right) \tag{2.46}$$

Electrojet irregularities are attributed to Farley-Buneman and gradient-drift instabilities. In the presence of initial perturbations, the two mechanisms amplify the perturbation to generate irregularities in the electrojet. They are associated with ion inertia and a plasma density gradient, respectively. The Farley-Buneman instability is excited if the component of the electron-ion relative drift in the direction of propagation of irregularities exceeds the ion acoustic speed, $\mathbf{k} \cdot (\mathbf{V_{De}} - \mathbf{V_{Di}}) > |\mathbf{k}| C_s (1 + \Psi_\circ)$. The linear theory, however, does not give justification as to why the Doppler velocities of radar echoes from the Farley-Buneman instabilities (type I radar echoes) are saturated at the ion-acoustic threshold speed.

Electrons should stream through ions with a speed greater than the ion acoustic speed to cause the two-stream instability. A polarization electric field is set up due to a relative motion between the $\mathbf{E} \times \mathbf{B}$ drifting electrons and the collisional ions. The polarization field arises so that the lagging ions flow with the fast streaming electrons and the plasma remains quasineutral as a result. The slowly moving

ions, however, keep accumulating because of their inertia, giving rise to growing perturbations in the local ion density. This leads to an increase in the perturbed polarization electric field. The overall process leads to an increase in the amplitude of the perturbed quantities and hence to instability provided that the process takes place faster than the rate of ion diffusion [*Farley*, 1963; *Buneman*, 1963].

The Farley-Buneman instability mechanism can be viewed as a competition between two dynamic processes, ion diffusion (which causes wave decay), and ion inertia (which triggers instability growth). The pressure gradient force acts in such a way that plasma density gradients are annhilated, meanwhile, due to their inertia, the slowly travelling ions tend to accumulate on top of the perturbation and the background plasma to generate the Farley-Buneman instability.

The first term in the square bracket in equation (2.45) is associated with the growth mechanism of the modified two-stream (Farley-Buneman) instability. Using typical E region ionospheric parameters to estimate the first term in (2.45), we can deduced that, for relative drifts $\mathbf{V_D}$ exceeding the ion acoustic speed even by a few meter per second, two-stream instabilities having wavelengths as large as 10 m might grow without experiencing damping due to recombination (the third term in (2.45)).

2.11.3 Gradient-drift instability

The gradient-drift mechanism is the other possible cause for instability in the equatorial electrojet. As the name implies, the gradient of the background density plays a role in the generation of instability. This is shown by the second term in (2.43).

According to the second term in equation (2.45), the gradient-drift instability

grows when the vertical density gradient scale length, $L_{n_{\circ z}}$, has a positive component in the direction of the driving electric field. This condition is satisfied during the daytime, for example, where $L_{n_{\circ z}}$ (below the E peak) is parallel to the vertical polarization field. In addition, using typical ionospheric parameters to estimate (2.45), we can deduce from the linear theory that: gradient-drift irregularities having wavelengths greater than about 50 m are excited by the linear instabilities mechanism, however, meter scale irregularities are damped.

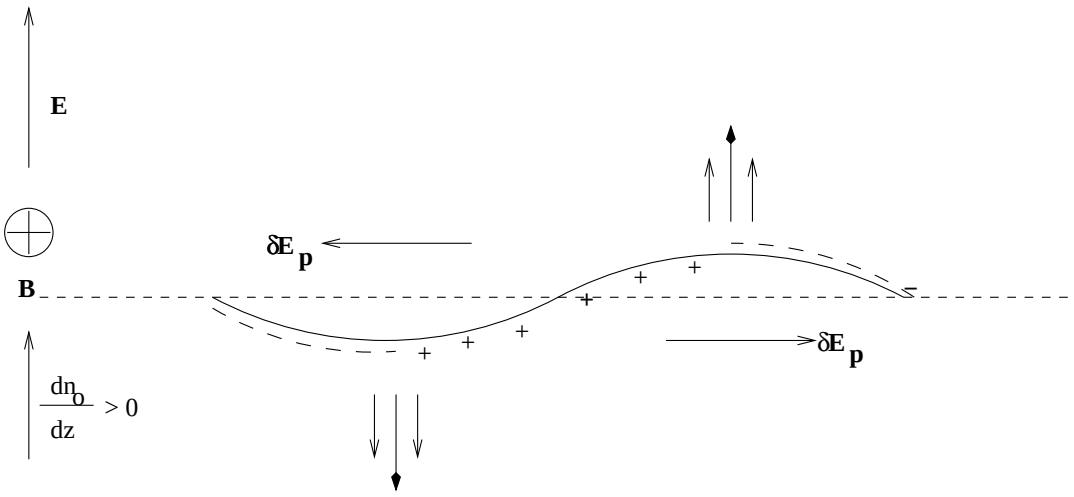

Figure 2.8: Schematic representation of the Gradient-Drift instability mechanism. A vertical background polarization electric field, which generally corresponds to daytime conditions, is assumed. The geomagnetic field is directed into the page. Vertical density gradients are positive.

A schematic representation of the physical mechanism for the gradient-drift instability is shown in Figure 2.8. The horizontal broken line represents an idealized unperturbed ionospheric state and corresponds to a contour of plasma density. The vertical electric field, **E**, is directed upward, which corresponds to daytime

electrojet conditions. The background density gradient is also directed upwards, $\frac{dn_\circ}{dz} > 0$, which is actually the case below the E region peak, which is at about 108±3 km altitude depending on solar conditions. A small amplitude sinusoidal perturbation is applied to the density gradient as shown in Figure 2.8. In response to the perturbation, the given vertical electric field, and density gradient configurations, electrons perform a Hall drift, whereas ions are marginally magnetized and remain relatively stationary or move slowly in the direction of the applied forces resulting in a relative drift. The sinusoid is polarized, and a horizontal polarization electric field, $\delta\mathbf{E_p}$, is generated, which changes polarity alternatively as shown in Figure 2.8. This perturbation field will cause the enhanced regions to drift downward and the depleted regions upward, leading to a situation where the amplitude of both the enhanced and depleted regions grows relative to the ambient plasma density. However, if we assume the orientation of the electric field to be in a direction anti-parallel to the background density gradient (or there is no parallel component in the gradient direction), growth will be hampered.

2.11.4 The anisotropy factor

Equation (2.46) can be written as (2.47) in terms of wavenumber components parallel and perpendicular to the magnetic field, $k_\parallel = k\sin\varphi$ and $k_\perp = k\cos\varphi$, respectively, φ being the angle measured from the direction perpendicular to the magnetic field in the north-south plane.

$$\Psi = \Psi_\circ \left(\cos^2\varphi + \frac{\Omega_e^2}{\nu_e^2}\sin^2\varphi\right) \tag{2.47}$$

Perpendicular to the geomagnetic field ($\varphi = 0$), $\Psi = \Psi_\circ$. However, off perpendicular, a small φ can make significant difference since $\Omega_e/\nu_e \simeq 100$ in the

electrojet region. The effect is to suppress growth of electrojet instabilities according to equation (2.45). For $\varphi = 1°$, for example, $\Psi \simeq 4\Psi_\circ$. A contour plot of equation (2.47) is displayed in Figure 2.9. The calculation was made using collision frequency [*Richmond*, 1972] and geomagnetic field [*National Space Science Data Center*, 2002] models for a realistic equatorial E region. The value of the anisotropy factor, however, increases dramatically away from the perpendicular direction with increasing φ. Consequently, plasma irregularities generated by the Farley-Buneman and gradient drift instabilities prefer propagating in a plane orthogonal or nearly orthogonal to the geomagnetic field.

2.11.5 Long wavelength gradient drift electrojet irregularities

Excluding the assumption that the growth rate is much smaller than the frequency and neglecting ion inertial effects and diffusion, the linear theory can be extended to long wavelengths. Applying these procedures, the frequency of long wavelength irregularities can be derived from (2.40) and (2.43),

$$\omega_k = \frac{kV_{De}}{1+\Psi_\circ}\left(1+\frac{k_\circ^2}{k^2}\right)^{-1} \tag{2.48}$$

Where $k_\circ = \left(\frac{\nu_i}{\Omega_i L_{n_\circ z}}\right)(1+\Psi_\circ)^{-1}$ is a chracteristic wave number. Typically, at the center of the electrojet where $\Psi_\circ \simeq 0.3$ and $\nu_i \simeq 30\Omega_i$, $k_\circ$ corresponds to a length scale $\lambda_\circ \simeq \frac{L_{n_\circ z}}{4}$. Using the above assumptions in (2.43) in combination with (2.48), the growth rate for large scale irregularities becomes,

$$\gamma_k = \frac{k_\circ V_{De}}{1+\Psi_\circ}\left(1+\frac{k_\circ^2}{k^2}\right)^{-1} - 2\beta n_\circ \tag{2.49}$$

In the limit where the wavelength of interest is much less than the characteristic wavelength, $k_\circ \ll k$, equations (2.42) and (2.43) would be recovered. The

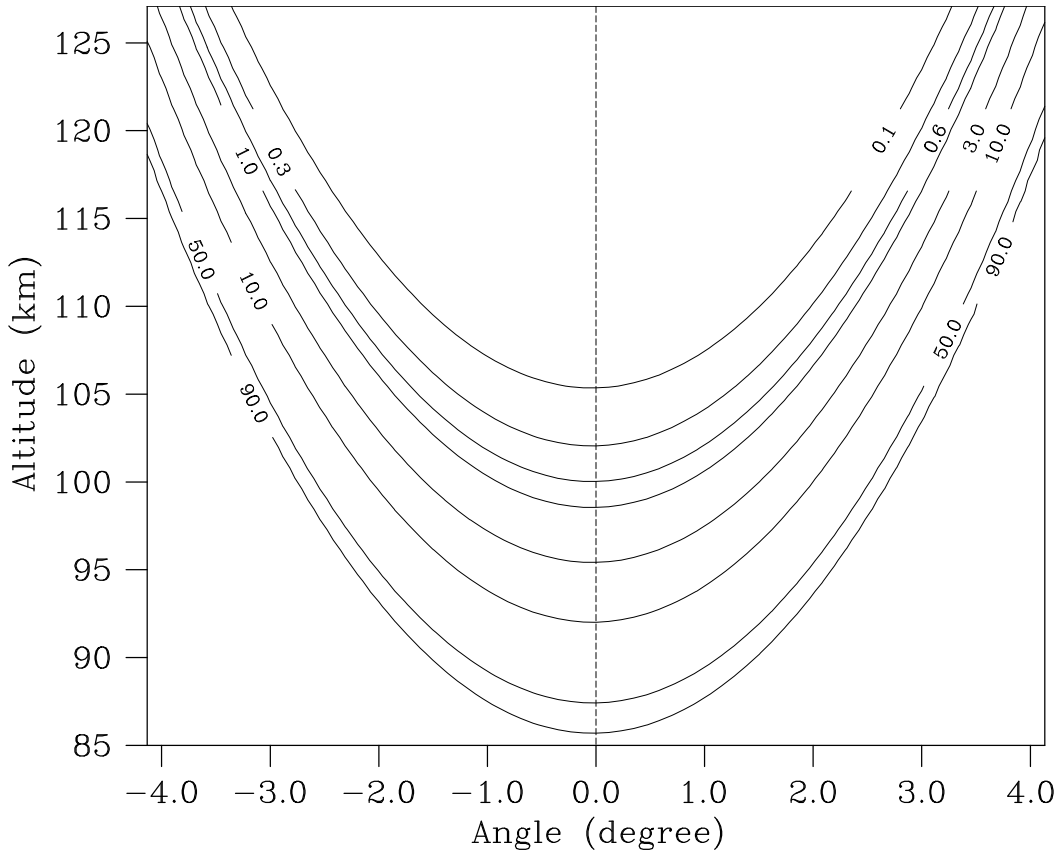

Figure 2.9: A contour plot of the anisotropy factor, Ψ, versus altitude and an angle φ, measured from the direction perpendicular to the geomagnetic field.

relationships (2.48) and (2.49) were found by *Kudeki et al* [1982], *Farley* [1985], and *Kudeki et al* [1987].

Such large scale irregularities, traveling in the east-west direction in the electrojet were observed by tracking the spatial (east-west) location of upward and downward moving short wavelength irregularities using radar interferometery at Jicamarca [*Farley et al*, 1981; *Kudeki et al*, 1982].

Taking $k \simeq k_\circ$, which might be in the vicinity of 2 km, the horizontal Doppler

velocity, (2.48), becomes,

$$\frac{\omega_k}{k} \simeq \frac{1}{2}\left(\frac{V_{De}}{1+\Psi_\circ}\right) \tag{2.50}$$

This shows that the velocity of propagation of long wavelength irregularities is smaller by one-half than the background electron drift, an analysis which was confirmed by the interferometer observations. For wavelengths much larger than $\lambda_\circ$, large scale irregularities might be damped during the day where the rate of recombination is high, according to (2.49). Large scale gradient drift irregularities are important for explaining the physical mechanisms behind small scale electrojet irregularities, as discussed below.

2.11.6 Two-step theory

What are the mechanisms for exciting upward and downward propagating short wavelength irregularities? What is the mechanism for exciting irregularities that cause type II radar echoes? A two-step theory involving the interaction between large- and small-scale waves is thought to be at work [*Farley and Balsley*, 1973; *Sudan et al*, 1973; *Farley et al*, 1981; *Kudeki et al*, 1982, 1987]. Polarization electric fields generated by large scale turbulence in the electrojet are believed to drive vertical and oblique short wavelength irregularities. Short wavelength vertically and obliquely traveling disturbances are commonly observed using the main and oblique antennas at Jicamarca, respectively. Two-step Farley-Buneman irregularities are driven if the amplitude of the primary wave electric fields are large enough to satisfy the ion-acoustic threshold condition. The perturbation field should have a positive component along a horizontal density gradient in order that secondary gradient drift waves are generated. The Doppler frequencies of

short wavelength irregularities causing type II echoes are generally taken to be governed by the linear theory.

The Doppler velocity of the vertical type I echoes coincides with the ion-acoustic threshold speed given by the linear instability theory. The Doppler velocities of the oblique type I echoes, however, may differ from the ion-acoustic speed, due to neutral wind effects. In the case of oblique observation, therefore, explaining the Doppler shift of type I echoes is not straight-forward. Do they saturate following the linear theory growth condition? In this dissertation, we shed light on Doppler shift characteristics of oblique type I echoes by evaluating them in light of zonal winds calculated by through a modelling approach (described in Chapter 5) and the linear instability theory.

2.11.7 Wave mode coupling

Long wavelength irregularities are commonly present below the E region peak where density gradients are positive, but they are nonexistent above the E region peak. In light of this and the two-step process discussed above, the following questions are raised: What are the causes for echoes above the E region peak and in the bottomside electrojet where collisions are frequent? What triggers type II echoes above the E region peak where the linear gradient drift instability mechanism likely fails? Nonlinear wave-wave interactions, in line with the discussion provided in *Dougherty and Farley* [1967], *Chen* [1984], and *Kudeki et al* [1987] are possible candidates for explaining these processes. Wave-wave coupling between wave triplets in the electrojet would lead to excitation and decay of wave modes. The mode triples undergoing interaction normally have matching oscillation frequency and wave vector characteristics, $\omega = \omega_1 + \omega_2$ and $\mathbf{k} = \mathbf{k_1} + \mathbf{k_2}$, respectively. This

means, an unstable wave mode, $(\omega, \mathbf{k})$, could excite two decaying modes, $(\omega_1, \mathbf{k_1})$ and $(\omega_2, \mathbf{k_2})$. Another possible wave-wave interaction scenario is that two unstable modes, $(\omega_1, \mathbf{k_1})$ and $(\omega_2, \mathbf{k_2})$, could excite one decaying wave mode, $(\omega, \mathbf{k})$.

2.11.8 Next chapter

By extending the review done in this chapter, the subsequent chapter will explore the various ionospheric current models of the low latitude ionosphere. The review will show the major developments of ionospheric current modelling from the early times of ionospheric research until the present time.

Chapter 3

Ionospheric current models

3.1 Introduction

As mentioned in Chapter 2, analytical and numerical models of the equatorial electrojet were not available before the 1950s'. Since then, observational as well as modelling efforts have intensified significantly. The major contributions of the theoretical/computational electrojet studies have been to model the polarization electric fields, to numerically reproduce the vertical profile of the equatorial electrojet current measured in rocket flight experiments, and to model growth mechanisms of electrojet plasma irregularities.

In the present chapter, some of the modeling efforts will be reviewed. Specifically, we will review the following two and three dimensional ionospheric models: (i) the thin-shell dynamo layer conductivity electrojet model [*Untiedt*, 1967; *Sugiura and Cain*, 1966; *Forbes*, 1981], (ii) a flux tube integrated two dimensional ionosphere model based on equipotential magnetic field lines [*Haerendel and Eccles*, 1992; *Haerendel et al*, 1992; *Eccles*, 1998a, b], (iii) a three dimensional model which assumes equipotential geomagnetic field lines [*Richmond*, 1973a; *Hysell et al*, 2002], and (iv) a three dimensional electrostatic potential model which does not make the equipotential approximation [*Richmond*, 1973a; *Hysell et al*, 2002]. A three dimensional potential model in a magnetic dipole coordinate system for the low latitude ionosphere will be highlighted here and will be described in detail in Chapter 5.

3.2 The current density

A compact expression for ionospheric current density derived in (r, θ, ϕ) coordinates, a vertical, a north-south, and an east-west coordinates, respectively, [*Forbes*, 1981] is given by,

$$\mathbf{J} = \hat{\mathbf{\Sigma}} \cdot (\mathbf{E} + \mathbf{U} \times \mathbf{B}) \tag{3.1}$$

where the coefficient of the current drivers in (3.1), the conductivity tensor, is defined as,

$$\hat{\mathbf{\Sigma}} = \begin{pmatrix} \sigma_{\phi\phi} & \sigma_{\phi\theta} & \sigma_{\phi r} \\ \sigma_{\theta\phi} & \sigma_{\theta\theta} & \sigma_{\theta r} \\ \sigma_{r\phi} & \sigma_{r\theta} & \sigma_{rr} \end{pmatrix} \tag{3.2}$$

Representing the magnetic dip angle by I, the elements of the above tensor are defined as,

$$\begin{aligned} \sigma_{\phi\phi} &= \sigma_P \\ \sigma_{\theta\phi} = -\sigma_{\phi\theta} &= -\sigma_H \sin I \\ \sigma_{r\phi} = -\sigma_{\phi r} &= -\sigma_H \cos I \\ \sigma_{\theta r} = \sigma_{r\theta} &= (\sigma_P - \sigma_\circ) \sin I \cos I \\ \sigma_{\theta\theta} &= \sigma_P \sin^2 I + \sigma_\circ \cos^2 I \\ \sigma_{rr} &= \sigma_\circ \sin^2 I + \sigma_P \cos^2 I \end{aligned} \tag{3.3}$$

The Pedersen, σ_P, Hall, σ_H, and longitudinal, $\sigma_\circ$, conductivities are defined by equations (2.7) through (2.9).

3.3 The thin-shell dynamo electrojet model

In the thin-shell dynamo model, horizontal ionospheric currents are restricted to flow in a thin slab of the dynamo region between the altitude region of about 90

and 160 km. The thin-shell dynamo model assumes that vertical current does not flow in the E region.

Neglecting pressure gradient and gravity driven currents for simplicity for the moment, and applying the assumptions that, $J_r = 0$, vertical currents do not flow, the east-west, J_ϕ, and north-south, J_θ, components of the current density can be calculated from (3.1),

$$\begin{aligned} J_\phi &= \Sigma_{\phi\phi} E_\phi + \Sigma_{\phi\theta} E_\theta \\ J_\theta &= -\Sigma_{\phi\theta} E_\phi + \Sigma_{\theta\theta} E_\theta \end{aligned} \tag{3.4}$$

where the so called layer conductivities are defined in terms of the conductivities given in (3.3),

$$\begin{aligned} \Sigma_{\phi\phi} &= \sigma_{\phi\phi} + \frac{\sigma_{\phi r}^2}{\sigma_{rr}}, \\ \Sigma_{\phi\theta} &= \sigma_{\phi\theta} - \frac{\sigma_{\phi r}\sigma_{r\theta}}{\sigma_{rr}}, \\ \Sigma_{\theta\theta} &= \sigma_{\theta\theta} - \frac{\sigma_{\theta r}^2}{\sigma_{rr}} \end{aligned} \tag{3.5}$$

By neglecting, E_θ, the electric field in the magnetic north-south direction as well as the role of neutral winds, *Sugiura and Cain* [1966] calculated the equatorial electrojet current, $J_\phi(\theta, r)$, from (3.4),

$$J_\phi(\theta, r) = \left(\sigma_{\phi\phi} + \frac{\sigma_{\phi r}^2}{\sigma_{rr}} \right) E_\phi \tag{3.6}$$

The objectives of their calculation were to model the latitudinal and altitudinal profiles of the equatorial electrojet (and the magnetometer deflection it causes) in the various longitude sectors, thereby reproducing ground and rocket measurements of currents and the resulting magnetic field.

In the cases where the magnetic dip angle is negligible, $I = 0$, and the first

term of (2.20) can be reproduced from (3.6),

$$J_\phi(\theta, r) = \sigma_P \left(1 + \frac{\sigma_H^2}{\sigma_P^2}\right) E_\phi \tag{3.7}$$

The model provided in *Sugiura and Cain* [1966] generally reproduces the shape of electrojet profiles but fail to match the amplitude and width of latitudinal and vertical profiles of the measured current.

Untiedt [1967] pointed out that in order to make a self-consistent model of the low latitude ionosphere, vertical current, which was ignored by *Sugiura and Cain* [1966], must be allowed to flow. The neglect of vertical current violates the divergence free current constraint in the ionosphere. Close to the magnetic dip equator, the background zonal electric field, E_ϕ, zonal, and meridional winds generate little current in the north-south direction. Off the magnetic equator, however, current can flow in the north-south direction, driven by a zonal electric field, E_ϕ can drive current for example. This behavior makes the current in the north-south direction divergent. Given that J_ϕ changes slowly compared to J_θ current divergence results in the ionosphere, $\nabla \cdot \mathbf{J} = \frac{1}{r \sin\theta}\left(\frac{\partial J_\phi}{\partial \phi} + \frac{\partial(\sin\theta J_\theta)}{\partial \theta}\right) \neq 0$.

To suppress nondivergent current, flow of vertical current is required by the system [*Untiedt*, 1967]. The assumptions above, (2.20) and (3.4) are therefore violated. By allowing vertical current flow, the electrojet model developed by *Untiedt* [1967] provided improved results in reproducing the electrojet current. Despite the improvements, the discrepancy between the amplitude, width and location of the peak of the calculated and measured current profiles were not fully resolved.

Forbes and Lindzen [1976a, b] and *Forbes* [1981] solved the height integrated thin shell dynamo equation and found out the shortcomings of thin shell model in reproducing the low latitude ground magnetic field perturbations. *Forbes and*

Lindzen [1976b] allowed for vertical current flow and solved the complete three dimensional problem resulting from the solenoidal current equation but did not fully reproduce magnetic field observations, however, the result were better than the thin shell model.

Heelis et al [1974] solved height integrated two dimensional potential equation and derived temporal properties of the zonal and vertical electric fields at the magnetic equator. The zonal and vertical electric fields were found to have diurnal characteristics with enhancement of the vertical plasma drift before reversal. *Heelis et al* [1974] also predicted the horizontal F region plasma velocity to have vertical shear in the flow during the evening.

3.4 A two dimensional magnetic flux tube integrated equatorial ionosphere model

A two dimensional ionosphere model has been derived by integrating the current divergence free equation along geomagnetic field lines [*Haerendel and Eccles*, 1992; *Haerendel et al*, 1992; *Eccles*, 1998a, b]. The collapse of the three dimensional physical ionosphere to a two dimensional computational ionosphere which lives in the magnetic equatorial plane is made possible by assuming equipotential magnetic field lines, $\mathbf{E}_{\parallel} \simeq \mathbf{0}$, in equation (2.6). The equipotential approximation applies for cross field scales larger than about a kilometer. The integrated ionosphere model was employed by *Haerendel and Eccles* [1992]; *Haerendel et al* [1992] to explain the prereversal enhancement of the zonal electric field and shear in the F region zonal plasma flow.

In order to investigate current and electric field relationships in the equatorial

electrojet region, which essentially lies within the narrow region of altitudes, from 75 to 150 km, the polar coordinate representation of the integrated ionosphere, (r, ϕ), is replaced by a Cartesian system, (h, t), standing for the equatorial altitude and local time, respectively [*Haerendel and Eccles*, 1992]. Using elements of the Cartesian coordinate system, the current divergence free equation of the integrated ionosphere becomes,

$$\frac{\partial J_L}{\partial h} + \frac{1}{v_r}\frac{\partial J_\phi}{\partial t} = 0 \tag{3.8}$$

where (J_L, J_ϕ) are components of the integrated current density vector in the magnetic equatorial plane, the horizontal distance is given by $v_r t$, and v_r is the Earth's rotation speed in the magnetic equatorial plane.

The components J_L and J_ϕ are integrated vertical and zonal current densities, respectively. The vertical component, J_L, is a sum of the projections of local meridional currents in the direction perpendicular to the magnetic field. The current components are expressed in terms of integrated parameters in the two dimensional plane: ionospheric conductivities, Σ's, zonal neutral wind, U_ϕ, vertical (E_L) and zonal (E_ϕ) electric fields,

$$\begin{aligned} J_L &= \Sigma_P \left(E_L + BU_\phi^P\right) - \Sigma_H E_\phi \\ J_\phi &= \tilde{\Sigma}_P E_\phi + \Sigma_H \left(E_L + BU_\phi^H\right) \end{aligned} \tag{3.9}$$

3.4.1 The equatorial evening *E* region current

Substituting (3.9) in (3.8) and integrating the integrated current from 75 km to 150 km altitudes leads to,

$$J_L(150,t) - J_L(75,t) = -\frac{1}{v_r}\frac{\partial}{\partial t}\int_{75}^{150}\left(\Sigma_c E_\phi + \frac{\Sigma_H}{\Sigma_P}J_L(h,t)\right)dh \tag{3.10}$$

$$\Sigma_c = \tilde{\Sigma}_P + \frac{\Sigma_H^2}{\Sigma_P}$$

Considering the temporal properties of the inputs, (i) the zonal electric field, E_φ, and (ii) integrated conductivities are defined in terms of integrated plasma densities (whose temporal behavior is related to plasma transport and rate of plasma loss/production by the continuity equation), *Haerendel and Eccles* [1992] numerically solved the integral equation (3.10) and modeled the height integrated vertical current as a function of time in the equatorial E region. They found that the vertical current at the top of the E region to be enhanced after sunset for a couple of hours and to decrease its magnitude after field reversal.

Equation (3.10) suggests that divergence of the electrojet current leads to a current in the vertical direction and out of the equatorial E region. This diversion of the electrojet current to the vertical is mainly a consequence of a reduction of the integrated Cowling conductivity, Σ_c, at the solar terminator. A zonal polarization electric field stronger than the background needs to be set up in this scenario to keep the current system divergence free. This electric field further speeds the vertical plasma uplift.

This prompted *Haerendel and Eccles* [1992] to draw the following hypothesis regarding the evening enhancement of zonal electric field: the equatorial electrojet current divergence at the terminator and F region vertical current demands are the mechanisms for the prereversal enhancement of the zonal electric field in the equatorial ionosphere. However, the feeding of vertical current from the E region to the bottomside F just mentioned is more of a consequence of the electrojet current divergence rather than a cause for enhancement of the zonal field.

It can be clearly seen from the above analysis how the divergence of the equatorial electrojet leads to zonal electric field enhancement in the equatorial E and bottomside F regions. However, it is not clear how this mechanism explains ver-

tical plasma velocity enhancement in the rest of the F region during the evening, especially in a situation where the plasma flowing out of the electrojet region meets a strong downward electric field generated by the F region dynamo. The downward electric field causes a zonal plasma drift. The F region zonal electric field, therefore, needs to be enhanced locally to keep the vertical plasma flow through the F region and toward the topside. Modeling efforts in this regard includes center on two theories: In one, the F region dynamo and the magnetically connected off-equatorial E region work together to cause enhancement of the zonal field [*Farley et al*, 1986]: In the other, the rapid change in the magnitude and direction of the F region dynamo during the early evening (edge effects) gives rise to the zonal field enhancement [*Eccles*, 1998b]. We plan to conduct further investigation into the physical mechanisms of the zonal field enhancement by analyzing the evening plasma dynamics of the equatorial F region in terms of the horizontal divergence of the evening vertical current, and the divergence of the zonal Pedersen current around the solar terminator.

3.4.2 Shear in the horizontal plasma flow

Polarization electric fields generated by the F region dynamo cause eastward plasma convection at night. In the lower F region through the peak, however, the dynamo effect is lessened due to a reduced neutral wind amplitude. In addition, the first and third terms in equation (3.11) further offset the downward electric field. It appears that the lower F region plasma may maintain the westward drift it had been doing during the day.

An integrated vertical polarization electric field expression can be derived from

the first of the integrated current equations (3.9),

$$E_L = \frac{\Sigma_H}{\Sigma_P} E_\phi - B U_\phi^P + \frac{J_L}{\Sigma_P} \tag{3.11}$$

Positive contributions to the vertical polarization field, E_L, in the lower F region come from the integrated downward Hall current and a vertical current coming out of the equatorial electrojet as shown by (3.11). This, combined with a reduction in the magnitude of the second term in (3.11), force a reversal of the vertical field to an upward direction implying westward plasma flow in the lower F region. This constitutes the origin of shear in the horizontal plasma convection in the evening equatorial ionosphere.

Haerendel et al [1992] made use of (3.11) to analyze shear in the F region evening horizontal plasma flow. By modeling the temporal and altitudinal dependence of the ionospheric parameters in the right hand side of (3.11), *Haerendel et al* [1992] calculated an altitude profile of the vertical electric field, E_L. The terms on the right hand side of (3.11) play a role in the shear generation. They showed a reversal in the vertical electric field around the F peak having a characteristics of an eastward plasma flow above the F peak and westward flow below. Their integrated model reproduced features of the evening vertical shears in the zonal plasma drifts observed at Jicamarca [*Kudeki et al*, 1981] and rocket ion cloud chemical release experiments reported in a review paper by *Fejer* [1981].

The two dimensional flux tube model [*Haerendel and Eccles*, 1992; *Haerendel et al*, 1992] offers additional insight into the physics of the equatorial ionosphere. The flux tube integrated model reproduces shear in plasma flow and contributes to the discussion of the prereversal enhancement of the zonal field. However, the integrated model is not helpful for studying latitudinal structures in electric fields and currents in the low latitude ionosphere. The integrated model is meant to ad-

dress large-scale motions in the ionosphere and therefore may not be suitable for studying local ionospheric dynamo processes such as meridional currents, etc. In addition, in the lower equatorial electrojet below about 100 km where the equipotential approximation breaks down [*Richmond*, 1973a; *Hysell et al*, 2002], results from the integrated model might be invalid.

3.5 Three dimensional electrojet model based on the equipotential approximation

In most of the solar-terrestrial environment, longitudinal conductivities are very large compared to transverse conductivities as shown in Figure 2.4. Parallel electric fields can therefore be negligible. Geomagnetic field lines can be treated as equipotential lines with the exception of the collisional lower ionosphere below about 100 km and in the particle acceleration region in the magnetosphere. Consequently potential differences originating from one region of space could be transported undiminished along magnetic field lines provided that the source electric fields are embeded in large scale plasma structures (kilometer scales and larger) [*Farley*, 1959, 1960].

In the ionosphere, the equation $\nabla \times \mathbf{E} = -\frac{\partial \mathbf{B}}{\partial t} \simeq 0$, is valid. Ionospheric electric fields can be therefore described by the electrostatic approximation.

Utilizing the equipotential and electrostatic approximations, assuming that the geomagnetic field can be represented by a dipole magnetic field, and carrying out flux tube integrations, *Richmond* [1973a, b] developed a three dimensional numerical model of the low latitude ionosphere that solves for the vector electric field and current density. The model is described below.

The current divergenceless equation can be written in integral form using Gauss' theorem as,

$$\int_{\tau} \nabla \cdot \mathbf{J} dV = \int_{\vartheta} \hat{n} \cdot \mathbf{J} dA = 0 \tag{3.12}$$

where the left hand side integral in (3.12) is carried out on a volume τ of the flux-tube shown schematically in Figure 3.1 and $\hat{n}$ is a unit vector in the direction of the outward normal to the bounding surfaces, ϑ, of the flux tube.

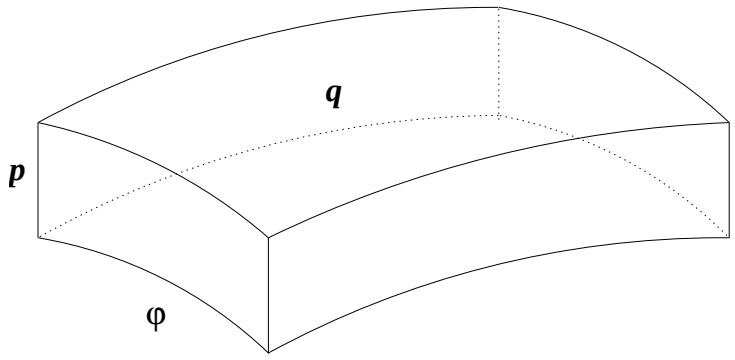

Figure 3.1: A sketch of the magnetic dipole coordinate system. The components p, q, and ϕ are perpendicular-vertical, parallel to magnetic field lines, and perpendicular-zonal components, respectively.

The magnetic dipole coordinate system consisting of the elements, (p, q, ϕ), is shown schematically in Figure 3.1. The geometric scale factors, (h_p, h_q, h_ϕ), transform the spherical coordinate system, (r, θ, ϕ), to the (p, q, ϕ) system. A detailed description of the dipole coordinate system, the geometric scale factors, and the merits of using the dipolar coordinates as applied to the solution of a three dimensional electrostatic potential problem in a realistic ionosphere will be presented in Chapter 5.

The flux tube shown in Figure 3.1 is bounded by p = constant, q = constant, and ϕ = constant surfaces. If the longitudinal slab is thin, the net current flow through the $p-q$ surface should be negligible. If the $p-\phi$ and lower $q-\phi$ surfaces lie below the nonconducting atmosphere, current flowing through those surfaces is also negligible. The flux tube is considered to be thin so that all the current through it passes through the p = constant surfaces. In the limit that the lower and upper p = constant surfaces coincide, the surface integral (3.12) reduces to,

$$d\phi \int_q J_p h_\phi h_q dq = C \tag{3.13}$$

where J_p is a current density component flowing perpendicular to the $q-\phi$ surfaces of the flux-tube, and C is a constant.

The constant in the right hand side of (3.13) is equal to the differential vertical E region current dI_p flowing in the differential element $d\phi$ at the base of the flux tube, since net vertical current exists in the electrojet [*Hysell et al*, 2002].

The vertical, J_p, and zonal, J_ϕ, current density components can be derived from the vector current density, (2.6), (pressure and gravity driven currents are ignored for the moment),

$$J_p = \sigma_P(E_p + uB) - \sigma_H(E_\phi - vB) \tag{3.14}$$

$$J_\phi = \sigma_P(E_\phi - vB) + \sigma_H(E_p + uB) \tag{3.15}$$

where $\mathbf{U} = (u, v, w)$ are zonal, vertical and meridional wind components, respectively. Near the magnetic equator, meridional winds, w, have negligible influences on the current system, $(\mathbf{U} \cdot \hat{\mathbf{b}}) \times \mathbf{B} \simeq \mathbf{0}$, since they are parallel to geomagnetic field lines.

Integrating (3.14) along magnetic field lines and using the relation in (3.13), we get,

$$\begin{aligned}\int_q J_p h_\phi h_q dq &= \int_q \sigma_P h_p E_p \frac{h_\phi h_q}{h_p} dq - \int_q \sigma_H E_\phi h_\phi h_q dq + \int_q (\sigma_P u + \sigma_H v) B h_\phi h_q dq \\ &= \frac{dI_p}{d\phi} \end{aligned} \tag{3.16}$$

Making use of electrostatic and equipotential approximation, $\mathbf{E}_\parallel$=0, the quantities $h_p E_p$ and $h_\phi E_\phi$ (curl free electric field equation) can be shown to be invariant along geomagnetic field lines. Making use of these invariances in (3.14), the vertical polarization electric field can be extracted and can be written as [*Richmond*, 1973a; *Hysell et al*, 2002],

$$E_p = \frac{h_\phi E_\phi \int_q \sigma_H h_q dq - \int_q (\sigma_P u + \sigma_H v) B h_\phi h_q dq + \frac{dI_p}{d\phi}}{h_p \int_q \sigma_p \frac{h_\phi h_q}{h_p} dq} \tag{3.17}$$

This causitive relationship describes the vertical polarization electric field in terms of four electric field drivers, namely, the background zonal electric field (the first term), dynamo fields generated by zonal and vertical wind fields (the second and third terms), and a net vertical current (the fourth term) flowing in the equatorial E region.

Richmond [1973a] has calculated E_p from (3.17), using zonal electric field, E_ϕ, conductivties, and winds as inputs. Using the calculated E_p, latitudinal and vertical structures of J_p and J_ϕ profiles were computed from (3.14) and (3.15), respectively, and the meridional current component was also calculated from $\nabla \times \mathbf{H} = \mathbf{J}$, where $\mathbf{H}$ is a perturbation magnetic field produced by ionospheric current $\mathbf{J}$. The model calculation generally agrees with a three dimensional formulation that does not make the equipotential approximation above 100 km altitude but departs below about 100 km. The vertical profile of the electrojet current calculated by

Richmond [1973a] was wider than the thin shell model and did not reproduce the current profiles measured by rockets.

Let us continue analyzing the flux tube integrated model equations to better understand current and dynamo relationships in the low latitude ionosphere. Substituting equation (3.17) in (3.15), the zonal current density can be written as,

$$\begin{aligned} J_\phi &= \sigma_P \left(1 + \frac{\sigma_H}{\sigma_P} \frac{\int_q \sigma_H \frac{h_\phi h_q}{h_p} dq}{\int_q \sigma_p \frac{h_\phi h_q}{h_p} dq}\right) E_\phi + \sigma_H B \left(u - \frac{\int_q \sigma_P u \frac{h_\phi h_q}{h_p} dq}{\int_q \sigma_p \frac{h_\phi h_q}{h_p} dq}\right) \\ &- \sigma_P B \left(v + \frac{\sigma_H}{\sigma_P} \frac{\int_q \sigma_H v \frac{h_\phi h_q}{h_p} dq}{\int_q \sigma_p \frac{h_\phi h_q}{h_p} dq}\right) + \frac{\sigma_H \frac{dI_p}{d\phi}}{h_p \int_q \sigma_p \frac{h_\phi h_q}{h_p} dq} \end{aligned} \tag{3.18}$$

Where the geomagnetic field, B, is assumed to be constant along the line of integration which is magnetic field lines in this case.

The first term in (3.18) is the sum of the zonal Pedersen current driven by the background electric field and a Hall current driven by the vertical polarization field (which is in turn caused by the zonal electric field and the polarized nature of the conductivity boundary). Since the Hall-to-Pedersen conductivity ratio is much larger than unity in the electrojet region, the contribution to the zonal current of the second term inside the big bracket is larger than that of the first term. The zonal current is amplified by the Cowling factor, the coefficient of $\sigma_P E_\phi$ in (3.18). The flux tube integrated conductivity gets smaller outside the E region; consequently, the strength of the zonal current diminishes.

The role of the zonal wind dynamo in driving zonal current can be seen from the second term in (3.18). The behavior of the zonal winds along magnetic field lines determines the value of Pedersen conductivity weighed average of the wind [*Richmond*, 1973a, 1995; *Hysell et al*, 2002]. If the zonal winds are invariant with altitude in the flux tube, the contribution to the integral will be zero. In this case, winds might not drive zonal current. It seems that the vertical polarization field

generated by winds tends to counteract wind driven current.

In cases where winds vary with altitude, *Richmond* [1973a, 1995], and *Hysell et al* [2002] argued that (i) little wind driven current flows at the top of magnetic field lines, but (ii) significant amount of wind driven current flows outside the zero dip angle region. A few degrees off the equator, dynamo fields are available for generating currents. If the different phases of the neutral wind oscillations are intercepted by the geomagnetic field lines in the flux tube, polarization fields generated within the different phases of the wind may be shorted out by parallel currents. A likely place for this to happens is outside the dip equator. In such cases, the wind dynamo drives a current since the second term in (3.18) does not vanish. Only if the phase fronts of the wind oscillations remain stationary in the flux tube can dynamo field be generated to cancel wind driven current. This analysis assumes negligible variations of the geometric scale factors along magnetic field lines.

Low latitude magnetic field line integrated model results from *Reddy and Devasia* [1981] support the analyses presented above. They predicted that the effects of local winds on the dynamo and current are latitude dependent. At the magnetic equator, wind generated currents are relatively small (10% - 30%) compared to the current driven by the east-west electric field.

The third term in (3.18) is the contribution to the dynamo field driven by vertical winds. Knowledge of the magnitude and phase of vertical winds are scant in the equatorial ionosphere. In addition, theoretical analysis of the momentum and mass continuity equations of air motion indicate that vertical air motions are generally much smaller than horizontal motion and can be ignored under most circumstances.

The last term in (3.18) is the contribution of the net vertical current coming out of the equatorial E region. In this regard, *Hysell et al* [2002] have noted that the relative importance of a net vertical current is substantial in regions of the ionosphere where the denominator, the flux tube integrated Pedersen conductivity, is small. In addition, *Haerendel and Eccles* [1992] have shown that substantial vertical current flows out of the equatorial E region around the solar terminator due to divergence of the electrojet, as discussed earlier.

The integrated zonal current in the magnetic equatorial plane is obtained by integrating the second term of the zonal current density, (3.18), along magnetic field lines. Let the current driven by local winds exclusively be represented by $(J_\phi)_u$, where u stands for the zonal wind,

$$\int_q (J_\phi)_u h_q dq = \int_q h_q dq \sigma_H B \left(u - \frac{\int_q \sigma_P u \frac{h_\phi h_q}{h_p} dq}{\int_q \sigma_p \frac{h_\phi h_q}{h_p} dq} \right) \tag{3.19}$$

Equation (3.19) shows that neither an oscillating nor a constant wind field contributes to the zonal wind driven current. That means the two dimensional flux tube model supports the argument that wind dynamo generates negligible current near the apex point.

3.6 A three-dimensional electrostatic potential model

Below the electrojet where the equipotential approximation may not be fully satisfied, the use of flux tube integrated models may not accurately predict electric fields and currents. Hence the need for three dimensional ionospheric modeling without the equipotential constraint.

Hysell et al [2002] presented a three-dimensional electrostatic potential model in a spherical coordinate system. Their model does not assume equipotential

geomagnetic field lines.

Using the fact that ionospheric currents are divergence free and applying the electrostatic approximation in (3.1), a second order inhomogeneous partial differential equation is obtained,

$$\nabla \cdot \left(\hat{\mathbf{\Sigma}} \cdot \nabla \Phi \right) = \nabla \cdot \left(\hat{\mathbf{\Sigma}} \cdot (\mathbf{E}_\circ + \mathbf{U} \times \mathbf{B}) \right) \tag{3.20}$$

where $\hat{\mathbf{\Sigma}}$ the general ionospheric conductivity tensor defined by (3.2), and $\mathbf{E}_\circ$ is a background electric field.

Hysell et al [2002] solved the differential equation (3.20) for the electrostatic potential in a spherical coordinate system and modeled electric fields and currents of the low latitude *E* region. Forcing their model by the NCAR-TIME-GCM winds, *Hysell et al* [2002] found that: (i) winds seem to have little significance in driving zonal currents near the dip equator but can drive substantial current at higher dip latitudes, a result in agreement with flux tube integrated models, (ii) zonal winds drive a significant Pedersen current in the meridional direction since ions are marginally magnetized and electrons are magnetized, and (iii) meridional winds drive discernible meridional currents at higher dip latitudes in the lower *E* region where the amplitudes of the winds are greatest.

3.7 Modeling the equatorial electrojet current profile

Numerical modeling of the vertical profile of the electrojet current aimed at reproducing current density profiles measured by rocket experiments has been a challenge for several years as discussed earlier in this chapter. The various efforts including *Sugiura and Cain* [1966], *Untiedt* [1967], *Richmond* [1973a], *Forbes and Lindzen* [1976a], and *Forbes and Lindzen* [1976b]. The strength of the equatorial

electrojet and the location of the peak current density calculated by these models did not agree with the measured profiles. *Ronchi and Sudan* [1990], by incorporating anomalous effects expressed in terms of small scale turbulence strength in their model, have reproduced fairly accurately current profiles measured *in situ*. Following their work, we will include anomalous effects to constrain our three dimensional electrostatic potential model (Chapter 5).

3.8 Looking ahead

In light of the review presented in this chapter and the need for a better computational model for the low latitude ionosphere, this dissertation will introduce a comprehensive numerical model in magnetic dipole coordinate system. The physics based three dimensional electrostatic potential model is based on realistic ionospheric conductivities, electric fields, winds, and incorporate anamalous collision effects. The model includes pressure gradient and gravity driven currents in addition to (3.1). Model calculations will invoke bistatic radar density measurements, wind profiles inferred from oblique radar Doppler measurements, and electric field derived from 150 km echo drifts. Model results are constrained by magnetometer measurements. The model solves for the vector electric field, current density, and zonal wind profiles in the low latitude E region. In the subsequent chapters, we will present how electron density and wind profiles are inferred from coherent scatter radar measurements at Jicamarca.

Chapter 4

E region electron densities derived from a bistatic radar experiment at Jicamarca

4.1 Introduction

This chapter presents electron density profiles in the equatorial E region ionosphere inferred from a bistatic coherent scatter radar experiment at the Jicamarca Radio Observatory in Perú. The necessity of developing this radar technique arises because of the fact that conventional incoherent scatter radar measurements for extracting plasma parameters are not applicable in the equatorial E region due to the permanent presence of nonthermal fluctuations [*Hysell and Chau*, 2001; *Shume et al*, 2005a]. The nonthermal plasma density fluctuations are caused by the equatorial electrojet current, a subject which was discussed at length in Chapter 2. The bistatic coherent scatter radar technique utilizes the plasma irregularities themselves as a diagnostic medium to scatter electromagnetic waves. The quasi-longitudinal approximation of electromagnetic wave propagation in a cold plasma is applied on the bistatic radar measurements to estimate electron density profiles. Inference of the E region electron density profiles is based on analysis of the phase (Faraday) angle of the coherently scattered signal. In this chapter, we present the sequence of steps leading to electron density estimation: (i) the quasi-longitudinal approximation of electromagnetic wave propagation in a cold magnetized plasma, (ii) the bistatic coherent scatter radar geometery, experimental parameters, the electron density inference technique, and experimental uncertainties, (iii) comparison of the inferred density with other estimates and the procedure employed to

validate the radar density profiles, and (iv) plasma irregulaities causing coherent radar scattering and thereby making measurements possible.

4.2 Wave propagation in a cold magnetoplasma

The Earth's ionosphere is an example of a magnetoionic medium. A magnetoionic medium refers to a plasma medium in an externally applied magnetostatic field [*Ratcliffe*, 1959; *Bittencourt*, 2003]. Magnetoionic theory deals with propagation of waves in a cold magnetoionic medium. A plasma can be regarded as cold if the thermal velocity of plasma particles is small compared to the propagation speed of the waves we are seeking. The cold plasma approximation works well for purposes of ionospheric radar probing. Analysis of radio signals scattered from the ionosphere has been crucial for plasma diagnostic purposes at the Jicamarca Radio Observatory [*Farley*, 1969; *Pingree*, 1990].

4.2.1 The Appelton-Hartree equation

The Appelton-Hartree equation comprises the dispersion relation for wave propagation in a cold magnetoplasma. The Appelton-Hartree equation is derived from the momentum and current density equations together with Maxwell's equations where ions are considered to be stationary. The following assumptions are made in deriving the Appelton-Hartree equation: (i) the wave frequency is assumed to be much larger than the ion gyro frequency, (ii) pressure gradient forces are ignored in the momentum equation since thermal motion is negligible compared to the phase velocity of the waves, (iii) the standard linear perturbation theory is employed, with the amplitude of the perturbed quantities assumed to be small compared to the background plasma parameters, and (iv) the various perturbed quantities are

assumed to have a plane wave solution. The Appelton-Hartree equation is then given by,

$$\eta^2 = \left(\frac{kc}{\omega}\right)^2 = 1 - \frac{X}{1 - iZ - \left(\frac{Y_T^2}{2(1-X-iZ)}\right) \pm \sqrt{\left(\frac{Y_T^4}{4(1-X-iZ)^2} + Y_L^2\right)}} \tag{4.1}$$

where η is an index of refractive of the medium, c is the speed of light, ω is a wave frequency, k is a wavenumber, and,

$$\begin{aligned} X &= \tfrac{\omega_{pe}^2}{\omega^2} \\ Y &= \tfrac{\Omega_e}{\omega} \\ Z &= \tfrac{\nu_e}{\omega} \\ Y_L &= Y\cos\gamma \\ Y_T &= Y\sin\gamma \end{aligned} \tag{4.2}$$

where $\omega_{pe} = \left(\frac{ne^2}{\epsilon_o m_e}\right)^{\frac{1}{2}}$ is the electron plasma frequency and γ is the angle of wave propagation relative to the geomagnetic field [*Budden*, 1961].

The dispersion relation, (4.1), provides two principal modes of wave propagation in a cold magnetized plasma, namely, the ordinary (O) mode (the positive solution), and the extraordinary (X) mode (the negative solution), for each wave frequency ω. The birefringence property giving rise to the above two modes of propagations is introduced by the geomagnetic field. Due to the difference in the indices of refraction of the O and X modes, the plane of polarization gets rotated while propagating, giving rise to the so called Faraday rotation phenomena. The angle of rotation or Faraday angle can be utilized to infer electron density profiles in the ionosphere.

4.2.2 The quasi-longitudinal approximation

In the quasi-longitudinal approximation, the direction of wave propagation is assumed to be roughly parallel to the geomagnetic field. For high frequency electromagnetic waves, $Z \ll 1$, electron collision frequencies are negligible compared to the wave frequency, and the Appelton-Hartree equation, (4.1), can be written as,

$$\eta_{\pm} = \left(1 - \frac{X}{1 \pm Y}\right)^{\frac{1}{2}} \tag{4.3}$$

For propagation in the direction of the geomagnetic field, $\mathbf{k} \cdot \mathbf{B} > 0$, the O mode corresponds to a Left Circularly Polarized (LCP) wave, and the X mode corresponds to a Right Circularly Polarized (RCP) wave. In this case, the wave electric field of the RCP wave rotates in the same sense as the electrons, whereas the electric field of the LCP wave and the ions have the same sense of rotation. The identification of the modes is reversed for anti-parallel wave propagation, $\mathbf{k} \cdot \mathbf{B} < 0$.

The quasi-longitudinal approximation, in other words, implies that the first term in the radical sign in the Appelton-Hartree equation (4.1) is negligible compared to the second term, that is,

$$\frac{Y_T^4}{4(1-X)^2} \ll Y_L^2 \tag{4.4}$$

Using the Jicamarca Radio Observatory transmission frequency, $\omega = \pi \times 10^8$ Hz, $\Omega_e = 2\pi \times 10^6$ Hz, and $\omega_{pe} = 2\pi \times 10^8$ Hz, the angle γ should be less than about 86° for the inequality in (4.4) to be satisfied. For the newly installed bistatic coherent scatter radar system between Jicamarca and Paracas in Perú, the wave propagates well off the perpendicular direction (see the geometry of the bistatic experiment in Figure 4.1), and the quasi-longitudial approximation is very well satisfied.

Using the above approximations, (4.1) can be written as,

$$\eta_{\pm} = \left(1 - \frac{X}{1 \pm Y\cos\gamma}\right)^{\frac{1}{2}} \tag{4.5}$$

Equation (4.5) is a generalization of (4.1) for an angle of propagation γ, satisfying the quasi-longitudinal approximation. The wave sees a gyrating electron with a frequency given by $\Omega_e \cos\gamma$.

For a wave frequency much larger than both the electron plasma and gyro frequencies, (4.5) can be written as,

$$\eta_{\pm} \simeq 1 - \frac{\omega_{pe}^2}{2\omega^2}\left(1 \mp \frac{\Omega_e\cos\gamma}{\omega}\right) \tag{4.6}$$

The refractive index of the two modes of propagation is a function of electron density, frequency, and the geomagnetic field. The phase difference between the two modes is an indication of the electron density of the medium.

4.2.3 Faraday rotation

Let us consider a linear polarized wave propagating along the z-axis. The electric field of the wave at the origin of a Cartesian coordinate system (x, y, z), can be written as,

$$\mathbf{E}(z=0,t) = E_\circ e^{-i\omega t}\hat{\mathbf{x}} = \frac{1}{2}E_\circ(\hat{\mathbf{x}} + i\hat{\mathbf{y}})e^{-i\omega t} + \frac{1}{2}E_\circ(\hat{\mathbf{x}} - i\hat{\mathbf{y}})e^{-i\omega t} \tag{4.7}$$

where the z axis is aligned with the direction of the geomagnetic field.

In writing the above expression, we have used the fact that a linearly polarized wave can be decomposed into right and left circularly polarized waves. The first term in (4.7) represents the RCP component of the wave, and the second represents the LCP part.

As shown by (4.5) and (4.6), the indices of refraction and hence the phase velocities of the LCP and RCP waves are different and hence propagate differently. Consequently, for $z > 0$, the electric field of the wave will take the following form,

$$\begin{aligned} \mathbf{E}(z,t) &= \frac{1}{2}E_\circ(\hat{\mathbf{x}} + i\hat{\mathbf{y}})\exp\left[i(\frac{\omega}{c}\eta_+ z - \omega t)\right] \\ &+ \frac{1}{2}E_\circ(\hat{\mathbf{x}} - i\hat{\mathbf{y}})\exp\left[i(\frac{\omega}{c}\eta_- z - \omega t)\right] \end{aligned} \tag{4.8}$$

Rearranging (4.8), we get,

$$\begin{aligned} \mathbf{E}(z,t) &= E_\circ \exp\left[i(\frac{\omega}{2c}(\eta_+ + \eta_-)z - \omega t)\right]\cos\left[\frac{\omega}{2c}(\eta_+ - \eta_-)z\right]\hat{\mathbf{x}} \\ &- E_\circ \exp\left[i(\frac{\omega}{2c}(\eta_+ + \eta_-)z - \omega t)\right]\sin\left[\frac{\omega}{2c}(\eta_+ - \eta_-)z\right]\hat{\mathbf{y}} \end{aligned} \tag{4.9}$$

We started with a linearly polarized wave (4.7). After the wave propagates a distance z along geomagnetic field lines, the resulting wave remains a linearly polarized (4.9) with a plane of polarization rotated by an angle δ, given by,

$$\delta = \frac{\omega}{2c}(\eta_+ - \eta_-)z. \tag{4.10}$$

This angle is related to the phase difference, $\frac{\omega}{c}(\eta_+ - \eta_-)z$, between the two modes of propagation (LCP and RCP). It is called the Faraday angle.

The differential Faraday angle, defined by $d\Theta$, corresponding to a wave travelling a differential length element dz in the E region can be written as,

$$\frac{d\Theta}{dz} = \frac{\omega}{c}(\eta_+ - \eta_-) \tag{4.11}$$

Writing the refractive indices in terms of the parameters in (4.6), the differential Faraday angle per differential path length can be described as,

$$\frac{d\Theta}{dz} = \left(\frac{e^3}{m_e^2}\right)\left(\frac{\mu_\circ}{\epsilon_\circ}\right)^{\frac{1}{2}}\left(\frac{1}{\omega^2}\right)n_e B\cos\gamma \tag{4.12}$$

Equation (4.12) relates the rate of change of Faraday angle with electron density, n_e. Phase angle profiles are normally measured from radar cross spectral measurements of the two modes of propagation. Geomagnetic field information can be obtained from International Geomagnetic Reference Field (IGRF) model, and the electron density of the medium can therefore be estimated using equation (4.12).

4.3 The bistatic radar experiment: theoretical aspects

In Chapter 2, we discussed how the equatorial electrojet current causes the E region to be unstable, producing a broadband spectrum of field-aligned plasma irregularities. The fact that the electrojet medium is governed by nonthermal physics makes the application of incoherent scatter radar techniques for extracting ionospheric plasma parameters impossible. However, the nonthermal fluctuations furnish a medium for coherent scatter radar diagnostics. *Hysell and Chau* [2001] designed a bistatic coherent scatter radar system that exploits the strong radar echoes from electrojet irregularities to infer E region electron density profiles from the Faraday rotation of the scattered signal.

4.3.1 The bistatic radar geometry

The transmitter for the bistatic radar system is located at Jicamarca (JRO), and the receiver is located about 2° south in Paracas, Peru. A schematic representation of the transmitter, receiver, and the geometry of the bistatic radar experiment is depicted in Figure 4.1. The transmitter and receiver coordinates along with the radar operating parameters are shown in Table 4.1. In Figure 4.1, ϕ_j is the angle of elevation, γ_j is the angle between the wave and the geomagnetic field, and ξ_j is

an angle between the incident and scattered wave vectors. The geomagnetic field vector is not necessarily in the plane of the diagram. These parameters depend on the location of the scatterers.

The bistatic coherent scatter radar experiment has the following practical aspects: (i) Although the free wave vectors are not orthogonal to the geomagnetic field, the Bragg scattering vector is perpendicular to the geomagnetic field such that coherent radar echoes from field aligned electrojet irregularities can be detected; (ii) The wave undergoes a considerable amount of Faraday rotation while traversing the E region ionosphere [*Hysell and Chau*, 2001].

According to Bragg's condition for constructive interference, the scattering wavelength can be written as,

$$\lambda = \frac{\lambda_\circ}{2}\left(\sin\frac{\xi_j(h)}{2}\right)^{-1} \tag{4.13}$$

where $\lambda_\circ$ is the wavelength of the transmitted wave and h is the altitude of the scatterers.

However, unlike backscattering radar experiments where $\xi_j = 180^\circ$ and $\lambda = \frac{\lambda_\circ}{2}$, in a bistatic radar geometry, Bragg's condition for constructive interference permits more than one spatial (Fourier) scattering component; the magnitude of the scattering vector depends on the scatterer altitude, (4.13). The spatial length of the scatterers is unique to each radar range gate.

4.3.2 Wave polarization

A horizontal (linearly) polarized wave is transmitted from Jicamarca. The wave polarization is directed along $\mathbf{x}$ (Figure 4.2) during transmission. The electric field

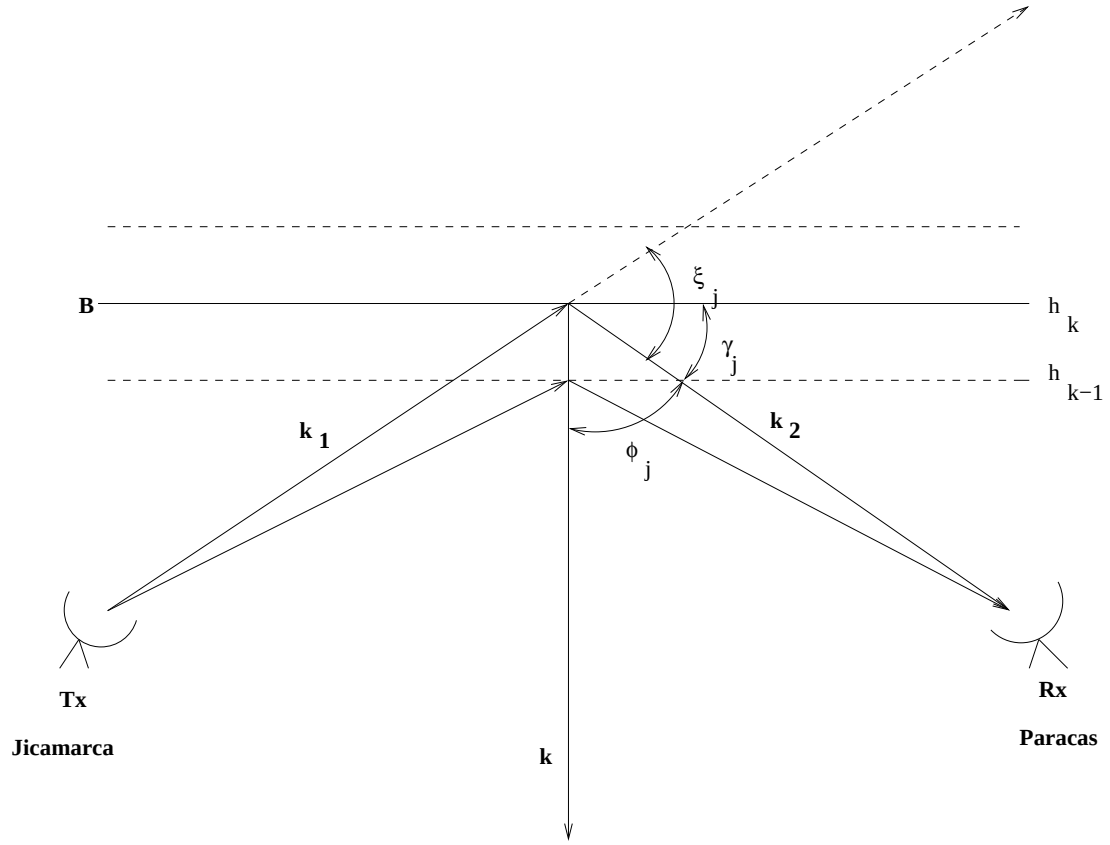

Figure 4.1: Schematic representation of the bistatic radar geometry. The transmitter is located at Jicamarca and the receiver is located at Paracas. $\mathbf{k}$, $\mathbf{k_1}$, and $\mathbf{k_2}$ are the scattering wave vector, the incident and scattered wave vectors, respectively. ϕ_j is angle of elevation, γ_j is the angle the scattered wave makes with the magnetic field, and ξ_j is the angle between $\mathbf{k_1}$ and $\mathbf{k_2}$.

of the wave can be expressed as,

$$\mathbf{E}(\mathbf{r}, t) = \hat{\mathbf{x}} E_\circ e^{i(\mathbf{k}\cdot\mathbf{r} - \omega t)} \tag{4.14}$$

While propagating through the E region plasma, the electric field rotates in the **x-y** plane (Figure 4.2), and the waves polarization is still linear or a combination

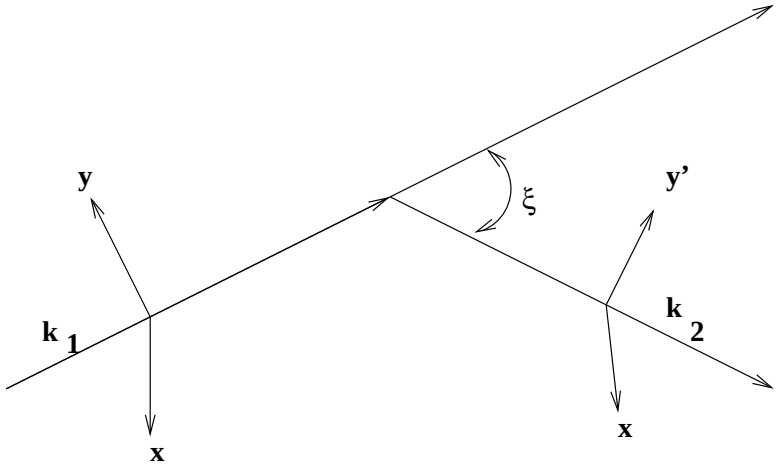

Figure 4.2: A schematic diagram showing the vectorial relationship between the wave propagation and polarization directions during transmission and reception in the bistatic radar experiment. At transmission, the electric field of the linearly polarized wave is along **x**.

of LCP and RCP waves. The electric field of the LCP and RCP components of the wave can be written as,

$$\mathbf{E}'_{\pm}(\mathbf{r},t) = (\hat{\mathbf{x}} \pm i\hat{\mathbf{y}})E'_{\circ}e^{i(\frac{\omega}{c}\eta_{\pm}\hat{\mathbf{k}}_{\mathbf{1}}\cdot\mathbf{r}-\omega t)} \tag{4.15}$$

where $\hat{\mathbf{k}}_{\mathbf{1}} = \frac{\mathbf{k_1}}{|\mathbf{k_1}|}$.

Suppose the wave polarization makes an angle δ with the **x** direction on its way to E region before scattered by electrons,

$$\delta = \frac{\omega}{2c}\left(\eta_{+} - \eta_{-}\right)\hat{\mathbf{k}}_{\mathbf{1}} \cdot \mathbf{r} = \frac{\Theta}{2} \tag{4.16}$$

where the angle Θ can be defined in terms of the phase difference between the LCP and RCP waves.

This result was obtained in the previous section for a general case of rotation

of plane of polarization of a linearly polarized wave, equation (4.10). The phase angle, Θ, is the Faraday angle accumulated by the wave before scattering.

Using property of electric field scattered by E region electrons, the electric field of the wave immediately after scattering becomes,

$$\mathbf{E}_{\pm}^{''}(\mathbf{r},t) = (\hat{\mathbf{x}} \pm i\cos\xi\hat{\mathbf{y}}^{'})E_{\circ}^{''}e^{i(\frac{\omega}{c}\eta_{\pm}\hat{\mathbf{k_2}}\cdot\mathbf{r}-\omega t)}$$

$$\begin{aligned}\mathbf{E}_{\pm}^{''}(\mathbf{r},t) &\propto E_{\circ}^{''}e^{i(\frac{\omega}{2c}[\eta_{+}+\eta_{-}]\hat{\mathbf{k_2}}\cdot\mathbf{r}-\omega t)}\hat{\mathbf{x}}\cos(\frac{\omega}{2c}[\eta_{+}-\eta_{-}]\hat{\mathbf{k_2}}\cdot\mathbf{r}) \\ &- E_{\circ}^{''}e^{i(\frac{\omega}{2c}[\eta_{+}+\eta_{-}]\hat{\mathbf{k_2}}\cdot\mathbf{r}-\omega t)}\cos\xi\hat{\mathbf{y}}^{'}\sin(\frac{\omega}{2c}[\eta_{+}-\eta_{-}]\hat{\mathbf{k_2}}\cdot\mathbf{r}) \qquad (4.17)\end{aligned}$$

where $\hat{\mathbf{k_2}} = \frac{\mathbf{k_2}}{|\mathbf{k_2}|}$.

Suppose the wave polarization makes an angle $\delta^{'}$ with $\mathbf{x}$ axis right after scattering. This angle can be written in terms of a ratio of the $\hat{\mathbf{y}}^{'}$ and $\hat{\mathbf{x}}$ components of the electric field in (4.17),

$$\delta^{'} = \tan^{-1}\left(\cos\xi\frac{\sin\frac{\omega}{2c}(\eta_{+}-\eta_{-})\,\hat{\mathbf{k_2}}\cdot\mathbf{r}}{\cos\frac{\omega}{2c}(\eta_{+}-\eta_{-})\,\hat{\mathbf{k_2}}\cdot\mathbf{r}}\right) \qquad (4.18)$$

After scattering, the circularly polarized waves propagate to the receiver and the plane of polarization continues to rotate in the $\mathbf{x}$-$\mathbf{y}^{'}$ plane. Let $\Theta^{'}$ be the Faraday angle accumulated during this time.

In the bistatic radar geometry, $\mathbf{k}\cdot\mathbf{B} > \mathbf{0}$, before and after scattering, unlike monostatic radar experiments. In monostatic radar experiments, $\mathbf{k}\cdot\mathbf{B} < \mathbf{0}$, after scattering, which results in switching of the LCP wave to RCP and vise versa. The reason for this switch is the change in orientation of the rotation of wave polarization with respect to the gyrating charged particles. In a bistatic radar experiment, however, the polarization switch does not happen, the LCP wave will continue as an LCP wave, and the same is true for the RCP wave. Consequently,

the magnitude of the Faraday angle continue to increase without undergoing a change in sign.

Therefore, the total Faraday angle, Θ^t, accumulated by the wave while traversing the E region ionosphere is given by the sum of Faraday angles gathered by the wave, $\Theta^t = \delta^{'} + \Theta^{'}$.

The total Faraday angle is the parameter which can be measured from the bistatic radar experiment. The total Faraday angle for a ray, j, is given by the formula,

$$\Theta_j^t = 2\tan^{-1}\left(\cos\xi_j \tan\frac{\Theta_j}{2}\right) + \Theta_j^{'} \tag{4.19}$$

4.3.3 Electron density inference formulation

The quasi-longitudinal theory of electromagnetic wave propagation in a cold magnetoplasma is the foundation for estimating electron density in the bistatic radar experiment. The theory relates the Faraday angle to the electron density of the medium quantitatively, as shown by the relationship (4.12).

Using the geometry of Figure 4.1, the differential Faraday angle for the signal propagating along a ray j downward through differential altitude element dh_k can be written as,

$$d\Theta_{jk} = an_k B(k)\cos\gamma_j \sec\phi_j dh_k \tag{4.20}$$

where the constant $a = \left(\frac{e^3}{m_e^2}\right)\left(\frac{\mu_\circ}{\epsilon_\circ}\right)^{\frac{1}{2}}\left(\frac{1}{\omega^2}\right)$ and the differential range gate element $dz_k = dh_k \sec\phi_j$. The geomagnetic field, B, is derived from IGRF model [*National Space Science Data Center*, 2002].

The total Faraday rotation incurred along the ray propagating downward from the altitude h_j where scattering took place is then given by [*Hysell and Chau*,

2001],

$$\frac{\Theta_j - C}{\cos\gamma_j \sec\phi_j} \propto \sum_{k=1}^{j} n_k \Delta h_k \tag{4.21}$$

where C is introduced to account for the phase which might be introduced due to asymmetries in the receiver system.

If the receiver system is constructed such that C is negligible, the plasma density at the altitude h_j can be calculated from the difference in the quantity in (4.21) between successive altitudes,

$$n_j \Delta h_j \propto \frac{\cos\phi_j}{\cos\gamma_j}\Theta_j - \frac{\cos\phi_{j-1}}{\cos\gamma_{j-1}}\Theta_{j-1} \tag{4.22}$$

Using the fact that the right hand side of equation (4.22) is a backward finite difference, it can be written in terms of a derivative of the function in the bracket in (4.24),

$$n(h)dh \propto d\left(\frac{\cos\phi(h)}{\cos\gamma(h)}\Theta(h)\right) = d(f(h)) \tag{4.23}$$

It follow from (4.23) that,

$$n(h) \propto \frac{df(h)}{dh} \tag{4.24}$$

where,

$$f(h) = \frac{\cos\phi(h)}{\cos\gamma(h)}\Theta(h) \tag{4.25}$$

Equation (4.24) is the recipe for inferring electron density profiles. In order to construct vertical profile of electron density, $n(h)$, the phase angle $\Theta(h)$ is required input. This is actually $\Theta_j^{'}$ using the terminology of (4.19). The parameters ϕ_j, ξ_j and γ_j are calculated by taking the Earth's curvature into consideration and using, the radar geometry (Figure 4.1), the transmitter and receiver coordinates,

and the range of the scatterers measured by the radar. The total Faraday rotation Θ_j^t is measured by the bistatic radar. Our density estimating algorithm calculates $\Theta_j^{'}$ iteratively from (4.19) and uses it in (4.24).

4.4 Bistatic radar observation

A bistatic coherent scatter radar experiment was first conducted at the Jicamarca Radio Observatory in September of 2000 [*Hysell and Chau*, 2001]. The validity of the quasi-longitudinal approximation applied to inferring E region electron densities was tested in the 2000 radar experiment. In that trial radar experiment, the transmitter and receiver were located at Paracas and Jicamarca, respectively.

At the beginning of the year 2004, a new and improved bistatic radar system was installed, and the locations of the transmitter and receiver were switched to Jicamarca and Paracas, respectively. Since March of that year, a series of bistatic radar experiments has been conducted utilizing the newly installed radar system. Representative daytime E region electron density profiles from March 23, 2004 are presented here.

4.4.1 The bistatic radar experiment description: improved experiment

The transmitter and receiver of the bistatic radar system are separated by about 222 km (or 2° of latitude). Coordinates of the transmitter and receiver and a summary of the radar operating parameter for both the new and original radar systems are shown in Table 4.1.

The new radar system was mainly introduced in order to enhance the sensitivity.

Table 4.1: The current (beginning 2004) and original (2000) bistatic radar operating modes

Parameters	Current (2004) experiments	Original (2000) experiments
Frequency, MHz	49.92	49.92
Peak power, kW	60	20
IPP[a], μs	2500	250
Coherent integration	16	8
Pulse width, μs	4x13 BC[b]	3
Range resolution, m	600	450
Altitude resolution, m	840 - 900	630 - 680
Range gates	92	40
HPFBW[c]	4°	6°
Transmitter coordinates	11°57'S	13°51'S
	76°52.6'W	76°14.96'W
Receiver coordinates	13°51'S	11°57'S
	76°14.96'W	76°52.6'W
Antenna	Sixteen five element yagi	Four five element yagi
	0.7λ[d] spacing	1.5λ spacing

a Inter Pulse Period

b Barker Code pulse

c Half Power Beam Width

d Wave length of the transmitted beam

Accordingly, the following remedies were done: (i) the transmitter and receiver of the original bistatic system were swapped in order to be able to utilize two 30kW transmitters available at Jicamarca, thus increasing the peak power by a factor of 3, (ii) sixteen 5 element yagi arrays with 0.7λ spacing were used (compared to four 5 element yagi arrays with 1.5λ spacing of the bistatic radar experiment of the year 2000) for a transmitting and receiving antennas. The objective of enlarging the arrays were to suppress grating sidelobes and, at the same time, enhance the signal strength at the receiver, and (iii) Barker coded pulses were introduced. The system upgrades provide close to 20 dB improvement in sensitivity. Moreover, in order to tackle the problems associated with azimuth scatter the half power beamwidth was decreased by 2° compared to the original experiment.

4.4.2 Electron density estimation

The power profiles for the two modes of propagation are shown in panel I and II of Figure 4.3. The estimated electron density profile (panel V) falls in the same altitude region, suggesting a relationship between the returned power and electron density of the medium.

Let V_L and V_R be the complex voltages at the receiving channels of the left and right circularly polarized signals, respectively. They can be written as,

$$\begin{aligned} V_L &= V_L^r + iV_L^i = V_\circ e^{i\theta_L} \\ V_R &= V_R^r + iV_R^i = V_\circ e^{i\theta_R} \\ V_L V_R^* &= V_\circ^2 e^{i(\theta_L - \theta_R)} \end{aligned} \tag{4.26}$$

where $V_\circ$ is a voltage amplitude, and the phase angles θ_L and θ_R correspond to the left and right circularly polarized signal, respectively.

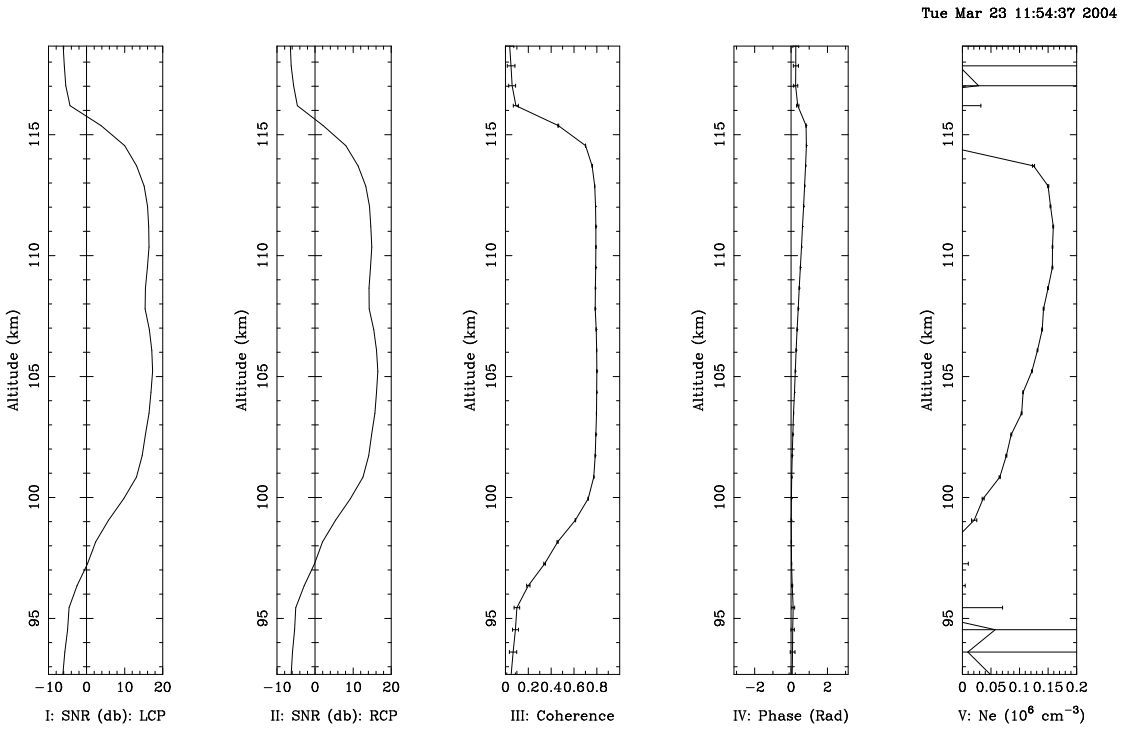

Figure 4.3: Parameters measured by the bistatic radar system. Panel I: Power profile of the left circularly polarized signal; Panel II: Power profile of the right circularly polarized signal; Panel III: Cross-spectral coherence profile; Panel IV: Faraday rotation angle profile; V: N_e in units of 10^6cm^{-3}.

From (4.26), the real and imaginary parts of the crossed power can be written as,

$$\Re(V_L V_R^*) = V_\circ^2 \cos(\theta_L - \theta_R) \tag{4.27}$$

$$\Im(V_L V_R^*) = V_\circ^2 \sin(\theta_L - \theta_R) \tag{4.28}$$

The ratio of the imaginary to the real parts of the crossed power gives rise to the phase difference between the left and right circularly mode of propagations.

The Faraday angle θ, is defined as,

$$\theta = \theta_L - \theta_R = \tan^{-1} \frac{\Re[V_L V_R^*]}{\Im[V_L V_R^*]} \tag{4.29}$$

Coherence and phase angle are described in terms of averages of power and cross correlated powers over N samples,

$$\langle V_L V_R^* \rangle = \frac{1}{N} \sum_{k=1}^{N} \left[V_{Lk}^i V_{Rk}^i + V_{Lk}^r V_{Rk}^r \right] + \frac{1}{N} i \sum_{k=1}^{N} \left[V_{Lk}^r V_{Rk}^i - V_{Lk}^i V_{Rk}^r \right]$$

$$V_L V_R^* = \rho_r + i\rho_i \tag{4.30}$$

where the real and imaginary parts of the cross correlation function are defined as,

$$\rho_r = \frac{1}{N} \sum_{k=1}^{N} \left[V_{Lk}^i V_{Rk}^i + V_{Lk}^r V_{Rk}^r \right]$$

$$\rho_i = \frac{1}{N} \sum_{k=1}^{N} \left[V_{Lk}^r V_{Rk}^i - V_{Lk}^i V_{Rk}^r \right] \tag{4.31}$$

The average power of the two circularly polarizations are defined as,

$$P_L = \frac{1}{N} \sum_{k=1}^{N} V_{Lk} V_{Lk}^* = \frac{1}{N} \sum_{k=1}^{N} [(V_{Lk}^r)^2 + (V_{Lk}^i)^2]$$

$$P_R = \frac{1}{N} \sum_{k=1}^{N} V_{Rk} V_{Rk}^* = \frac{1}{N} \sum_{k=1}^{N} [(V_{Rk}^r)^2 + (V_{Rk}^i)^2] \tag{4.32}$$

The magntiude of the cross correlation function or coherence is calculated by taking the modulus of the correlation function (4.30) normalized by product of the power of the two circular polarizations,

$$\rho = \sqrt{\frac{\rho_r^2 + \rho_i^2}{P_L P_R}} \tag{4.33}$$

The coherence displayed in panel III (Figure 4.3) is calculated using (4.33). It is shown in the panel that wherever the coherence is high, the errors in the density estimates are very low, showing that coherence values close to unity are desirable for accurate estimation of electron densities.

In the section dealing with error analysis, we will see the quantitative relation between variances in phase angle and the coherence estimates. Maximizing the coherence parameter means minimizing the errors of phase angle and hence electron density measurements.

The phase angle can be calculated from (4.30) using the prescription given in equation (4.29),

$$\theta = \tan^{-1} \frac{\rho_i}{\rho_r} \tag{4.34}$$

The phase angle, estimated using (4.34), together with (4.19) are employed to form the phase angle $\theta_j^{'}$, profile shown in panel IV, Figure 4.3.

The total Faraday angle profiles are then used to construct electron density profiles through backward finite differencing (4.24),

$$n(h_j) \propto \frac{f(h_j) - f(h_{j-1})}{h_j - h_{j-1}} \tag{4.35}$$

The estimated electron density profile (solid line) with error bars is depicted in Figure 4.3 (panel V). The bistatic coherent scatter radar experiment has enabled us to measure electron density profiles spanning about 14 km altitude in the electrojet region. Panel V of the same figure also shows that the density profile generally rises gently from the bottomside on its way to the peak. The measured E region peak density occurs at about 110 km altitude and has a value of about $\simeq 0.16 \times 10^6$ cm^{-3}. In the next section, we compare and contrast the radar measured profiles with other theoretical, experimental and model E region electron density measures.

Also shown in Figure 4.3 (panel V), the plasma density scale height has distinct values below and above the peak, having a relatively small magnitude below the peak compared to above the peak (and leading to the valley region). This feature

is shared by E region density profiles in the midlatitude [*Trost*, 1979] and high latitude [*Brekke and Hall*, 1988] ionospheres.

4.4.3 Error analysis

Assume that the fluctuations in the variables X and Y are uncorrelated. Let their variances be defined by, σ_X^2 and σ_Y^2, respectively. The variance, σ_G, of a function $G(X, Y)$ can be expressed as [*Bevington*, 1969],

$$\sigma_G^2 \simeq \sigma_X^2 \left(\frac{\partial G}{\partial X}\right)^2 + \sigma_Y^2 \left(\frac{\partial G}{\partial Y}\right)^2 \tag{4.36}$$

We will now calculate the variance of the phase angle, σ_θ^2, by applying the relation (4.36) and using (4.34), the expression for Faraday angle, $\theta(\rho_r, \rho_i)$. The variance of the phase angle then becomes,

$$\sigma_\theta^2 \simeq \sigma_{\rho_r}^2 \left(\frac{\partial \theta}{\partial \rho_r}\right)^2 + \sigma_{\rho_i}^2 \left(\frac{\partial \theta}{\partial \rho_i}\right)^2 \tag{4.37}$$

where $\sigma_{\rho_r}^2$ and $\sigma_{\rho_i}^2$ are the variances of the real and imaginary parts of the correlation function, respectively.

Performing the derivatives in (4.37),

$$\begin{aligned} \frac{\partial \theta}{\partial \rho_r} &= \frac{-\rho_i}{\rho_r^2 + \rho_i^2} \\ \frac{\partial \theta}{\partial \rho_i} &= \frac{\rho_r}{\rho_r^2 + \rho_i^2} \end{aligned} \tag{4.38}$$

Assuming further that the variances of the real and imaginary parts of the correlation function contribute equally to the total variance, that is, $\sigma_{\rho_r}^2 \simeq \sigma_{\rho_i}^2 \simeq \frac{1}{2}\sigma_\rho^2$, and defining coherence, $|\rho|^2 = \rho_r^2 + \rho_i^2$,

$$\sigma_\theta^2 \simeq \frac{1}{2} \frac{\sigma_\rho^2}{|\rho|^2} \tag{4.39}$$

The magnitude of signal coherence is therefore a crucial factor in determining the uncertainties in the measurement of the phase angle. The errors of phase angle estimation are minimized whenever the cross correlation between the two circular polarizations is high.

Coherence is adversely affected by dispersion, noise and interference [*Farley*, 1969; *Hysell and Chau*, 2001]. Generally, the phase angle, θ, varies within the scattering volume defined by antenna radiation pattern and pulse width. The contributions corresponding to different values of the phase angle will be uncorrelated, leading to a Faraday angle dispersion. However, phase angle dispersion does not threaten the accuracy of estimation here because of the low E region plasma densities involved and the narrow beam width of the the bistatic radar experiment. To the extent noise alone is responsible for decorrelation of the circularly polarized signals, $|\rho| = \frac{S}{S+N}$ and the variance of the correlation function becomes [*Hysell and Chau*, 2001],

$$\sigma_\rho^2 \approx \frac{1}{K}\left(\frac{N}{S} + \frac{3}{2}\frac{N^2}{S^2}\right) \tag{4.40}$$

where S and N are the strengths of signal and noise, respectively, and K is the number of statistically independent samples used to estimate the correlation function. Since correlation time is the echoes is of the order of 5 ms, $K = 10^4$ to 10^5 independent samples for the coherent scatter experiments [*Hysell and Chau*, 2001]. *Farley and Hagfors* [2004] have also noted that $K = 10^4$ smaples will be needed in order to estimate signal power to with in 1 percent of accuracy.

In order to calculate the standard deviations of electron density estimates, we have incorporated (4.39), (4.40), and the fact that uncertainties in the phase angle estimations propagate to the electron density estimates. The estimated error are shown with the profiles in panel V of Figure 4.3. With the exception of the

extreme top and bottom altitudes, the densities were measured with a high degree of accuracy; relative uncertainties were only 1.0% on average.

4.5 Measured density profiles compared with other electron density estimates

In the present section, equatorial E electron density estimates derived from the bistatic radar experiment are compared and contrasted with four electron density estimates: theoretical (electron density function derived from the α Chapman production function), experimental (rocket experiments carried out in Thumba, India) electron density measurements, International Reference Ionosphere (IRI-2001) model E region electron density predictions (these comparisons are shown in panels II - IV of Figure 4.4, respectively), and peak densities from the Jicamarca Digisonde Portable Sounder (DPS-4) (shown in Figure 4.5). The finding reported here are reproduced from a recent manuscript by *Shume et al* [2005a].

4.5.1 The Chapman function

Here we present a simple analytical method of modeling ionization profiles in the ionosphere. Given a neutral atmosphere and a theory for the rate of ion production, the Chapman theory provides ionization density profiles.

The rate of production of ionization (also called production function in the literature) is proportional to the rate at which ionization is absorbed by the neutral atmosphere constituents,

$$Q = -C\frac{dI}{ds} = C\sigma n_n I \tag{4.41}$$

where I intensity of ionizing solar radiation, σ is a radiation-absorption cross-

section, n_n is neutral atmosphere density of a single neutral atmosphere species and ds is a differential line of sight distance, $ds = dh \sec\chi$, χ is a solar zenith angle, dh is a differential altitude element, and C is an ionization efficiency which is assumed to be constant.

The neutral atmosphere density profile is derived from the hydrostatic equilibrium condition of an isothermal atmosphere,

$$n_n = n_{n\circ} \exp\left(-\frac{h - h_\circ}{H_n}\right) \tag{4.42}$$

where $n_{n\circ} = n_n(h_\circ)$, $H_n = \frac{\kappa_B T_n}{m_n g}$ is a density scale height, T_n and m_n are respectively temperature and mass of the neutral atmosphere constituent under consideration.

At the peak of production of ionization,

$$\frac{dQ}{ds} = C\sigma I n_n \left(\frac{1}{n_n}\frac{dn_n}{ds} + \frac{1}{I}\frac{dI}{ds}\right) = C\sigma I n_n \left(\frac{\cos\chi}{H_n} - \sigma n_n\right) = 0 \tag{4.43}$$

and therefore leads to the condition,

$$\sigma H_n n_{nm} \sec\chi = \sigma H_n n_{n\circ} \exp\left(-\frac{h_m - h_\circ}{H_n}\right) \sec\chi = 1 \tag{4.44}$$

where $n_{nm} = n_n(h_m)$ at production maximum h_m.

For an overhead sun (4.44) becomes,

$$\sigma H_n n_{n\circ} = \exp\left(\frac{h_{m\circ} - h_\circ}{H_n}\right) \tag{4.45}$$

where $h_{m\circ}$ is the maximum of production for an overhead sun.

The solution for the intensity of ionization is obtained by combining and solving (4.41) and (4.42) we get,

$$I(h) = I_\infty \exp\left(-\sigma \sec\chi H_n n_n\right) = I_\infty \exp\left(-\sigma \sec\chi H_n n_{n\circ} \exp(-\frac{h - h_\circ}{H_n})\right) \tag{4.46}$$

where $I_\infty = I(h \to \infty)$.

It follows from (4.44) and (4.46) that at ionization maximum,

$$I(h_m) = I_\infty \exp\left(-\sigma \sec\chi H_n n_{nm}\right) = I_\infty \exp(-1) \tag{4.47}$$

Combining (4.46) with (4.41), and using the relation,

$$Q_m = Q(h_m) = C\sigma n_{nm} I(h_m) = C\sigma n_{n\circ} \exp\left(-\frac{h_m - h_\circ}{H_n}\right) I_\infty \exp(-1) \tag{4.48}$$

the rate of ionization production becomes,

$$Q(h) = Q_m \exp\left(1 + \frac{h_m - h}{H_n} - \exp(\frac{h_m - h}{H_n})\right) \tag{4.49}$$

A combination of (4.44) and (4.45) gives,

$$\frac{h_m}{H_n} = \frac{h_{m\circ}}{H_n} + \log(\sec\chi) \tag{4.50}$$

Using (4.50) in (4.49), the rate of production can be written as,

$$Q(h) = Q_{m\circ} \exp\left(1 - \zeta - \sec\chi \exp(-\zeta)\right) \tag{4.51}$$

where $\zeta = \frac{h - h_{m\circ}}{H_n}$. From (4.44) and (4.48), $Q_m = \frac{C I_\infty \exp(-1)}{H_n \sec\chi}$, therefore, for an overhead sun $Q_{m\circ} = \frac{Q_m}{\cos\chi}$.

This result is known as the Chapman profile and was also derived by numerous researchers including [*Budden*, 1961; *Hargreaves*, 1995; *Luhmann*, 1995; *Schunk and Nagy*, 2000].

In a steady state and if plasma transport is neglected, the electron continuity equation is reduced to $Q_e = L_e = \alpha N_e^2$. An α function is employed in this case since the loss of ionization content is assumed to behave quadratically in the E region ionosphere which is mainly rich in molecular gases but also a small percentage of atomic constituents of the neutral atmospheric, Figure 2.3. The electron density profile then becomes,

$$N_e(h) = N_{mE} \exp\left(\frac{1}{2}(1 - \zeta - \sec\chi \exp(-\zeta))\right) \tag{4.52}$$

where $N_{mE} = \sqrt{\frac{Q_{m\circ}}{\alpha}}$ is E region density peak. The amplitude production function $Q_{m\circ}$ is a mean of the peak rates of production of the various constituents.

This is the plasma density function describing the vertical and zenith angle dependence of densities when the plasma is in photochemical equilibrium.

4.5.2 Electron density profile from the α Chapman function

The altitude variation of E region electron density can be represented by a simplified theoretical electron density function ($N_e(h)$) derived from the α Chapman function given by (4.52).

Figure 4.4 (panel II) shows a superposition of a Chapman electron density function $N_e(h)$ (solid line) and the measured densities (circles). The input parameters used to calculate $N_e(h)$, are, N_mE=0.161x10^6 cm^{-3}, h_mE=110.0 km, and χ=14.3^o at noon local time for March 23, 2004 as obtained from IRI-2001 model specifications [*National Space Science Data Center*, 2001], and a constant atmospheric scale height H=6.2 km as derived from the MSIS-E-90 Atmosphere Model [*National Space Science Data Center*, 1990]. Appreciable congruence is found between the bistatic radar observation and the theoretical density, $N_e(h)$.

4.5.3 Electron density from rocket measurements

A full solar cycle of equatorial daytime E region electron density data from Langmuir probes onboard rocket flight experiments in Thumba (in the Indian subcontinent) is represented in Figure 7 of Chandra etal. [2000]. Here in Figure 4.4 (panel III), we have reproduced an electron density profile (stars) from a rocket flight ex-

periment conducted in the spring of 1975 representing solar minimum conditions. The shape and magnitude of our measured density profile (circles) are comparable to the rocket probe data except around the very lowest altitudes where the radar measurement has significant uncertainty.

4.5.4 The IRI model: Lower *E* region

The IRI model uses the mathematical function shown below in (4.53) to connect the D region with the E region peak density located at peak altitude h_{mE}[*Bilitza*, 1990],

$$N(h) = N_{mE} \exp\left(-D_1 (h_{mE} - h)^K\right) \tag{4.53}$$

where K and D_1 are determined such that the exponential function agrees with the D region profile and its first derivative at the height $h_{DX} = 85.6$ km during the day and $h_{DX} = 92.5$ km at night. The parameters K and D_1 are defined as,

$$K = \frac{-D_N (h_{mE} - h_{DX})}{N_{DX} \log \frac{N_{DX}}{N_{mE}}} \tag{4.54}$$

$$D_1 = \frac{D_N}{N_{DX} K (h_{mE} - h_{DX})^{K-1}} \tag{4.55}$$

where N_{DX} is the electron density at h_{DX} and D_N is the derivative $\frac{dN}{dh}$ at that height.

4.5.5 Electron density from IRI-2001 ionospheric parameter specifications

We have also made a comparison of the IRI-2001 E region electron density predictions [*Bilitza*, 2001] with the radar derived densities. IRI-2001 results (solid line)

superimposed on the density measurements (circles) for March 23, 2004 at noon are shown in panel IV of Figure 4.4.

At and above the peak

Panel IV of Figure 4.4 clearly demonstrates that at and above the peak, the IRI-2001 and measured densities are coincident. The IRI peak density model is constructed utilizing a worldwide network of ionosonde f_oE (E region critical plasma frequency) measurements [*Bilitza et al*, 1993; *Bilitza*, 2001], hence the reason for the good agreement between the IRI and measured peak values. In addition, in both the IRI and measured density profiles, the peak density occurred at 110.0 km. In general, the radar measured density peak altitude varies between 108.0 km and 111.0 km (not shown here in Figure 4.4 but can be seen from Figure 4.6), the typical peak altitude being 110.0 km.

Below the peak

However, the two electron density estimates depart drastically below the peak. The IRI bottomside E region density profile is represented by an arbitrary exponential function, (4.53), connects the D region to the E region peak density [*Bilitza*, 1990]. Mathematically, there might be multiple ways of smoothly joining the D region and E region peaks. The discrepancy mentioned above can be attributed to the fact that IRI bottomside E region profile is an arbitrary mathematical function which does not have an observational basis. Evidently, the IRI model overestimates E region bottomside electron densities as shown in panel IV of Figure 4.4.

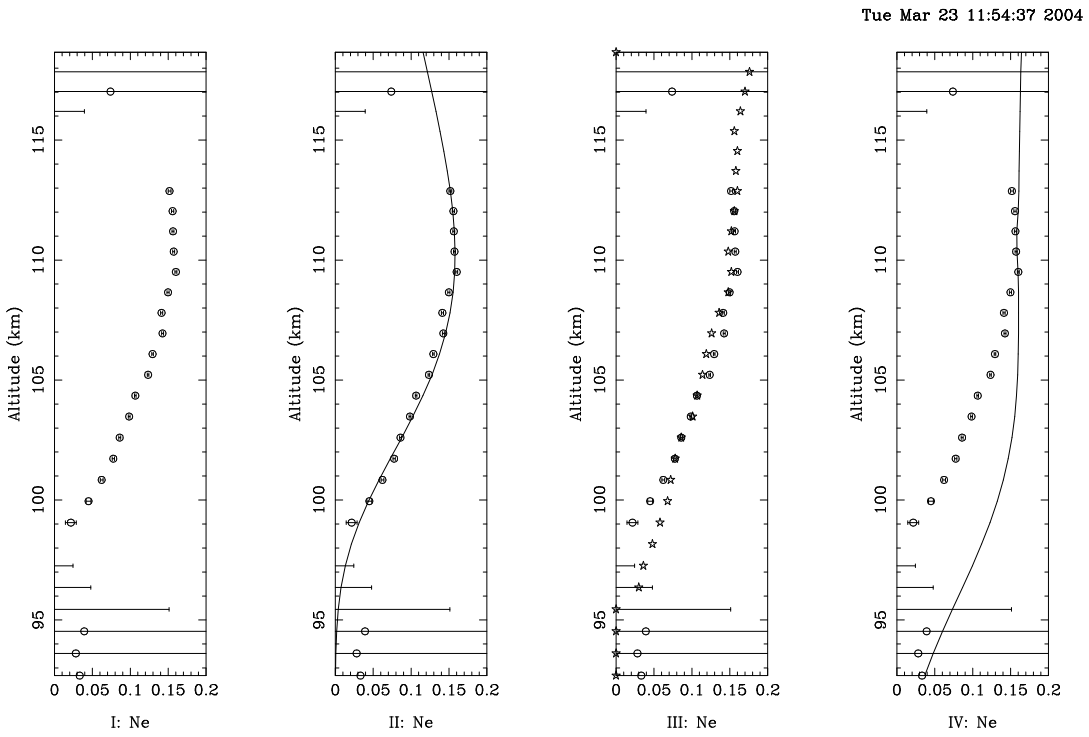

Figure 4.4: Panel I: measured electron density profile with error bars; Panel II: measured density (circles) superimposed on a Chapman electron density function (solid line); Panel III: measured density (circles) along with electron density from rocket experiments (stars); Panel IV: measured density (circles) superimposed on IRI-2001 (solid line); All times are local time; Ne (Electron density) in units of $10^6 \mathrm{cm}^{-3}$.

4.5.6 Peak density comparison

The Jicamarca Digisonde Portable Sounder (DPS-4) records f_oE at 15 minute intervals. At noon on March 23, 2004, f_oE=3.62 MHz, and the corresponding peak E region electron density was N_mE=0.162x10^6 cm^{-3}. The peak IRI electron density was (0.161x10^6 cm^{-3}). On the same day at local noon, the measured

peak density was (0.162±0.001)x10^6 cm^{-3}. Therefore, the peak electron density estimates are in fairly good agreement, their difference falling within the range of experimental uncertainty.

A time series comparing the peak densities is shown in Figure 4.5. The figure shows how the measured peak density (circles) compares with the Jicamarca Digisonde (X) and IRI-2001 (solid line) peak density estimates. The measured peak is consistent with the Digisonde and IRI peak values from about 10:00 to 14:30 local time. However, about two hours before and after local noon, two stream processes terminate in the electrojet, and because gradient drift processes are stable near and above the *E* region peak by definition, echoes from near and above the peak vanish (more on the coherent radar scattering mechanisms in the next section). It therefore important to note that, the bistatic radar density profiles are accurate but incomplete and are therefore unsuitable for tracking the altitude or density of the peak throughout the day.

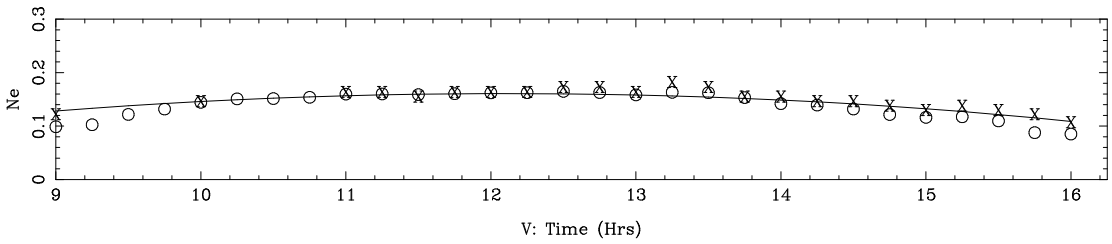

Figure 4.5: Temporal variation of peak density, radar (circles), the Jicamarca Digisonde (X), and IRI-2001 (solid line) on March 23, 2004; All times are local time; Ne (Electron density) in units of $10^6 cm^{-3}$.

In summary, *E* region electron densities inferred from the bistatic radar observation agrees satisfactorily with the theoretical and experimental electron density

estimates mentioned above. It is noteworthy, however, that below the altitude of the E region peak, the measured density profiles diverge significantly from the IRI-2001 profiles.

4.6 *E* region plasma irregularities causing coherent radar scattering

What are the short wavelength field aligned plasma irregularities responsible for the coherent radar echoes utilized for inferring E region electron density profiles?

The waterfall plot in Figure 4.6 shows the altitudinal variation of the radar measured electron density in the equatorial electrojet region as well as the temporal variation of the density profiles from 9:00 to 16:00 Local Time. Both the bottomside and topside coherent radar returns underlying the density profiles are due to short wavelength irregularities in the electrojet. *Kudeki et al* [1987] have suggested that pure two-stream instability processes provide the mechanism for the topside coherent scatter. Instabilities directly driven by the electrojet through the two-stream mechanism would account for the topside coherent radar echoes. Electron density estimation was possible due to the existence of those field aligned irregularities.

Electrons are increasingly collisional in the bottomside and as a result, the relative motion of electrons and ions might not fast enough to reach the ion acoustic speed threshold [*Kudeki et al*, 1987]. The two-stream mechanism might not therefore excite instabilities in the E region bottomside. In addition, for short wavelengths the gradient-drift instability mechanism is stable. The bottomside irregularities are therefore explained by a gradient drift wave driven mode cou-

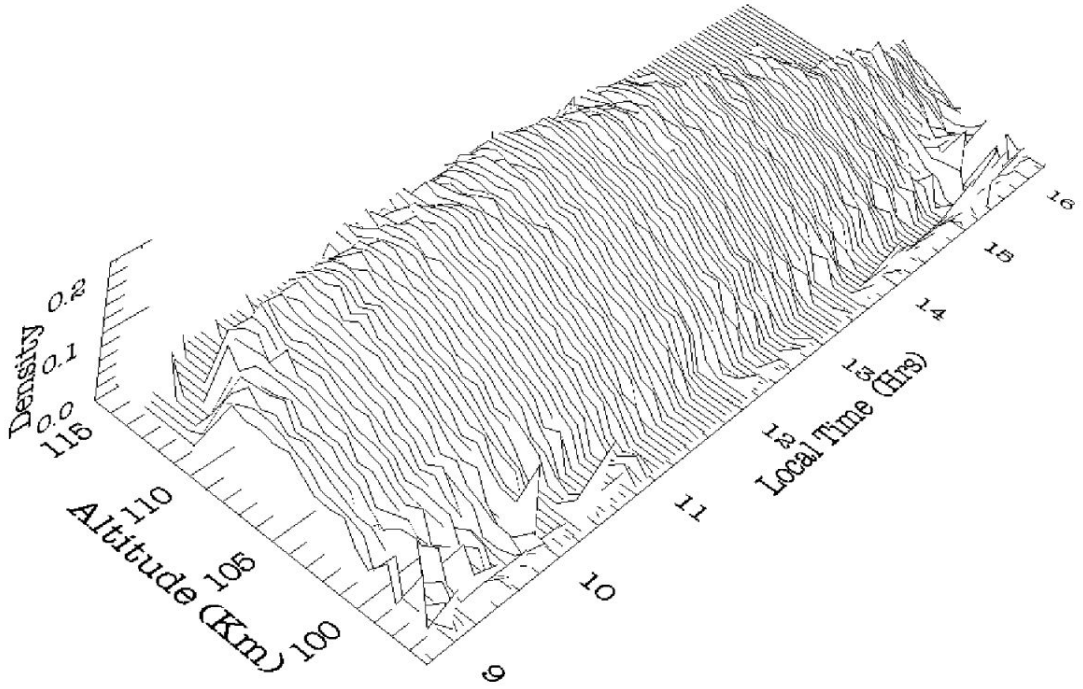

Figure 4.6: The waterfall plot depicts altitudinal and temporal variations of equatorial E region electron density (in units of $10^6 \mathrm{cm}^{-3}$) derived from short wavelength coherent scattering in the bistatic radar experiment between Jicamarca and Paracas, Peru on March 23, 2004.

pling mechanism [*Sudan and Keskinen*, 1979]. Around noon local time (two hours before and after noon) where the solar zenith angle is minimum, strongly driven pure two-stream waves are present, making topside density measurement possible. The positive density gradient in the bottomside allows gradient-drift irregularity processes to operate, permitting coherent scatter radar density measurements in the bottomside. However, before 9:45 and after 14:00 local times when the topside echoes subside and bottomside echoes get weaker, the density profiles contract in altitude as well as in shape.

It should be noted that electron density profiles are available only at altitudes and local times when strong plasma irregularities are present. The usefulness of the low power bistatic radar system is, therefore, restricted to certain local times of the day where the electrojet is strong enough to trigger instabilities. The radar technique might not be, for example, suitable for tracking the E region peak altitude over a period of time.

Chapter 5

Electrostatic potential model & derived lower thermospheric wind estimates for the low latitude ionosphere

5.1 Introduction

In this chapter, a three dimensional electrostatic potential model for the low latitude ionosphere is described. The model is built is a magnetic dipolar coordinate system. The physics based model consists of a second order nonseparable nonhomogeneous elliptic partial differential potential equation. Given realistic ionospheric input parameters, the model calculates perturbation potential and vector current density. The computed electric field components, together with Doppler shifts of type II radar echoes observed at the Jicamarca Radio Observatory, are employed to infer daytime zonal wind profiles in the equatorial E region. The potential model includes anomalous effects and is constrained by radar and magnetometer data. We first drive the magnetic dipole coordinate system and the relevant geometric scale factors of transformation.

5.2 The magnetic dipole coordinate system

The use of the dipole coordinates simplifies finding numerical solution of the partial differential potential equation mentioned above. Magnetic dipole coordinates and geometric scale factors are derived here utilizing a combination of the equation for magnetic field lines and the definition magnetic scalar potential.

A magnetic line of force is defined as a curve which is tangent to a magnetic field intensity $\mathbf{B}$. If $d\mathbf{s}$ is an arc length, the magnetic line of force may be represented by a set of difference equations,

$$d\mathbf{s} \times \mathbf{B} = 0 \tag{5.1}$$

Using the differential vector length element, $d\mathbf{s}$, defined in a spherical coordinate system, (r, θ, ϕ) shown in Figure 5.1, where r is a radial distance, θ is a colatitude ($\lambda = \frac{\pi}{2} - \theta$ is the corresponding latitude), and ϕ is an azimuth angle or longitude,

$$d\mathbf{s} = dr\hat{\mathbf{e}}_r + rd\theta\hat{\mathbf{e}}_\theta + r\sin\theta d\phi\hat{\mathbf{e}}_\phi \tag{5.2}$$

and the magnetic field vector,

$$\mathbf{B} = B_r\hat{\mathbf{e}}_r + B_\theta\hat{\mathbf{e}}_\theta + B_\phi\hat{\mathbf{e}}_\phi \tag{5.3}$$

the vector product (5.1) becomes (5.4) whose solution yields parameters that label a line of force.

$$\frac{dr}{B_r} = \frac{rd\theta}{B_\theta} = \frac{r\sin\theta d\phi}{B_\phi} \tag{5.4}$$

Assuming that the contribution to the current originating from the Earth's interior is much larger than other current sources (ionospheric and magnetospheric currents), the geomagnetic field can be considered irrotational, $\nabla \times \mathbf{B} \simeq \mathbf{0}$. Utilizing this assumption, the geomagnetic field vector can be written as the gradient of the magnetic scalar potential, $\mathbf{B} = -\nabla\varsigma$. The magnetic scalar potential may be expressed as,

$$\varsigma = -\frac{\mu_\circ}{4\pi}\mathbf{M} \cdot \nabla\left(\frac{1}{r}\right) = -\frac{\mu_\circ M}{4\pi}\left(\frac{\cos\theta}{r^2}\right) \tag{5.5}$$

where $\mathbf{M}$ is the magnetic dipole moment (defined in terms of the current flowing in the Earth's interior and the area enclosed by the current loop) which is shown schematically in Figure 5.1.

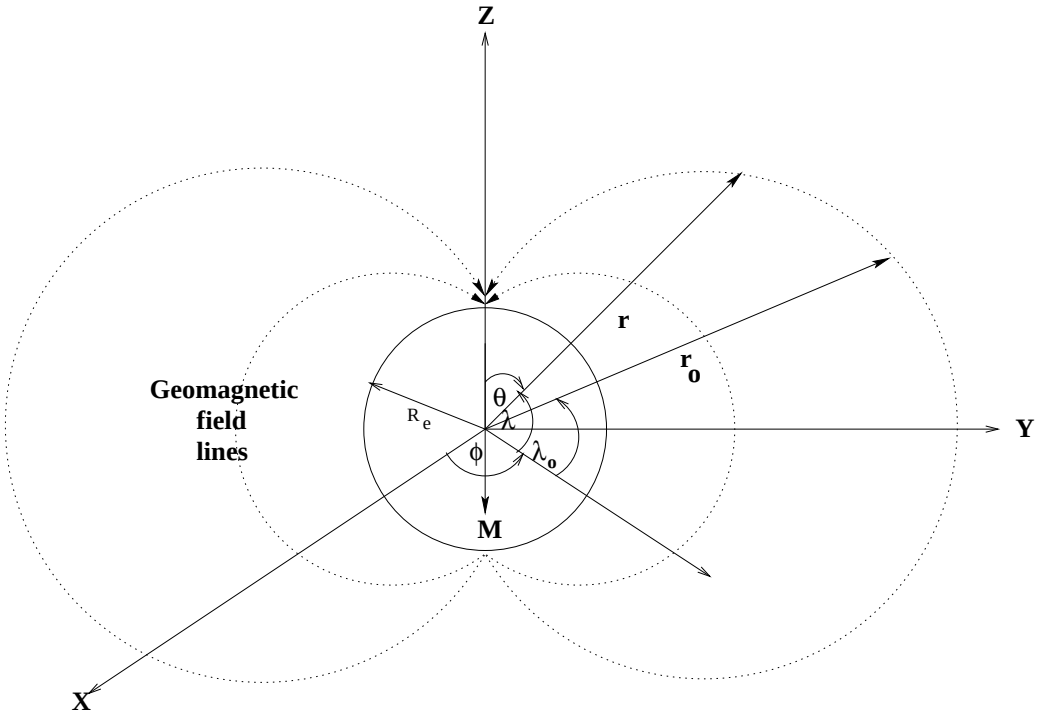

Figure 5.1: The spherical coordinate system. **M** is the magnetic dipole moment, r is the radial distance, λ is the latitude (θ is the colatitude), and ϕ is the azimuth angle. R_e is radius of the Earth.

The components of the magnetic field, (B_r, B_θ, B_ϕ), can therefore be derived from (5.5),

$$B_r = -\frac{\partial \varsigma}{\partial r} = -\frac{\mu_\circ M}{2\pi}\frac{\cos\theta}{r^3}$$

$$B_\theta = -\frac{1}{r}\frac{\partial \varsigma}{\partial \theta} = -\frac{\mu_\circ M}{4\pi}\frac{\sin\theta}{r^3} \tag{5.6}$$

$$B_\phi = -\frac{1}{r\sin\theta}\frac{\partial \varsigma}{\partial \phi} = 0$$

Rearranging (5.4) and using (5.6) we get,

$$\frac{1}{r}\frac{dr}{d\theta} = \frac{B_r}{B_\theta} = 2\frac{\cos\theta}{\sin\theta} = -2\frac{\sin\lambda}{\cos\lambda} \tag{5.7}$$

Further rearrangement of (5.7) gives rise to,

$$\frac{dr}{r} = 2\frac{d(\sin\theta)}{\sin\theta} = 2\frac{d(\cos\lambda)}{\cos\lambda} \tag{5.8}$$

Integrating (5.8) from an initial distance $r_\circ$ to the final distance r shown in Figure 5.1, the corresponding polar angles intercepted by the radial distances are $\lambda_\circ$ and λ, respectively,

$$\int_{r_\circ}^{r} \frac{dr}{r} = \int_{\lambda_\circ}^{\lambda} 2\frac{d(\cos\lambda)}{\cos\lambda} = \int_{\theta_\circ}^{\theta} 2\frac{d(\sin\theta)}{\sin\theta} \tag{5.9}$$

The result of the above integral is,

$$\frac{r}{r_\circ} = \frac{\sin^2\theta}{\sin^2\theta_\circ} \tag{5.10}$$

Equation (5.10) can be written as,

$$\frac{r}{\sin^2\theta} = \frac{r_\circ}{\sin^2\theta_\circ} = k \tag{5.11}$$

where k is a constant representing the invariance of the ratio of the radial distance to the square of the sine of the colatitude.

It can be seen from (5.11) that the constant k can be a multiple of the radius of the Earth, R_e, that is, $k = pR_e$,

$$pR_e = \frac{r}{\sin^2\theta} \tag{5.12}$$

Equation (5.12) yields the first element of the magnetic dipole coordinate system p. This coordinate depends on the radial distance and the location of the polar angle,

$$p = \frac{r}{R_e\sin^2\theta} \tag{5.13}$$

The second coordinate is derived from the definition of the magnetic scalar potential,

$$\varsigma(r,\theta) = -\frac{\mu_\circ M}{4\pi}\frac{\cos\theta}{r^2} \tag{5.14}$$

Normalizing (5.14) by the magnetic scalar potential evaluated on the surface of the Earth at $\theta = 0$, $\varsigma(R_e, 0)$, we obtain,

$$\frac{\varsigma(r,\theta)}{\varsigma(R_e,0)} = \left(\frac{R_e}{r}\right)^2 \cos\theta \tag{5.15}$$

where $\varsigma(R_e, 0) = -\frac{\mu_o M}{4\pi}\frac{1}{R_e^2}$.

The above ratio defined by a parameter, q, defines the second coordinate of the dipole coordinate system,

$$q = \left(\frac{R_e}{r}\right)^2 \cos\theta \tag{5.16}$$

The third coordinate is the azimuth angle, ϕ, which is also an element of the conventional spherical coordinate system.

The complete set of magnetic dipole system of coordinate forming an orthogonal system is given by:

$$(p, q, \phi) = \left(\frac{r}{R_e \sin^2\theta}, \left(\frac{R_e}{r}\right)^2 \cos\theta, \phi\right) \tag{5.17}$$

These coordinates are directed in the direction perpendicular to the geomagnetic field in the radially outward direction, in the direction of the geomagnetic field, and orthogonal to the first two coordinates in the azimuthal direction, respectively [*Hysell et al*, 2004]. These coordinates are schematically depicted in Figure 3.1.

5.2.1 Geometric scale factors

Using Pythagorean theorem, the square of the differential distance between two neighboring points, $(ds)^2 = d\mathbf{s} \cdot d\mathbf{s}$,

$$(ds)^2 = (dr)^2 + r^2(d\theta)^2 + r^2 \sin^2\theta (d\phi)^2 \tag{5.18}$$

On the other hand, the square of the corresponding distance element in the dipole coordinate system can be written as,

$$(ds)^2 = \sum_l h_l^2 (dl)^2 \tag{5.19}$$

The scale factors are defined as,

$$h_l^2 = \sum_j \left(\frac{\partial l}{\partial j}\right)^2 \tag{5.20}$$

where the coordinate l can take any one of the value of, (p, q, ϕ), whereas for the case at hand j assumes elements of spherical coordinates, (r, θ, ϕ).

Using (5.19), the length element becomes,

$$(ds)^2 = h_p^2 (dp)^2 + h_q^2 (dq)^2 + h_\phi^2 (d\phi)^2 \tag{5.21}$$

The fact that the two differential distance elements in (5.18) and (5.21) must be equal leads to,

$$dp = \left(\frac{1}{h_p}\right) dr = h_p^{'} dr$$

$$dq = \left(\frac{1}{h_q}\right) r d\theta = h_q^{'} r d\theta \tag{5.22}$$

$$d\phi = \left(\frac{1}{h_\phi}\right) r \sin\theta d\phi = h_\phi^{'} r \sin\theta d\phi$$

where the primed metric factors are related to unprimed factors reciprocally, $h_p^{'} = \frac{1}{h_p}$, $h_q^{'} = \frac{1}{h_q}$, and $h_\phi^{'} = \frac{1}{h_\phi}$.

As shown in (5.20), the scale factors of transformation are defined in terms of the total derivatives,

$$h_p^2 = \left(\frac{\partial p}{\partial r}\right)^2 + \frac{1}{r^2}\left(\frac{\partial p}{\partial \theta}\right)^2 + \frac{1}{r^2 \sin^2\phi}\left(\frac{\partial p}{\partial \phi}\right)^2$$

$$h_p^2 = \frac{1}{R_e^2 \sin^6\theta}\left(1+3\cos^2\theta\right) \tag{5.23}$$

$$h_q^2 = \left(\frac{\partial q}{\partial r}\right)^2 + \frac{1}{r^2}\left(\frac{\partial q}{\partial \theta}\right)^2 + \frac{1}{r^2\sin^2\phi}\left(\frac{\partial q}{\partial \phi}\right)^2$$

$$h_q^2 = \frac{R_e^4}{r^6}\left(1+3\cos^2\theta\right) \tag{5.24}$$

$$h_\phi^2 = \left(\frac{\partial \phi}{\partial r}\right)^2 + \frac{1}{r^2}\left(\frac{\partial \phi}{\partial \theta}\right)^2 + \frac{1}{r^2\sin^2\phi}\left(\frac{\partial \phi}{\partial \phi}\right)^2$$

$$h_\phi^2 = \frac{1}{r^2\sin^2\phi} \tag{5.25}$$

The geometric scale factors of interest here are the $h_p^{'}$, $h_q^{'}$, and $h_\phi^{'}$ which are related to h_p, h_q, and h_ϕ, respectively, in (5.22),

$$h_p^{'} = \frac{1}{h_p} = \frac{R_e \sin^3\theta}{(1+3\cos^2\theta)^{\frac{1}{2}}}$$

$$h_q^{'} = \frac{1}{h_q} = \frac{r^3}{R_e^2(1+3\cos^2\theta)^{\frac{1}{2}}} \tag{5.26}$$

$$h_\phi^{'} = \frac{1}{h_\phi} = r\sin\theta$$

5.3 Fluid model description

Generalizing (3.1) by incorporating pressure gradient and gravity forces, the ionospheric current density vector can be compactly written in terms of the drivers as,

$$\mathbf{J} = \hat{\mathbf{\Sigma}} \cdot (\mathbf{E} + \mathbf{U} \times \mathbf{B}) - \hat{\mathbf{D}} \cdot \nabla n + \hat{\mathbf{\Gamma}} \cdot \mathbf{g} \tag{5.27}$$

where the coefficients of the current drivers, in the right hand side of (5.27), namely the conductivity ($\hat{\mathbf{\Sigma}}$), pressure gradient ($\hat{\mathbf{D}}$) and gravity driven ($\hat{\mathbf{\Gamma}}$) tensors are

given below in dipole coordinates (p, q, ϕ). The anisotropic nature of current density in the ionosphere lies in the antisymmetric properties of these second rank tensors:

$$\hat{\mathbf{\Sigma}} = \begin{pmatrix} \sigma_P & 0 & -\sigma_H \\ 0 & \sigma_\circ & 0 \\ \sigma_H & 0 & \sigma_P \end{pmatrix} \tag{5.28}$$

$$\hat{\mathbf{D}} = \begin{pmatrix} d_P & 0 & d_H \\ 0 & d_\circ & 0 \\ -d_H & 0 & d_P \end{pmatrix} \tag{5.29}$$

$$\hat{\mathbf{\Gamma}} = \begin{pmatrix} e_P & 0 & -e_H \\ 0 & e_\circ & 0 \\ e_H & 0 & e_P \end{pmatrix} \tag{5.30}$$

where elements of $\hat{\mathbf{\Sigma}}$ are defined by equations (2.7) through (2.9), elements of $\hat{\mathbf{D}}$ are defined by equations (2.10) through (2.12), and elements of $\hat{\mathbf{\Gamma}}$ are defined by equations (2.13) through (2.15).

The current flowing in the ionosphere given by (5.27) must solenoidal. As long as currents driven by the background electric field, $\mathbf{E}_\circ$, the wind dynamo, $\mathbf{U} \times \mathbf{B}$, and other possible sources, are divergent, the ionospheric plasma instantly rearrange itself by establishing a polarization electric field, $-\nabla\Phi$. The three dimensional electrostatic potential model presented here is built on the premise of solenoidal current:

$$\nabla \cdot \mathbf{J} = 0$$

$$\nabla \cdot \left(\hat{\mathbf{\Sigma}} \cdot \nabla\Phi \right) = \nabla \cdot \left(\hat{\mathbf{\Sigma}} \cdot (\mathbf{E}_\circ + \mathbf{U} \times \mathbf{B}) - \hat{\mathbf{D}} \cdot \nabla n + \hat{\mathbf{\Gamma}} \cdot \mathbf{g} \right) \tag{5.31}$$

where the polarization electric field that drives the electrojet current and irregulatities is contained within the electrostatic potential Φ.

In order to compare electric field and thermally driven currents and determine the condition under which the divergence of thermal currents merits consideration, let us take the ratio of the Pedersen current component to the a perpendicular thermal current component in the right hand side of (5.31),

$$\left| \frac{\nabla_\perp \cdot (d_P \nabla_\perp n)}{\nabla_\perp \cdot (\sigma_P \mathbf{E}_\perp)} \right| \sim \frac{1}{L_\perp} \tag{5.32}$$

where we have assumed a single ion species in the E region (mean of NO^+ and O_2^+) in calculating the ratio. The ratio in (5.33) suggests that thermal currents will have significant contribution provided that the transverse plasma density gradient scale length ($L_\perp$) is much much less than a kilometer. Given that vertical gradient scale lengths of the ambient plasma are in the range of 6 - 8 km in the E region, the divergence of thermal currents is very small. However, the existence of broadband spectrum of plasma density irregularities (ranging from meter to kilometer scales) have been detected in the equatorial electrojet from their radar backscatter signatures in which case, (5.33) may not be small.

As far as divergence of diamagnetic current is concerned,

$$\nabla_\perp \cdot \left(d_H \nabla n_\perp \times \hat{\mathbf{b}} \right) = \left(\nabla_\perp n \times \hat{\mathbf{b}} \right) \cdot \nabla_\perp d_H \approx 0 \tag{5.33}$$

where the background vertical density gradients only are taken into account. However, this assumption fails around the terminator where horizontal gradients exist. Divergence of current driven by gravity has not been considered since it is small compared to other terms in (5.31).

By performing the divergence operations in (5.31), we obtain the linear second order inhomogenous nonseparable elliptic partial differential equation (PDE) in

the electrostatic potential with spatially varying coefficients,

$$\Upsilon\Phi(p,q,\phi) = \mathbf{R}(p,q,\phi) \tag{5.34}$$

where

$$\Upsilon = a\frac{\partial^2}{\partial p^2} + b\frac{\partial^2}{\partial q^2} + c\frac{\partial^2}{\partial \phi^2} + e\frac{\partial}{\partial p} + f\frac{\partial}{\partial q} + s\frac{\partial}{\partial \phi} \tag{5.35}$$

The coefficients of the second order differential operator, Υ, and the nonhomogenous term (the source or divergence of current drivers) of the PDE, are defined in equations (5.36),

$$\begin{gathered}
a = \sigma_p \frac{h_\phi h_q}{h_p}, \quad b = \sigma_\circ \frac{h_p h_\phi}{h_q}, \\
c = \sigma_p \frac{h_p h_q}{h_\phi}, \quad e = \frac{\partial a}{\partial p} + \frac{\partial (h_q \sigma_H)}{\partial \phi}, \\
f = \frac{\partial b}{\partial q}, \quad s = \frac{\partial c}{\partial \phi} - \frac{\partial (h_q \sigma_H)}{\partial p}, \\
\mathbf{R}(p,q,\phi) = \nabla \cdot \left(\hat{\mathbf{\Sigma}} \cdot (\mathbf{E}_\circ + \mathbf{U} \times \mathbf{B}) - \hat{\mathbf{D}} \cdot \nabla n + \hat{\mathbf{\Gamma}} \cdot \mathbf{g} \right)
\end{gathered} \tag{5.36}$$

Gradients in the Pedersen, direct and Hall conductivities in (5.36) are crucial for the first order partial derivative terms to have significant contributions to the PDE in (5.34). The same thing applies to the derivatives of the geometric scale factors. The quantity $e = \frac{\partial a}{\partial p} + \frac{\partial (h_q \sigma_H)}{\partial \phi}$ is related to a vertical variation of the Pedersen conductivity and zonal variation of the Hall conductivity. The second term in e is most likely significant around the solar terminator, whereas the first term is important in the E as well as F regions and most importantly around the conductivity boundaries. The quantity $f = \frac{\partial b}{\partial q}$ is related to gradient of parallel conductivity, it is very likely that the higher rate of parallel diffusion destroys

parallel gradients. The quantity $s = \frac{\partial c}{\partial \phi} - \frac{\partial (h_q \sigma_H)}{\partial p}$ represents the zonal divergence of Pedersen conductivity and vertical divergence of Hall conductivity. While the second term of s is particularly important in the E region, zonal divergence of Pedersen current typically occurs around the terminator.

5.4 Numerical procedures

We are seeking solution of $\Phi(p, q, \phi)$ in (5.34) in the dipole coordinates shown in Figure 3.1. In the dipole coordinate system, longitudinal and transverse plasma motion are marginally coupled, creating an orthogonal set of coordinates. Aligning the system of coordinate to the magnetic dipole system simplifies the numerical calculations significantly. Because of the use of the dipole coordinates, the PDE in (5.34) is free from mixed partial derivative terms which would have been the case had a spherical coordinate system been empolyed.

We have employed UCAR's (University Corporation for Atmospheric Research) MUDPACK (Multigrid Software for Elliptic Partial Differential Equations) package version 4.0 [*Adams*, 1998] to numerically solve the second order PDE shown in (5.34). The MUDPACK package discretizes linear PDEs using a finite difference formula on solution grids. MUDPACK utilizes multigrid iterative technique that combine the classical Gauss-Seidel iterative techniques with subgrid refinement procedures.

A multigrid method is a scheme to improve the rate of convergence by treating the problem on a hierarchy of grids. The method arises from the fact that long wavelength errors in the solution are dissipated on coarser grid while the shorter wavelength errors are dissipated on a finer grid. By iterating and transferring approximations and corrections at subgrid levels, a good initial guess and rapid

convergence at the fine grid level could be achieved. Multigrid iteration requires less storage and computation than direct methods for nonseparable elliptic PDEs [*Adams*, 1998].

5.4.1 Simulation space

The inhomgenoeuos term, which are function of divergences of (i) the tensors shown from (5.28) to (5.30), (ii) density gradients, (iii) the zonal electric field and wind fields, and (iv) gravitational field; and the variable coefficients in (5.36) are discretized on the interior of the solution region. Along with boundary conditions, they specify the numerical problem for solving for the electrostatic potential $\Phi(p, q, \phi)$. The solution space contains 73, 73, and 37 grid points in the (p, q, ϕ) cooordinates, respectively. The simulation space is a segment of the equatorial ionosphere in the South American sector centered at the geographic latitude, 12° 33'S, and geographic longitude, 283°E. The simulation space covers between 85 to 150 km of altitude and is $\pm 10°$ wide both in latitude and longitude. Since the magnetic declination is nearly zero in this sector of the globe, we need not consider effects of a tilted dipole.

5.4.2 Boundary conditions

Given boundary conditions, the coefficients, and the forcing term in (5.36), the PDE solver calculates the perturbation potential at each grid point. Neumann boundary conditions are imposed on the extreme q boundaries (the feet of the geomagnetic field lines), the zonal (or ϕ) boundaries, and the lower p boundary. The boundary condition imposed on the upper p boundary is that vertical perturbation electric field is that of a perfectly efficient wind driven dynamo.

We initially force the potential model using the NCAR TIME-GCM model zonal winds shown in Figure 5.2. Ultimately, zonal wind profiles are inferred from type II radar echoes in subsequent iterative model runs.

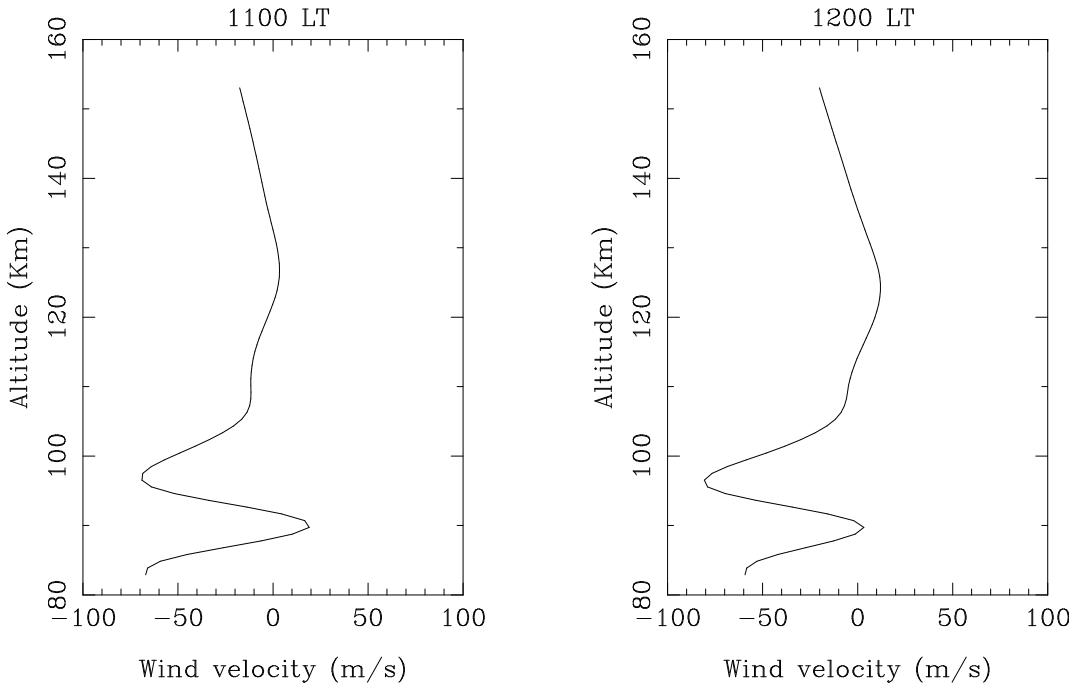

Figure 5.2: Zonal winds in the equatorial E region derived from the NCAR TIME/GCM model for center of the simulation space, geographic latitude, 12° 33'S, and geographic longitude, 283°E.

5.5 Model input parameters

Neutral atmosphere densities and temperatures used by the potential model were derived from the MSIS-E-90 Atmosphere Model, and geomagnetic field components were obtained from the IGRF model. Electron density profiles, plasma composition, and electron/ion temperatures were derived from the IRI. For our model

runs, the IRI-2001 model electron densities were combined with E region electron density profiles derived from an α Chapman function, based on the result found in Chapter 4.

5.5.1 Collision frequency models

We have employed ion-neutral collision frequency models developed by *Richmond* [1972],

$$\nu_{1n} = \left((1.07N_1 + 1.06N_2)(\frac{T}{500})^{-0.16} + 0.60N_3(\frac{T}{500})^{-0.19} \right) 10^{-22}\frac{\Omega_1}{B} \quad (5.37)$$

$$\nu_{2n} = \left(1.08N_1(\frac{T}{500})^{-0.17} + 2.02N_2(\frac{T}{500})^{0.37} + 0.61N_3(\frac{T}{500})^{-0.19} \right) 10^{-22}\frac{\Omega_2}{B} \quad (5.38)$$

$$\nu_{3n} = \left(0.89N_1(\frac{T}{500})^{-0.20} + 1.16N_2(\frac{T}{500})^{0.05} + 0.89N_3(\frac{T}{500})^{0.36} \right) 10^{-22}\frac{\Omega_3}{B} \quad (5.39)$$

where the subscripts ν_{1n}, ν_{2n}, and ν_{3n} refer to neutral-ion collision frequency for NO^+, O_2^+, and O^+ respectively, Ω_1, Ω_2, and Ω_3 are the corresponding cyclotron frequencies. N_1, N_2, and N_3 represent neutral densities of N_2, O_2, and O respectively. T is neutral temperature in Kelvins.

Our potential model uses an electron-neutral collision frequency model (5.40) developed by *Gagnepain et al* [1977] and an electron-ion collision frequency model (5.41) developed by *Nicolet* [1953],

$$\nu_{en} = \left(4.11N_1(\frac{T_e}{300})^{0.95} + 2.95N_2(\frac{T_e}{300})^{0.79} + 1.09N_3(\frac{T_e}{300})^{0.85} \right) 10^{-26}\frac{\Omega_e}{B} \quad (5.40)$$

$$\nu_{ei} = \left(34.0 + 4.18\ln(\frac{T^3}{n_e 10^{-6}}) \right) n_e 10^{-6} T^{-\frac{3}{2}}\frac{\Omega_e}{B} \quad (5.41)$$

In these collision models, collision frequencies are expressed as a function of neutral atmospheric densities and temperatures which we derived from the MSIS

model. For specifically dealing with the electrojet region altitudes, we have defined an effective electron collision frequency parameter that utilizes anamalous collision theories to incorporate electron collision enhancements due to wave-particle interactions (further discussion on this is provided below).

5.5.2 *E* region electron density profiles

We have seen in Chapter 4 that the IRI model does not accurately predict electron densities below the E region peak. The IRI model overestimates electron densities and the underlying conductivities there. Since electron density profiles derived from the α Chapman function reproduce E region density profiles measured by a bistatic coherent scatter radar at the Jicamarca Radio Observatory [*Shume et al*, 2005a], our model represents E region electron densities below the E region peak by a Chapman function. In Figure 5.3, we have shown, (i) an example electron density profiles derived from the Chapman function (dots), which will be utilized in the numerical calculation, and (ii) IRI model electron density profile (solid line). The profiles are constructed for a March 22, 2003, 1100 local time conditions. To derive the electron density profiles, based on the α Chapman function, the E region peak density and solar zenith angle data were obtained from IRI model parameter specifications, and the neutral scale height was calculated using parameters from the MSIS model. The electron density profiles used in the potential modeling agrees with the FIRI lower ionosphere model (which is an improved IRI model based on electron density data measured *in situ* by the Faraday rotation technique) [*Friedrich and Torkar*, 2001].

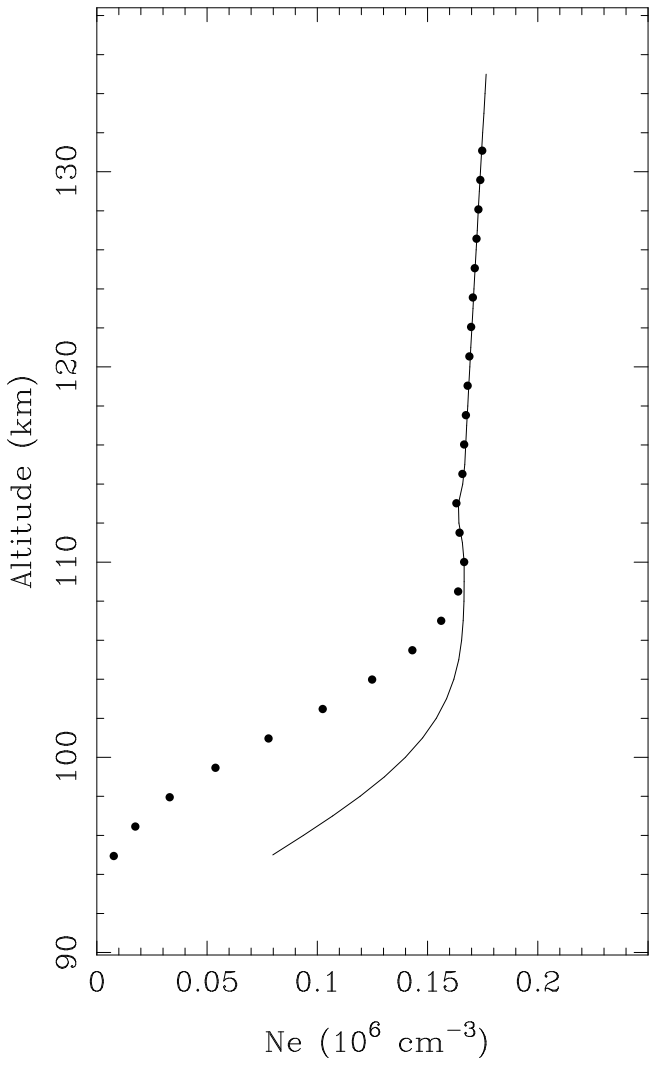

Figure 5.3: Electron density profiles in the equatorial ionosphere on March 22, 2003 1100 LT. Dark dots are the electron density profile derived from the α Chapman function, and the solid line represents electron densities from IRI model specifications.

5.5.3 Anomalous collision effects

Electric fields of short wavelength electrojet irregularities can enhance electron transport via anomalous collisions [*St.-Maurice*, 1987; *Ronchi and Sudan*, 1990].

The resulting changes in the properties of the medium, in turn, modify the growth rate and Doppler velocity of the irregularities. Due to anomalous collision effects (or wave-particle collisions), an effective electron collision frequency, ν_e^t, will then have a classical collision component, ν_e, and an anomalous collision contribution, ν_e^* , that is,

$$\nu_e^t \equiv \nu_e + \nu_e^* \tag{5.42}$$

Using first order smoothing of electric field and density fluctuations of electrojet irregularities, *St.-Maurice* [1987], and *Ronchi and Sudan* [1990] have derived the mathematical relation between anomalous electron collisions and the amplitude of the small scale turbulence strength in the electrojet medium, $\left\langle \left| \frac{\delta n}{n} \right|^2 \right\rangle$:

$$\nu_e^* = \frac{\Psi_\circ}{1+\Psi_\circ} \frac{\Omega_e^2}{2\nu_e} \left\langle \left| \frac{\delta n}{n} \right|^2 \right\rangle \tag{5.43}$$

The introduction of anomalous collisions transforms the ordinary anisotropic factor to a new anisotropy factor ($\Psi_\circ \rightarrow \Psi^{'}$) defined by,

$$\Psi^{'} \equiv \Psi_\circ + \Psi^* \tag{5.44}$$

where Ψ^* is the addition due to anomalous effects. $\Psi_\circ$ and Ψ^* are given by the first and second terms of the right hand side of equation (5.45), respectively,

$$\Psi^{'} = (\nu_e + \nu_e^*) \frac{1}{\Omega_e} \left(\sum_j f_j \frac{\Omega_j}{\nu_j} \right)^{-1} \tag{5.45}$$

where f_j is the fractional part of ion species of type j.

As indicated in Chapter 3, reproducing the electrojet current density profiles measured *in situ* has been a challenge. By inferring the anomalous collision frequencies using a relative plasma density fluctuation measurement from a rocket flight experiment [*Pfaff et al*, 1987], *Ronchi and Sudan* [1990] have shown that the

shape and magnitude of the equatorial electrojet calculated by their model can, to a good extent, reproduce the measured current density profiles. Likewise, the measured current density profile was reproduced by *St.-Maurice* [1988]. The effect of the anomalous collision term is to decrease the magnitude of the calculated electrojet current and elevate the altitude of the current maximum.

Our electrostatic potential model allows for anomalous effects by using ν_e^t and its byproduct, the effective anisotropy factor Ψ'. In order to close (5.43), we have modeled the relative density fluctuation by a Gaussian function following the work of *Ronchi and Sudan* [1990]. The Gaussian model function is derived based on plasma density irregularity data measured by rocket flights in the equatorial E region [*Pfaff et al*, 1987]. We have used the anomalous effects to constrain our model calculations. The amplitude and width of the Gaussian function are tuned such that the measured horizontal and vertical magnetic field components derived from Jicamarca magnetograms agree with model calculations. We discuss how the Gaussian model is implemented in the computational model in the upcoming section.

5.6 Vertical polarization electric field and zonal current

The model was run for a March 22, 2003, 1100 local time geophysical conditions to calculate the electric field and current density in the equatorial E region in the Peruvian sector. A one dimensional cut through the three dimensional simulation space showing model results are displayed in Figure 5.4. The calculated vertical polarization electric field is shown in panel I, and the zonal current density in panel II. The solid lines in both panels show model results in the absence of winds whereas the dotted curves are model calculations done in the presence of winds. It

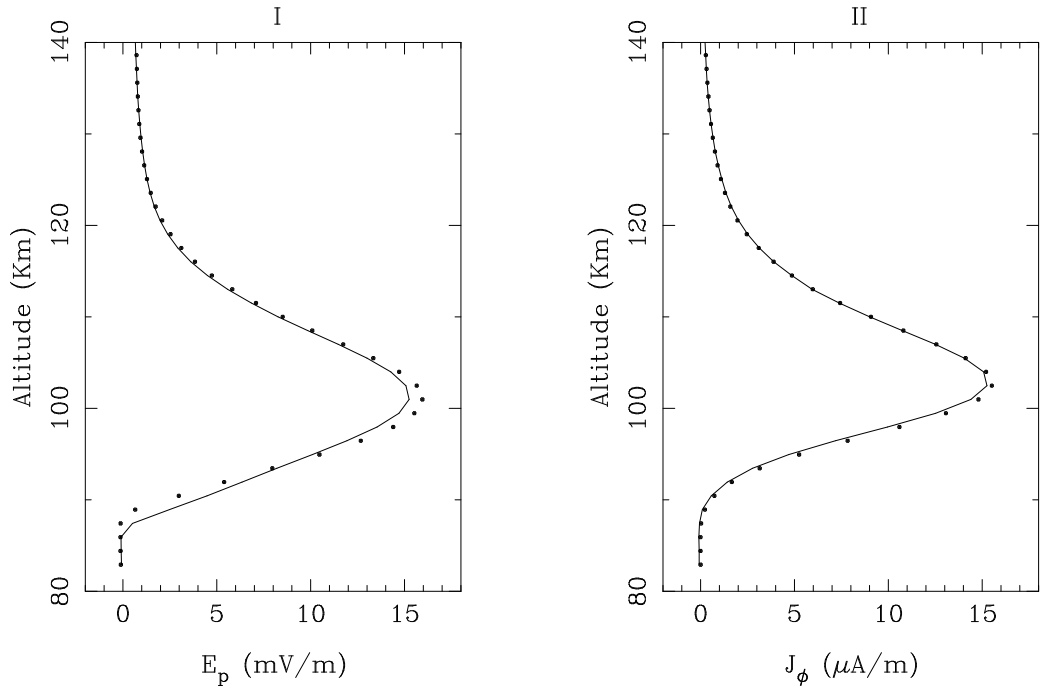

Figure 5.4: Panel I shows calculated vertical polarization field in the absence (solid line) and presence (dotted lines) of zonal winds for March 22, 2003 1100 LT. Panel II shows the calculated zonal current density in the absence and presence zonal winds for the same date and local time.

is clearly shown in panel I that the strength of the polarization field is enhanced in proportion to uB in the peak region. On the other hand, the current is neither significantly enhanced nor reduced in the presence of zonal winds proving once again the assertions of Chapter 3. The vertical polarization electric field that drives the electrojet Hall current maximizes at about 100 km altitude. The electrojet current peaks at an altitude of about 103 km.

5.7 Inferring zonal wind velocity profiles in the equatorial *E* region

Mid- and high-latitude E region winds can be derived from incoherent scatter radar (ISR) ion drift measurements. Near the magnetic equator, however, the ISR technique generally fails due to clutter from plasma irregularities in the equatorial electrojet. This paper presents a technique which utilizes the electrojet irregularities themselves for inferring zonal winds in the equatorial E region.

Type I and II spectra are radar signatures of electrojet irregularities that are observed if the Farley-Buneman and gradient-drift instabilities are excited [*Farley*, 1985]. The electrojet current and the irregularities are mainly driven by the vertical polarization electric field, an outcome of the complex interaction between the horizontal geomagnetic field geometry, the Cowling conductivity, the background zonal electric field, and the zonal winds. The Doppler shifts of the irregularities are related to the polarization electric field, the winds, and the dynamo fields they induce by a linear dispersion relation [*Fejer et al*, 1975; *Rogister and D'Angelo*, 1970; *Fejer and Kelley*, 1980]. The winds hence modulate the Doppler shifts of irregularities [*Sato*, 1975; *Balsley et al*, 1976; *Broche et al*, 1978; *Devasia and Reddy*, 1995; *Hysell et al*, 2002]. Doppler shift profiles from the electrojet measured routinely at Jicamarca are therefore a potential source of information about the lower thermosphere winds.

Utilizing the presence of electrojet plasma irregularities, coherent scatter radar techniques have been employed as a diagnostic tool to infer electric fields [*Balsley*, 1969, 1973; *Balsley et al*, 1976; *Reddy et al*, 1987; *Devasia and Reddy*, 1995; *Hysell and Burcham*, 2000; *Chau and Woodman*, 2004] as well as electron density

profiles [*Hysell and Chau*, 2001; *Shume et al*, 2005a]. These parameters cannot be derived from incoherent scatter radar techniques due to the clutter produced by the irregularities themselves. Coherent scatter from the electrojet is routinely monitored using a variety of antenna configurations at the Jicamarca Radio Observatory (JRO).

5.7.1 Central question

The central question is, given measured Doppler shifts of type II radar echoes, how can we infer zonal wind velocity profiles in the equatorial electrojet? We have developed a numerical strategy that combines theoretical models, coherent and incoherent scatter radar measurements, and magnetometer observations. A three dimensional numerical model which solves for the electrostatic potential (which was described in the previous section) throughout the low-latitude ionosphere is run, assuming a zonal neutral wind profile and incorporating measurements of the background zonal electric field derived from incoherent scatter radar measurements. The model predicts the vertical profile of type II echo Doppler shifts according to the linear dispersion relation for gradient drift waves. These profiles are compared with profiles measured using a 50 MHz radar with an oblique, narrow antenna beam at Jicamarca. The neutral wind profile is then tuned for optimal model-data agreement. Magnetometer data are incorporated to help account for effects of anomalous effects and thereby constrain the model.

5.7.2 Research review: zonal wind estimation

Ever since so-called type I and II radar echoes were first observed, attempts have been made to extract wind estimates from them. *Balsley et al* [1976] pointed

out that, since the Doppler shifts are functions of the neutral wind velocity, the latter can be indirectly inferred from the radar echo. *Broche et al* [1978] made a theoretical analysis of the linear dispersion relation and pointed out that, not only the winds themselves but also the dynamo electric fields they generate must be considered. *Reddy et al* [1987] inferred vertical profiles of the zonal electric field in the equatorial ionosphere in the Indian sector from measured phase velocities of Type II radar echoes, but their inference ignored the influence of the zonal winds at electrojet heights. However, zonal winds in the equatorial ionosphere are not negligible as shown by rocket chemical release experiments [*Larsen and Odom*, 1997; *Larsen*, 2002]. *Devasia and Reddy* [1995] outlined a method to calculate zonal wind profiles in the equatorial electrojet region from the phase velocity of Type II echoes, but their method has limited practical applicability since they neglected the effects of the background electric field. A comprehensive theoretical and computational treatment of the problem was presented by *Hysell et al* [2002], who drove a three-dimensional potential model for the equatorial electrojet region with winds derived from the NCAR TIME-GCM model. They predicted radar data generally consistent with observations but did not solve the inverse problem and infer winds from radar measurements. We take up the problem of inverting winds from coherent radar data from here.

5.7.3 Type II radar echo observations at the Jicamarca Radio Observatory

An oblique coherent scatter radar system is used at the Jicamarca Radio Observatory to measure Doppler shifts of electrojet irregularities. The oblique system is comprised of a 50 MHz radar with an antenna array of 16 widely spaced tilted

Yagi elements. The antenna arrays are arranged obliquely in such a way that a component of the Doppler velocity of the zonally propagating plasma irregularities can be captured.

Doppler velocities of type II echoes used for inferring wind profiles were estimated from the following experimental arrangement. The main radiation beam is directed westward at an angle of 53.3° to the zenith and have a half power full beamwidth of about 1°. The width of the transmitted pulse was 10μs, and the corresponding range resolution of the experiments was 1.5 km. The backscatter spectra observed with the oblique antenna system generally show signatures of both type I and type II echoes, similar to those shown in Figure 2.6 and Figure 2.7, respectively. We have separated out type II Doppler shifts from type I for the purpose of zonal wind profile inference. To accomplish that, we have used a Gaussian function fitting procedure. The procedure followed is to fit the measured Doppler spectra with a superposition of double Gaussian curves. We interpret the Doppler shift of the spectral component with narrower width and which saturates close to the ion acoustic speed as type I, and the ones with a greater spectral width as type II. To calculate the altitude of the scatters, we estimated the range based on the radar scattering geometry. The measured Doppler shift profiles of type II echoes are shown in Figure 5.7 and Figure 5.8 by circles with error bars. The solid line running through them is the predicted Doppler profile, which is discussed in the next section. The expected uncertainty was about 7 m/s.

5.7.4 Techniques for calculating *E* region zonal wind velocity profiles

Experimentally, type II Doppler velocities are estimated utilizing the radar experiments described above. Theoretically, our numerical model predicts Doppler velocity profiles. To be able to make the prediction, we have formulated an expression for the Doppler velocity of gradient drift irregularities from the linear theory of electrojet instabilities (described in Chapter 2). The Doppler velocity is a function of the polarization electric field, radar zenith angle, zonal wind velocity, and the anisotropy factor Ψ'. Techniques for retrieving zonal wind profiles presented below invloves combining the linear dispersion relation for gradient drift irregularities, the three dimensional electrostatic potential model, and Doppler velocity profiles of Type II radar echoes. The model tunes the winds as described below for best model-data agreement.

The linear dispersion relation of electrojet irregularities

According to the linear theory, the Doppler frequency of electrojet irregularities can be written as (2.44). A result which was derived by [*Fejer et al*, 1975; *Rogister and D'Angelo*, 1970; *Fejer and Kelley*, 1980].

In the electrojet region, electrons are magnetized, $\nu_e \ll \Omega_e$. The motion of electrons is thus more or less completely decoupled from the neutral atmosphere motion, and is controlled by the geomagnetic field. The drift velocity of electrons can therefore very well be approximated by the $\mathbf{E} \times \mathbf{B}$ drift, where the total vector electric field $\mathbf{E}$ has a background component ($\mathbf{E}_\circ$) and a perturbation electric field component ($-\nabla\mathbf{\Phi}$).

Due to heavy mass of ions, ions are collisional, $\nu_{in} \gg \Omega_i$. The motion of ions

is thus controlled by collision with the neutral atmosphere. The ion drift velocity can therefore be approximated by the neutral zonal wind velocity throughout the electrojet region.

Utilizing the above physical grounds, the Doppler velocity of type II irregularities (2.44) may be described as follows,

$$\frac{\omega(p)}{k} \simeq \frac{\sin(\beta)}{B(1+\Psi')}\left(\cot\beta(\frac{1}{h_\phi}\frac{\partial\Phi}{\partial\phi} - E_\circ) - \frac{1}{h_p}\frac{\partial\Phi}{\partial p} - \Psi' Bu(p)\right) \tag{5.46}$$

where β is the radar zenith angle, $E_\circ$ is the background zonal electric field, $u(p)$ is zonal wind profile. Due to shortage of reliable vertical wind information, the influence of vertical winds on the electrojet system is ignored altogether in our wind estimation algorithm. The influence of meridional winds on the expression for the Doppler velocity (5.46) is ignored as well since meridional winds blow almost parallel to the geomagnetic field near the magnetic equator and have negligible dynamo effects there.

Procedures for inferring zonal wind velocity profiles

We have employed the following numerical scheme for zonal wind profile inference: The model estimates zonal wind velocities iteratively. Winds are expressed in terms of a linear combination of a linearly independent basis functions. They are related to the vertical extensions of the Hough basis functions and consists of the diurnal and semi-diurnal tidal modes shown in Figure 5.5 [*Chapman and Lindzen*, 1970]. Initially, the model is driven by wind profile based on NCAR TIME-GCM model predictions. Doppler shift profiles are then predicted using (5.46) and compared with the Doppler velocity profile measured by the oblique coherent scatter radar. Iteration continues by updating the winds, adding a fraction of the difference between the measured and predicted Doppler profiles each time.

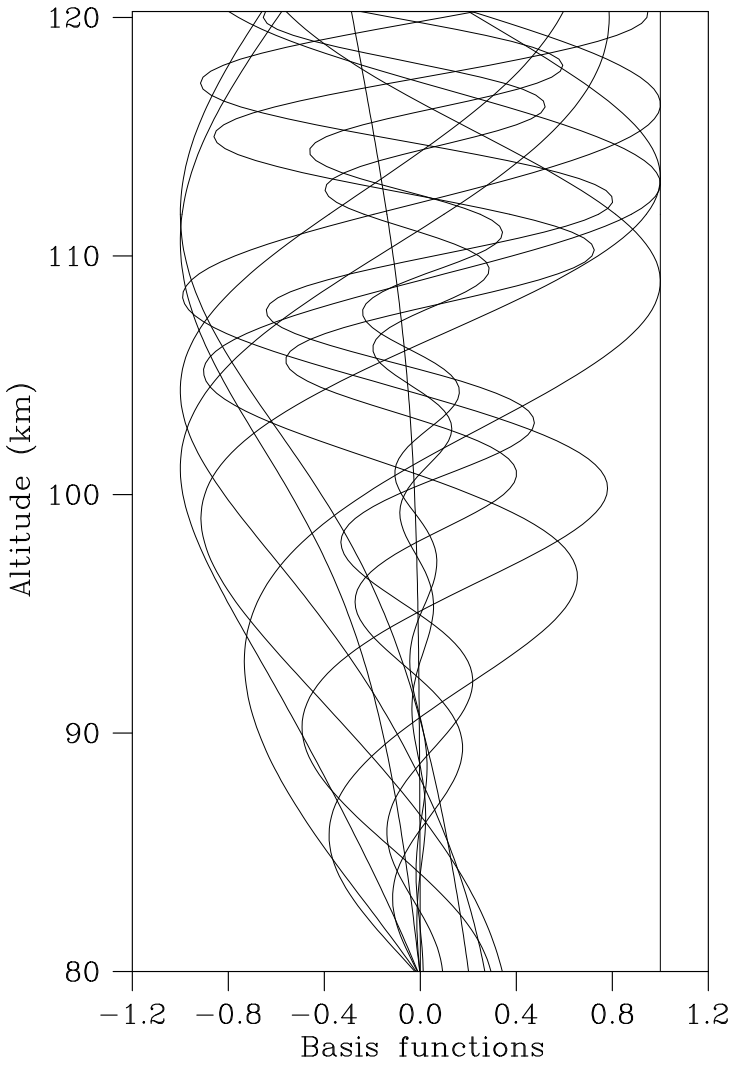

Figure 5.5: Basis functions used in the zonal wind inference. We have used a linear combination of the orthogonal diurnal and semidiurnal tidal modes shown in the figure derived from the vertical extension of the hough functions [*Chapman and Lindzen*, 1970].

Model-data agreement is seen to improve rapidly, first at low altitudes and later higher up. Iteration ceases when the χ^2 difference between modeled and measured Doppler shifts falls below a threshold, at which point the zonal wind profile has

been estimated.

5.7.5 Model constraints

The calculation of the potential in a least square sense is constrained by: (i) the background zonal electric field, $E_\circ$, which we have derived from incoherent scatter data from the Jicamarca radar, and (ii) horizontal and vertical magnetometer data, which can be predicted from the currents that flow in our model.

Electric field

We have performed the model calculation procedure for March 22, 2003, 1100 LT conditions. For this run, the background electric field constraining the model was set to 0.4 $\frac{mV}{m}$. This electric field value is extracted from average vertical plasma drift radar data. In relation to this, *Chau and Woodman* [2004] have pointed out that average vertical drifts derived from incoherent scatter data agree with vertical drifts from the so called 150 km echoes at Jicamarca. Below 150 km, however, we expect the zonal electric field to vary with altitude. The strategy we adopted to get the proper background zonal electric field is to make an initial guess and modify the guess in such away that the calculated electric field at the top of the simulation space, $E_\circ - \frac{1}{h_\phi}\frac{\partial \Phi}{\partial \phi}$, matches the electric field data derived from the radar, which was 0.4 $\frac{mV}{m}$ for the date and local time mentioned above.

Magnetic field

Our wind estimation was also constrained by the horizontal and vertical magnetometer data from March 22, 2003, 1100 LT. The net measured horizontal and vertical components of magnetometer deflections, which are caused by the electro-

jet current, are obtained by subtracting the horizontal and vertical components measured at the Jicamarca radar site, located at 2° North magnetic latitude, from those measured at Piura, an off equatorial station at 6°8' North magnetic latitude. The resulting horizontal and vertical components are again subtracted from the nighttime baseline magnetometer records at Jicamarca. This was done to remove current sources other than the equatorial electrojet which might cause magnetometer deflections. The horizontal and vertical magnetic field components calculated

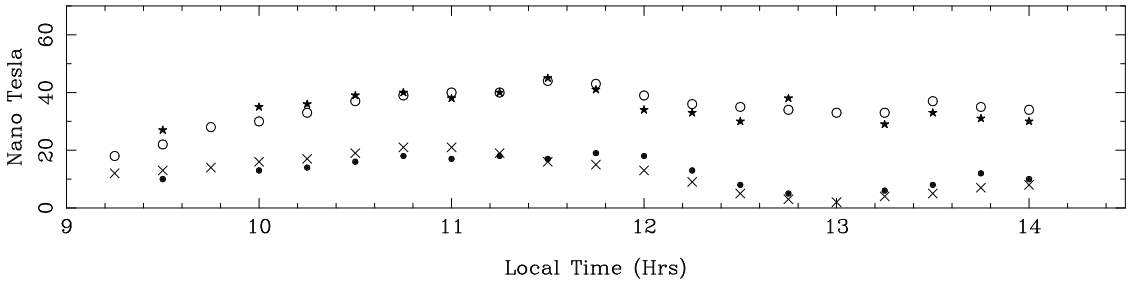

Figure 5.6: Comparison between the horizontal and vertical components of the measured and calculated magnetic field (nT) on March 22, 2003. Circles are measured horizontal components, stars are calculated horizontal components, crosses are measured vertical components, and dots are calculated vertical components.

by our model were compared with the measured horizontal and vertical components of magnetic field at Jicamarca. The magnetic field calculations, along with the wind estimations, are repeated by varying the turbulence strength parameter until the agreement between the calculated and measured magnetic fields is close. Setting the density fluctuation amplitude to 2% of the background density, a value within the range of rocket measured relative density fluctuation [*Pfaff et al*, 1987], the calculated and measured magnetic fields agree well. The calculated horizontal

and vertical components were found to be 38 and 17 nT respectively, and the measured horizontal and vertical components were 40 and 21 nT for March 22, 2003 at 1100 local time.

We have run the potential model on quarter of an hour intervals from 930 LT to 1400 LT for the day mentioned above. The zonal background electric field is time varying and is updated at each time step according to the Jicamarca drifts database. We have varied the turbulence strength parameter, $|\frac{\delta n}{n}|$, from 2 to 5% to force agreement between the calculated magnetic field components. The wind profiles and magnetic field components were calculated using the procedures described above. The results of the magnetic field comparison are depicted in Figure 5.6. Circles and stars are measured and calculated horizontal magnetic field components, respectively. The crosses and dots are measured and calculated vertical magnetic field components, respectively. Overall, the agreement is satisfactory over the time span in question. We were able to recover magnetometer observations using measured electric fields, type II electrojet Doppler shift profiles, incorporating reasonable turbulence strength parameters, and assuming plausible wind values.

5.7.6 Calculated zonal wind profiles

The calculated zonal wind velocity profile (broken line with error bars) for March 22, 2003, 1100 LT is plotted in figure Figure 5.7. The coordinate convention we have employed here is that positive values imply eastward directed zonal winds but westward-propagating electrojet irregularities. Also shown on the same graph are measured (dots with error bars) and model predicted (solid line) type II echo Doppler shifts. The calculated Doppler velocity profile has clearly reproduced

the measured type II echo Doppler shift profile. The Doppler shifts agreement and the magnetic field components comparison mentioned above suggest that the calculated winds are representative of daytime zonal wind profiles in the equatorial electrojet region.

The calculated wind profile shown in Figure 5.7 has a magnitude of about 60 m/s and directed eastward at the center of the electrojet. The wind is directed westward with a relatively smaller magnitude at the lower edge of the electrojet. As shown by equation (5.46), eastward dynamo winds slow down gradient drift waves in the daytime by opposing the driving vertical polarization electric fields whereas westward winds speed up the propagating irregularities. The calculated wave Doppler velocity around 106 km would have been faster, had the magnitude of the eastward wind been smaller than that calculated. Westward winds were needed in the bottomside to drive the waves in the collisional lower electrojet region.

The model was also run for a September 24, 2003, 1025 LT conditions. We have followed procedures identical to the March 22, 2003, 1100 LT model run. For this run, a background electric field value of 0.475 $\frac{mV}{m}$ was used. The resulting predicted wind profiles are plotted in Figure 5.8. The amplitude and phase of the calculated wind profiles are comparable to the March 22, 2003, 1100 LT calculated zonal winds.

5.7.7 Uniqueness and sensitivity

The calculated potential at a given altitude is a function of the winds not only at that altitude but also all altitudes below. In other words, the influence of winds telegraphs from lower altitude of the simulation space through to higher altitudes

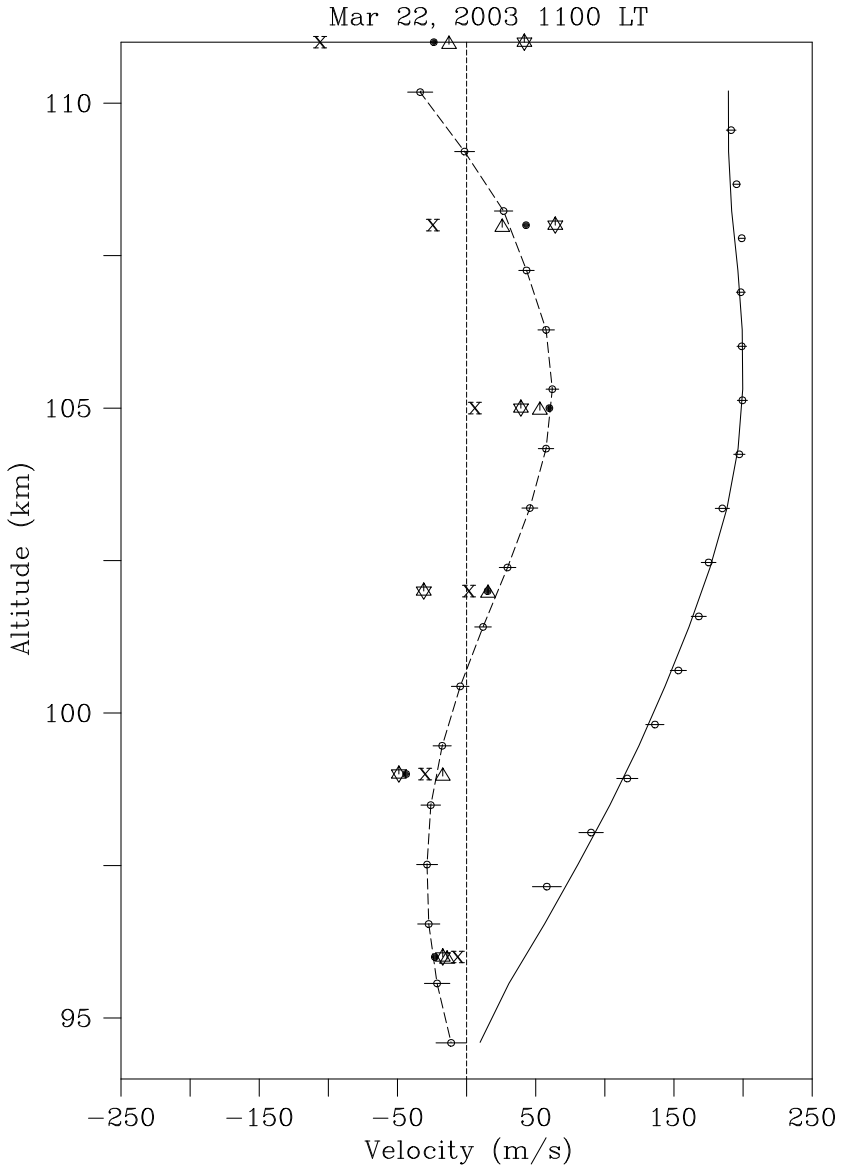

Figure 5.7: Comparison of the calculated zonal wind velocity profile (broken line) in the equatorial E region with winds measured by WINDII instrument onboard the UARS satellite (crosses, stars, dots, and triangles). The solid line shows the calculated phase velocity. The dots with error bars are phase velocities of type II echoes.

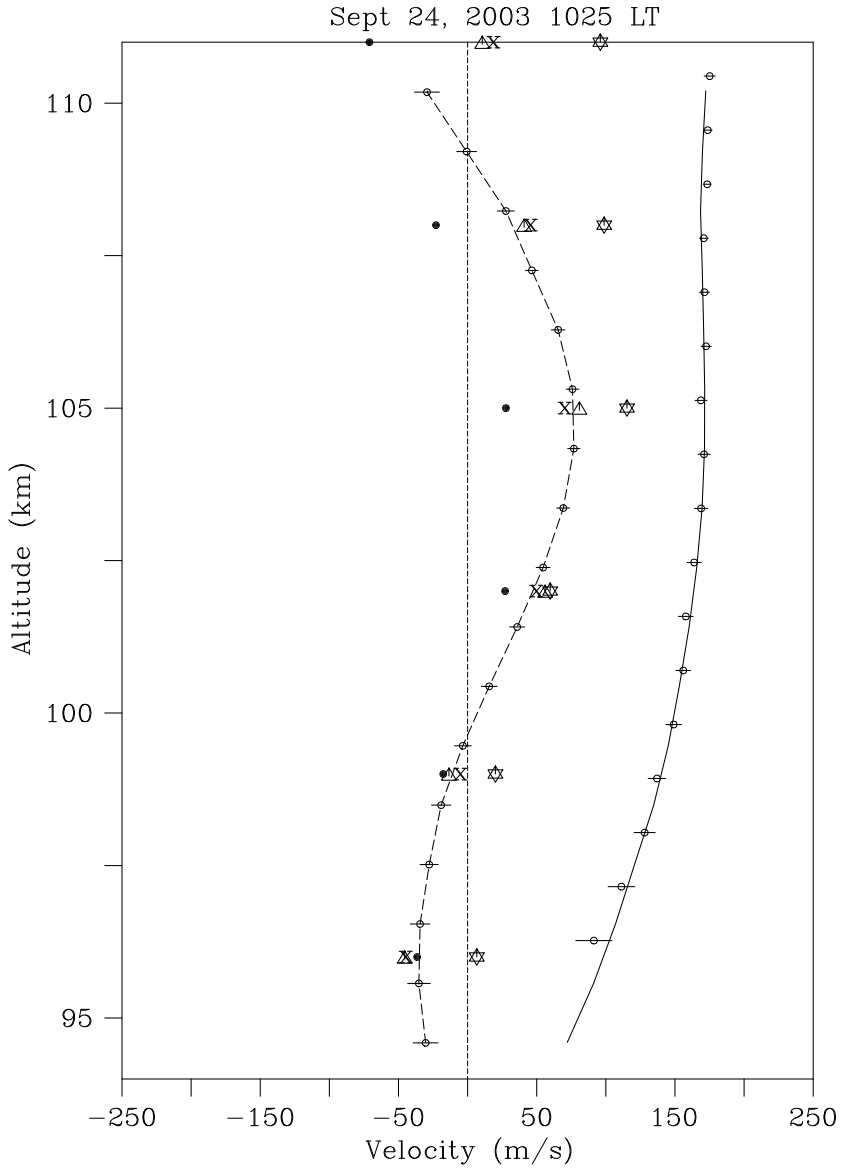

Figure 5.8: Same as Figure 5.7 but for September 24, 2003, 1025 local time.

by the model potential calculations. Winds do not generate dynamo fields in the lower edge of the electrojet (below about 93 - 95 km altitudes), however, since conductivities drop significantly in that region. Zonal winds could, therefore, be uniquely inverted from Doppler velocity data since winds have negligible dynamo

effect below altitudes for which we have Doppler shift data. Hence, the ionosphere medium works such that uniqueness of the wind solution we sought for is guaranteed. This same argument was also used in a modeling work by *Devasia and Reddy* [1995].

We have conducted an ensemble analysis of the wind calculation to examine the sensitivity of the employed numerical procedures. We have examined the response of the calculated wind profiles to variations in the Doppler and electric field data within the uncertainities of their respective measurements. The results of the analysis are displayed by the error bars on the calculated wind profiles (broken lines) in Figure 5.7 and Figure 5.8, the rms spread is about 8 m/s on average.

5.7.8 Zonal wind validation

Figure 5.7 also shows made a comparison between the calculated winds and a wind data set measured by the WINDII instrument onboard Upper Atmopshere Research Satellite (UARS). UARS had a nearly circular orbit at 585 km inclined at 57° to the equator. The instruments onboard were mounted at 90° to the spacecraft velocity vector and could see to 80° latitude in one hemisphere and to 34° to the other [*Reber et al*, 1993]. The WINDII instrument recorded zonal and meridional wind components over a large span of latitudes, longitudes and altitudes. The data used in our study were recorded by the WINDII instrument when it looked within ±5° of the latitude and longitude of the Jicamarca radar site. The data correspond to September 19, 1992 early afternoon (crosses), October 31, 1992 late morning (stars), and November 26, 1992 early afternoon (dots and triangles). The local time and solar flux level of the data are comparable with our model run conditions. As can be seen in the figure, the calculated wind profile has the same

envelope and phasing as the WINDII wind profiles shown by the symbols. The amplitude of the calculated zonal wind is also consistent with the November 26, 1992 WINDII data.

The phase and amplitude of the calculated wind profile of September 24, 2003, 1025 LT is also in good agreement with WINDII data. This comparison is shown in Figure 5.8. The WINDII instrument data here were from September 4, 1995 early afternoon (dots), November 13, 1996 late morning (stars), November, 14 1995 late morning (crosses and triangles). The two instances of zonal wind predictions (March 22, 1100 LT and September 24, 1025 , 2003) argue that the wind profiles produced by our procedure reveal the attributes of local wind profiles in the equatorial electrojet.

5.7.9 Temporal behavior

To study the behavior of the wind oscillations as a function of time, we have run the model over a span of time. We have followed identical numerical procedures as the above model runs. The temporal characteristics of the calculated zonal wind profiles for March 22 and September 24, 2003 are displayed in Figure 5.9 and Figure 5.10, respectively. Each curve in the graphs represents the specific local time shown by the legend on the right top corners of the figures. In Figure 5.9, the uppermost wind profile corresponds to 0930 LT and the lowermost to 1400 LT. In Figure 5.10, the uppermost wind profile corresponds to 0938 LT and the lowermost to 1218 LT. On both these days, the phases of the wind oscillations show a slow descent. The wind oscillations in both figures exhibit an average vertical wavelength of about 15 km. The March 22, 2003 wind profiles propagate downward about 4.5 km in about 5 hours. The September 22, 2003 wind profiles

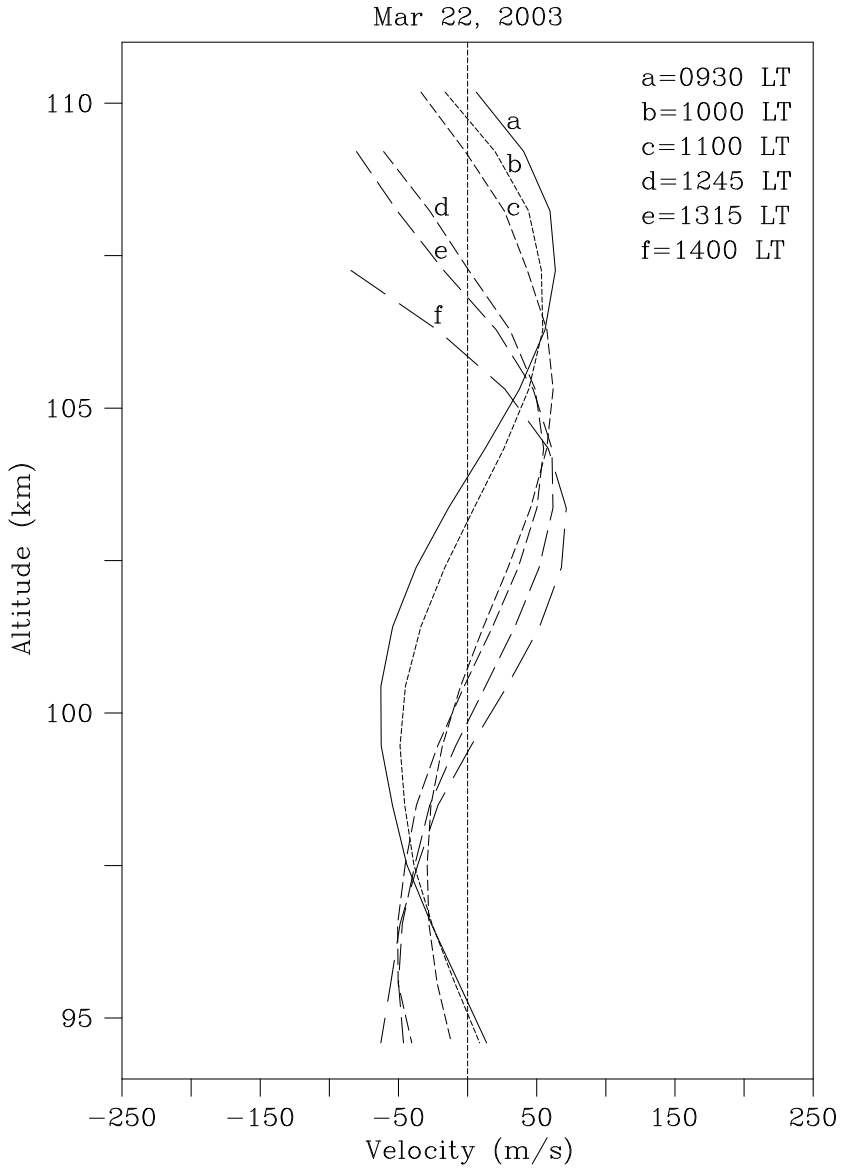

Figure 5.9: Temporal characteristics of the calculated zonal wind profiles on March 22, 2003.

propagate downward about 3 km in about 2 hours and 45 minutes. The phase of the March 22, 2003 wind makes approximately one full oscillation in about 13 hours or about two oscillations in a day. The September 22, 2003 phase shows similar

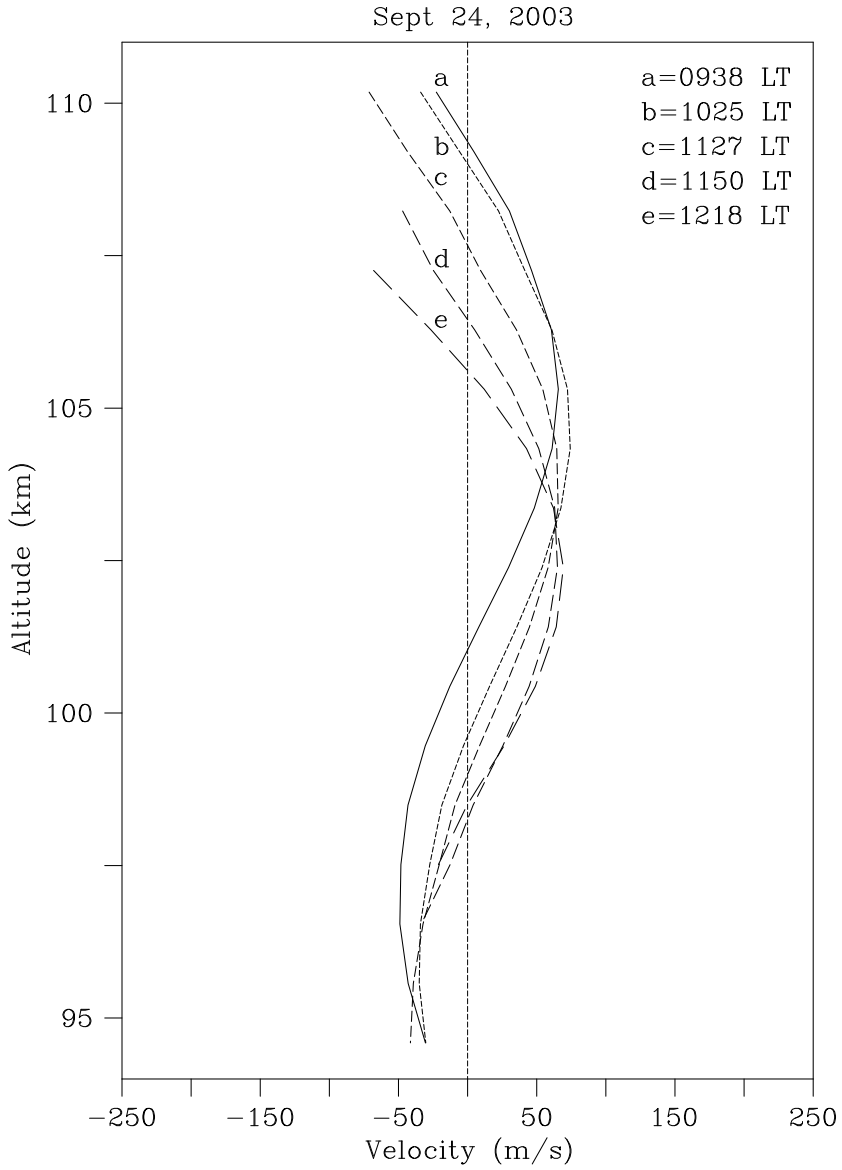

Figure 5.10: Same as Figure 5.9 but for September 24, 2003.

behavior, making one complete oscillation in about 13.5 hours. The downward phase progression of the wind oscillations is therefore nearly semidiurnal.

Using incoherent scatter ion line drift measurements at Arecibo Radio Observatory, *Harper et al* [1976] have shown eastward and southward winds to have

a downward propagation pattern with approximate periods within the range of 10 - 13 hours. *Bernard and Spizzichino* [1971] have shown wind and temperature profile data between 95 and 140 km derived from incoherent scatter radar experiment at Nancay (France) to have a dominant semidiurnal periodicity with downward phase propagation. *Bernard* [1974] has also found semi-diurnal propagating E region tidal modes using incoherent scatter radar (ISR) measurements in Saint Santin (France). The phase oscillations of the model predicted as well as the ISR measured zonal wind profiles have therefore semidiurnal period with the phase progressing downwards. However, the vertical wavelength of the winds measured by *Bernard and Spizzichino* [1971] and *Bernard* [1974] are about three times larger than the wavelength of the winds calculated by our computational procedure. On the other hand, the model wind results have the same phasing and comparable wavelength as the E region zonal wind profiles measured by rocket-born chemical release experiments conducted in the equatorial ionosphere [*Larsen*, 2002; *Larsen and Odom*, 1997], although, the rocket wind data is characterized typically by larger amplitude oscillations. The discrepancy in amplitude of the two wind estimates may lie in the inherent differences between the radar and rocket experimental techniques. The calculated wind profiles were extracted from spatially and temporally averaged Doppler velocities of type II radar echoes, whereas each point of the wind profiles measured by the rocket chemical release experiment was sampled from single spatial location instantly.

5.8 Findings summarized

Zonal wind velocity profiles in the equatorial E region are inferred by combining a three-dimensional electrostatic potential model with type II radar echoes in the

equatorial electrojet. The model predicted zonal wind velocity profiles agree well with winds measured by the WINDII instruement onboard the UARS satellite. The phases of the calculated winds progress downward with a period of about half a day which might be an indication of the semidiurnal tidal waves.

Chapter 6

Validating wind profile estimates using additional radar diagnostics

6.1 Introduction

This chapter reports on equatorial electrojet experiments conducted on July 26, 2005, at the Jicamarca Radio Observatory. Various radar experiments, namely bistatic and oblique coherent scatter radar and radar imaging experiments, were carried out concurrently to study background parameters and wave behavior. The experiments also included runs of the new AMISR -7 UHF radar system.

The Doppler shifts of type I radar echoes relative to a neutral wind frame are generally thought to saturate at the ion acoustic speed, that is, $(\frac{\omega_k}{k})_u \simeq C_s$, for a radar pointing in the direction of mean plasma flow. However, in the Earth's frame, where observations of type I radar echoes are carried out, type I Doppler shifts are expected to be shifted further by the line-of-sight projection of the neutral wind velocity.

We have not made use of the extra information imparted by type I echoes so far in this dissertation. Here, we do so in order to help validate the wind profile estimates derived from type II echoes. We also consider wave motion inferred from interferometric imaging of large-scale electrojet irregularities. At low altitudes, large scale wave velocities are mainly thought to be indicative of the local neutral winds.

6.2 Type I echoes from the Jicamarca main antenna

Figure 6.1 and Figure 6.2 show type I radar echoes observed on July 26, 2005 using the vertically looking Jicamarca main antenna. Figure 6.1 shows Doppler

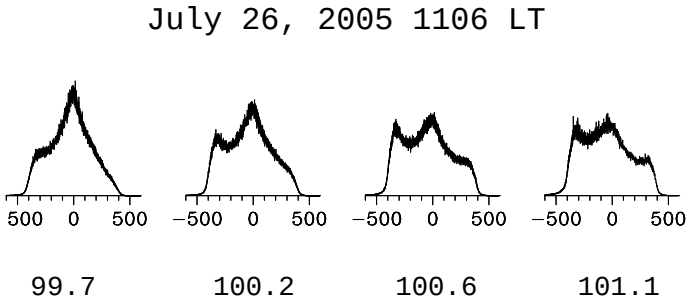

Figure 6.1: Type I radar spectra measured using the vertical main Jicamarca antenna on July 26, 2005, 1106 LT. Normalized power is plotted versus Doppler velocity in meters per second. The altitude in kilometers corresponding to each spectrum is shown below. Power is normalized by a factor of an aggregate of power in each Doppler bin.

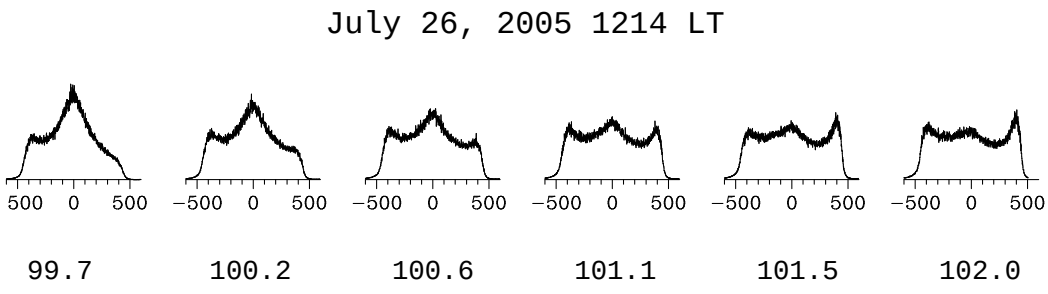

Figure 6.2: Same as Figure 6.1 but for July 26, 2005, 1214 LT.

velocities observed at 1106 LT, and the spectra in Figure 6.2 were observed at 1214

LT. The Doppler velocities of the type I echoes are about 350 m/s (Figure 6.1) and about 400 m/s (Figure 6.2).

The irregularities causing the type I echoes are generated by Farley-Buneman instabilities triggered by primary large scale gradient drift irregularities. These upward and downward propagating waves whose signatures are shown by the downshifted and upshifted spectra, respectively, in Figure 6.1 and Figure 6.2, were observed at zero zenith angle where the radar points in the flow direction of the two-stream waves. Their Doppler velocity generally saturates at the ion-acoustic speed since vertical wind speeds are generally considered to have negligible magnitude. The phase velocities 350 m/s at 1106 LT (Figure 6.1) and 400 m/s at 1214 LT (Figure 6.2) therefore correspond to the ion acoustic speeds (C_s) at the respective local times. The increase in phase velocity between the two observations indicates an increase in temperature, of which the ion acoustic speed is a function. For large zenith angles, however, the effects of zonal winds have to be taken into consideration in explaining Doppler shifts of irregularity spectra.

6.3 Theoretical estimate of type I phase velocities

Using linear theory, equations (2.44) and (2.45), assuming that the ions are strongly coupled with the neutral atmosphere in the E region, and invoking the fact that the Farley-Buneman irregularities are observed when the electron/ion relative drift speed along the radar line of sight exceeds the ion-acoustic threshold speed, the phase velocity of type I echoes for a radar pointing at a zenith angle β in the direction of electron flow, can be written mathematically as,

$$\frac{\omega_k}{k} \simeq \begin{cases} C_s + u\sin\beta, \\ C_s - u\sin\beta \end{cases} \tag{6.1}$$

where the plus and minus signs are associated with westward and eastward winds, respectively.

6.4 Zonal wind estimates

Zonal wind profiles estimated utilizing the numerical technique described in Chapter 5 are presented in Figure 6.3 with solid curves in the left half of the panels (for altitudes below about 102 km). When type II echoes are nonexistent or hard to distinguish, zonal winds can be inferred from altitudinal variations of type I radar echoes. Panels II - IV in Figure 6.3 present zonal wind estimates derived from height varying phase velocities of type I radar echoes shown with solid lines (for altitudes above about 102 km). We have employed phase velocity profiles of oblique type I echoes, equation (6.1) and the ion acoustic speeds derived from short wavelength coherent radar echoes shown in Figure 6.1 and Figure 6.2 to solve for the wind profiles, u. Actually, the dotted lines in these panels show type I phase velocity offsets from the ion acoustic speed (whose value is shown in the top right corner in each panel).

The following features of the wind profiles can be discerned from Figure 6.3: (i) a westward wind speeds of about 65 - 75 m/s around 100 km altitude, (ii) a phase reversal of the wind direction to eastward in the bottomside of the electrojet roughly coincident with reversal of direction of phase velocity of type II echoes (shown with circles with error bars) from westward to eastward (true for all panels save panel IV), and (iii) wind profiles inferred independently from type I and type II radar echoes show a fairly good continuity.

Height variations of type I echoes occurring above about 102 km altitude (dotted lines in Figure 6.3, panels II - IV) can be caused by variations in the thermo-

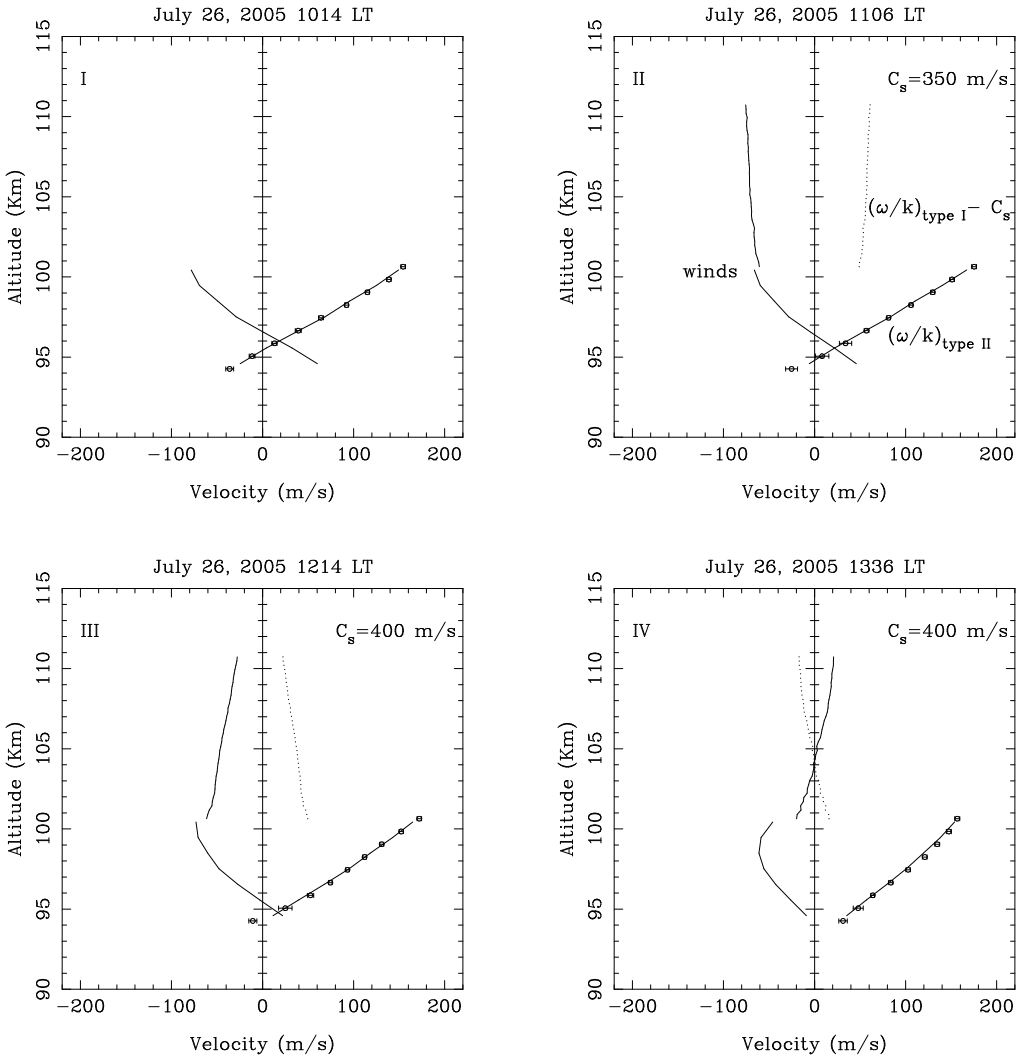

Figure 6.3: Calculated zonal wind velocity profiles (solid lines) in the equatorial E region on July 26, 2005 at 1014, 1106, 1214 and 1336 local times are shown in panel I, II, III, and IV, respectively. Circles with error bars are phase velocities of type II echoes. Solid lines plotted over them show the calculated phase velocity profiles. Offsets from the ion acoustic speed of the phase velocities of type I echoes are shown with dots.

spheric winds. Winds are thought to move the irregularities and hence can speed up (or slow down) the phase velocities of type I echoes. The wind profiles shown in Figure 6.1, panels II - IV, were extracted from the movement of the irregularities. The merger between the wind profiles derived from type II echoes and the ones derived from type I echoes support the validity of the techniques used.

6.5 Oblique type I radar echoes

Figure 6.4 and Figure 6.5 show the Doppler velocities of type I echoes observed by the oblique looking radar at Jicamarca on July 26, 2005. The figures correspond to 1106 and 1214 LT, respectively. The corresponding velocities for the two sets of spectra are about 400 m/s and 450 m/s, respectively. We have made use of these velocity measurements along with wind estimates shown in Figure 6.3, type I echoes in Figure 6.1 and Figure 6.2, and equation (6.1) to gain physical insights into the Doppler shift characteristics of oblique type I radar echoes.

Given $C_s = 350$ m/s from Figure 6.1, a westward wind of $u \approx 65$ m/s for 1106 LT from Figure 6.3 around the altitude region 100±1 km (panel II), and taking $\beta = 53.8°$ for the oblique antenna at Jicamarca, the phase velocity (6.1) becomes $\frac{\omega_k}{k} = 400$ m/s in agreement with the observed phase velocity shown in Figure 6.4. Likewise at 1214 LT, for a westward wind of $u \approx 70$ m/s around the altitude region 100±1 km (Figure 6.3, panel III) and C_s= 400 m/s (Figure 6.2), the phase velocity (6.1) becomes $\frac{\omega_k}{k} = 450$ m/s in agreement with Figure 6.5. Therefore, the presence of a westward wind evidently explains the Doppler shifts of type I oblique echoes observed at large zenith angle (Figure 6.4 and Figure 6.5).

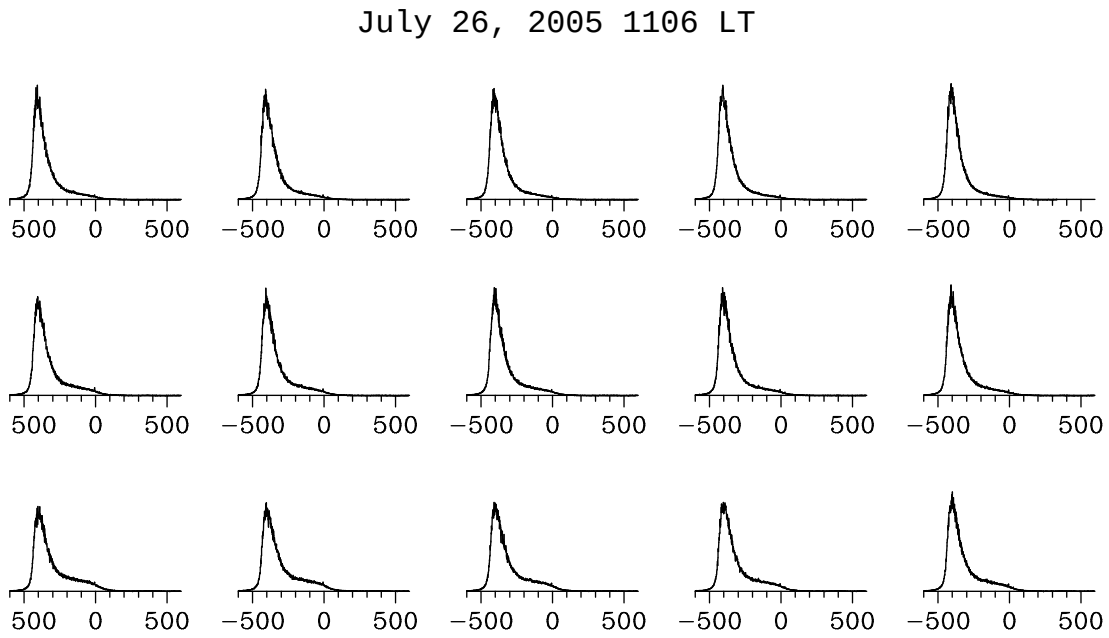

Figure 6.4: Type I radar spectra measured using the oblique coherent scatter radar at Jicamarca on July 26, 2005, 1106 LT. Normalized power is plotted versus Doppler velocity in meters per second. The bottom left spectrum correspond to 99.0 km altitude and the top right spectrum correspond to 102.8 km. The separation between two consecutive spectra is about 250 meters. Power is normalized by a factor of an aggregate of power in each Doppler bin.

6.6 Wind profiles inferred from propagation properties of large-scale electrojet turbulence at low altitudes

Linear theory for large scale irregularities, equation (2.48), indicates that phase velocities of large scale electrojet irregularities depend on the strength of the electric field and background parameters. In the lower electrojet below about 98 km altitude, the motion of drifting electrons is inhibited by ion neutral collisions.

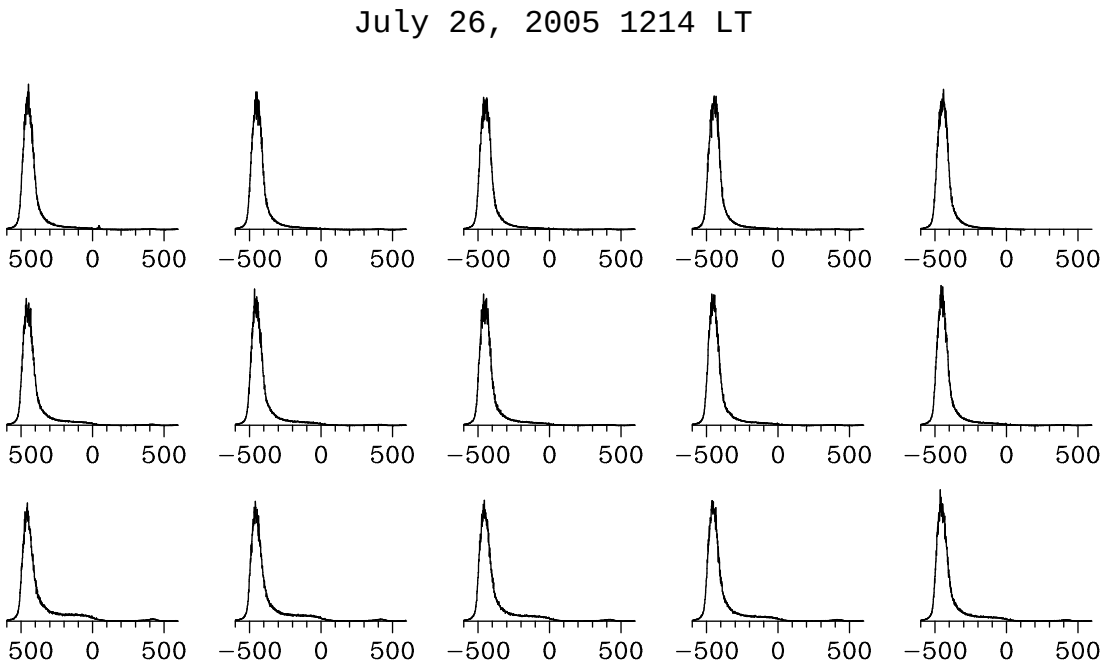

Figure 6.5: Same as Figure 6.4 but for July 26, 2005, 1214 LT.

In addition, at those altitudes, electron collision frequencies might not be much smaller compared to electron gyro frequencies. These lead to diminishing phase velocities of the normally westward propagating large scale irregularities. Actually, the large scale wave phase velocities are at times found to reverse to eastward in the bottomside, as shown by radar interferometric experiments at Jicamarca. This is illustrated in Figure 6.6 (a movie of the propagating large scale waves clearly shows this). The eastward propagation of the waves observed in the bottomside must be due to the presence of eastward winds at those altitudes. The reversal, to eastward, of the calculated wind profiles (Figure 6.3, panels I - III) in the lower electrojet is therefore supported by the presence of the eastward large scale waves.

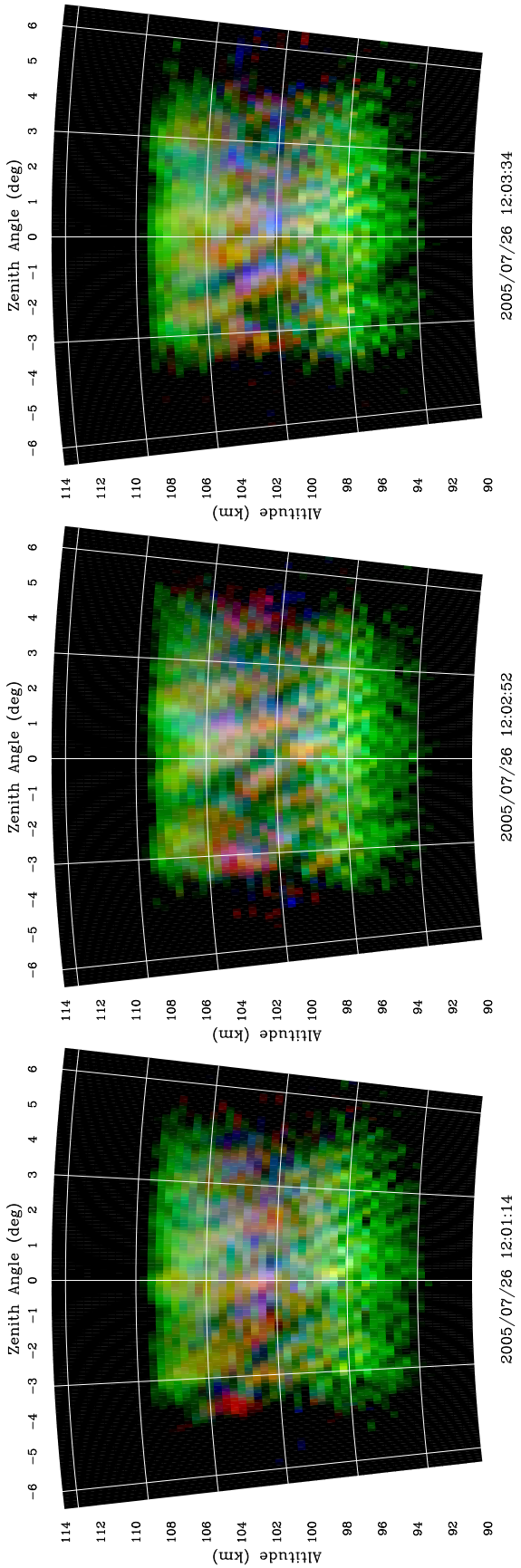

Figure 6.6: Images of large scale irregularities in the equatorial electrojet on July 26, 2005, 1201 LT to 1203 LT.

Chapter 7

Conclusion and Future work

An electrostatic potential model has been combined with coherent/incoherent scatter radar measurements to study the equatorial electrojet region, the region where an intense zonal current excites a broadband spectrum (ranging from meter scales to kilometers) of field aligned plasma irregularities. Accordingly, this final chapter presents (i) summaries of major research findings reported in the dissertation, and (ii) future research plans.

7.1 Conclusion

1. We have reported equatorial E region electron density profiles measured with a new bistatic coherent radar system operating between Jicamarca (transmitter) and Paracas (receiver), Peru. We have utilized the quasi-longitudinal approximation of radio wave propagation in a cold magnetoplasma, which functionally relates electron density and Faraday rotation of the coherently scattered signal. Electron density profiles are constructed by numerically differentiating the Faraday angle with respect to altitude. The radar estimated electron density profiles agree well with (i) electron density profile derived from the α Chapman function, and (ii) density profiles measured *in situ* by rocket flight experiments. The peak measured electron densities are in good agreement with the IRI-2001 peak electron density estimates. The measured peak densities are also in good agreement with the peak electron denisities measured by the Jicamarca Digisonde Portable Sounder (DPS-4). However, it is worth mentioning that the measured and IRI profiles depart

drastically below the E region peak. The latter which represented by a mathematical function overestimates electron density profiles below the E region peak. Electron density data are available only at altitudes and local times when strong plasma irregularities are present, limiting their usefulness in certain kinds of statistical studies and making then unsuitable, for instance, for tracking the E region peak altitude over time. The bistatic system is now permanently installed at Jicamarca and Paracas for continuously monitoring electron density profiles in the equatorial electrojet region. The E region electron density profiles are being deposited in the CEDAR database for use by the space geophysics community.

2. We have reported on zonal wind profiles in the equatorial electrojet region in the South American sector extracted from Doppler radar measurements of type II echoes from the obliquely looking radar at the Jicamarca Radio Observatory. Zonal wind profiles are retrieved by combining a three-dimensional electrostatic potential model with predictions and measurements of type II echoes in the equatorial electrojet. The conventional electron collision frequency was modified to incorporate anomalous collision effects. Our model calculations are consistent with magnetometer and vertical plasma drift data measured by the incoherent scatter radar at the Jicamarca Radio Observatory. We sought wind profiles which brings the measured and calculated phase velocities of type II echoes to closer agreement. Accordingly, a comparative iterative procedure has been employed. The magnitude and phasing of the calculated zonal wind velocity profiles agree well with winds measured by the WINDII instrument onboard the UARS (Upper Atmosphere Research Satellite). It is evident from the temporal properties of the calculated wind

that the phase progresses downward with a period of about half a day which might be a signature of the semidiurnal tide. The downward phase progression of the zonal winds appear to influence the electrodynamics of the local plasma by modulating the magnitude and direction of the polarization electric fields through a dynamo mechanism. Concurrent bistatic and oblique coherent scatter radar experiments would be conducted at Jicamarca to investigate the influences of the downward phase progression of the winds might have on the E region plasma density profiles and plasma instabilities. The amplitude and phase of the calculated zonal wind profiles are in general agreement with representative wind profiles measured by the WINDII instrument onboard the Upper Atmosphere Research Satellite (UARS). The calculated winds also have the same general characteristics as zonal wind profiles measured by rocket-borne chemical release experiments. However, the magnitude of the latter are larger than the former. The temporal behavior of the calculated zonal winds suggests a downward phase progression with a roughly semidiurnal period.

7.2 Future work

We plan to pursue the following research areas pertinent to the equatorial ionosphere: (i) the pre-reversal enhancement of the zonal electric field in the equatorial ionosphere. (ii) Plasma flow characteristics of the topside equatorial F region during spread F conditions.

7.2.1 Pre-reversal enhancement of the zonal electric field in the equatorial ionosphere

Introduction

During early evening hours, the low altitude plasma in the equatorial ionosphere is lifted up to higher altitudes [*Woodman*, 1970; *Fejer*, 1981]. The plasma uplift is due to enhancement of the zonal electric field. Theories put forward by various researchers for explaining the observed electric field enhancement have been reviewed in Chapter 2. To summarize them: (i) *Farley et al* [1986] explained the enhancement of the zonal field in terms of electric fields mapped back from the magnetically connected off equatorial ionosphere to the F region, (ii) *Haerendel and Eccles* [1992] explained it in terms of the divergence of the equatorial electrojet during the evening due to conductivity reduction and the vertical current demanded by the F region, and (iii) *Eccles* [1998a, b] explained it in terms of the edge effect of the vertical polarization electric field formed during the evening and morning hours.

Here we will analyze the behavior of the divergence free current equation to study electric field enhancements near the solar terminators. For that purpose, equation (5.31) is rewritten as,

$$\begin{aligned} -\frac{\partial}{\partial\phi}\left(h_p h_q \sigma_P E_\phi\right) + \frac{\partial}{\partial p}\left(h_\phi h_q \sigma_H E_\phi\right) &= \frac{\partial}{\partial\phi}\left(h_p h_q[\sigma_H(E_p + uB) + \sigma_P E_\circ]\right) \\ &+ \frac{\partial}{\partial p}\left(h_\phi h_q[\sigma_P(E_p + uB) - \sigma_H E_\circ]\right) \\ &+ \frac{\partial}{\partial q}\left(h_p h_\phi \sigma_\circ E_\parallel\right) \end{aligned} \tag{7.1}$$

where $E_\circ = |\mathbf{E}_\circ|$, $E_\parallel = |\mathbf{E}_\parallel|$, and pressure and gravity driven currents are ignored for the simplicity.

Let us consider the various terms in the right hand side of (7.1) to analyze their contribution to the variations of the Pedersen and Hall currents driven by the zonal polarization field E_ϕ.

Case 1: Divergence of zonal current

When the zonal current driven by the vertical polarization field and the background electric fields diverge, a need arises for a zonal polarization electric field to keep the current flowing and maintain quasineutrality,

$$-\frac{\partial}{\partial\phi}\left(h_p h_q \sigma_P E_\phi^I\right) + \frac{\partial}{\partial p}\left(h_\phi h_q \sigma_H E_\phi^I\right) = \frac{\partial}{\partial\phi}\left(h_p h_q [\sigma_H (E_p + uB) + \sigma_P E_\circ]\right) \quad (7.2)$$

Due to a reduction in the content of conductivities, the right hand side diverges drastically around the solar terminator. In such circumstances, the zonal electric field E_ϕ^I needs to be enhanced while approaching the terminator where σ_P and σ_H are significantly diminished. In the E region, divergences of both $\sigma_H(E_p + uB)$ and $\sigma_P E_\circ$ contribute to the process. According to the second term in the right hand side of (7.2), the zonal field drives a vertical Hall current out of the E region to further reduce the conductivity there. The feedback is to further speed up plasma uplift from the E region. This result was found by *Haerendel and Eccles* [1992].

In the F region, (7.2) might take the approximate form,

$$-\frac{\partial}{\partial\phi}\left(h_p h_q \sigma_P E_\phi^I\right) = \frac{\partial}{\partial\phi}\left(h_p h_q \sigma_P E_\circ\right) \quad (7.3)$$

This due to the fact that Pedersen current flows in the F region but Hall current is confined in the E region. Integrating (7.3) in a longitudinal sector ranging from ϕ_1 to ϕ_2 well before the terminator and in the terminator, respectively,

$$\sigma_P(\phi_2)(E_\phi(\phi_2) + E_\circ(\phi_2)) = \sigma_P(\phi_1)(E_\phi(\phi_1) + E_\circ(\phi_1)) \quad (7.4)$$

where the variation of the scale factors is ignored for simplicity. They will not be, however, ignored in actual numerical calculations.

Obviously, the conductivity $\sigma_P(\phi_2)$ is much smaller than $\sigma_P(\phi_1)$. Therefore, by a similar argument as above, there arises a demand for a significant increase in the zonal field $E_\phi^I + E_\circ$ at ϕ_2 compared to $E_\phi^I + E_\circ$ at ϕ_1.

Case 2: Divergence of vertical current

The evening plasma uplift might also be described in terms of divergence of vertical E and F region currents,

$$-\frac{\partial}{\partial\phi}\left(h_p h_q \sigma_P E_\phi^{II}\right) + \frac{\partial}{\partial p}\left(h_\phi h_q \sigma_H E_\phi^{II}\right) = \frac{\partial}{\partial p}\left(h_\phi h_q[\sigma_P(E_p + uB) - \sigma_H E_\circ]\right) \quad (7.5)$$

If the vertically diverging vertical current is also diverging zonally, which is likely true around the terminator, the zonal field E_ϕ^{II} adjusts such that the overall current remains solenoidal.

In the F region, (7.5) might reduce to,

$$-\frac{\partial}{\partial\phi}\left(h_p h_q \sigma_P E_\phi^{II}\right) = \frac{\partial}{\partial p}\left(h_\phi h_q \sigma_P (E_p + uB)\right) \quad (7.6)$$

Vertical Pedersen current decays during evening hours due to cancelation by the F region dynamo, leading to the horizontal divergence just mentioned,

$$\left(-h_p h_q \sigma_P E_\phi^{II}\right)(\phi_2) + \left(h_p h_q \sigma_P E_\phi^{II}\right)(\phi_1) = \int_{\phi_1}^{\phi_2} \frac{\partial}{\partial p}\left(h_\phi h_q \sigma_P (E_p + uB)\right) d\phi \quad (7.7)$$

The field E_ϕ^{II} at ϕ_2 should be larger than at ϕ_1 since the integrand in (7.7) is larger at ϕ_1 than at ϕ_2 .

Case 3: Divergence of parallel current

Divergence of parallel current might also contribute to zonal field enhancement according to the last term in (7.1),

$$-\frac{\partial}{\partial\phi}\left(h_p h_q \sigma_P E_\phi^{III}\right) + \frac{\partial}{\partial p}\left(h_\phi h_q \sigma_H E_\phi^{III}\right) = \frac{\partial}{\partial q}\left(h_p h_\phi \sigma_\circ E_\parallel\right) \tag{7.8}$$

Specific plan

The plan in this regard is therefore to assess the relative importance of the mechanisms mentioned above for enhancement of the equatorial zonal electric field using realistic ionospheric modeling. These efforts would help us to establish the dominant physical mechanism or the relative contributions of the various factors for the field enhancement.

7.2.2 Spectral analysis of flow characteristics of the topside equatorial *F* region plasma

Results of spectral analysis of electric field fluctuation data from the AE-E (Atmospheric Explorer -E) satellite have been reported by *Shume and Hysell* [2004]. The manuscript is attached in Appendix A of the dissertation. The findings can be summarized as follows.

Plasma drift data from the AE-E satellite were spectrally analyzed to investigate the characteristics of the flow in the topside equatorial F region ionosphere during strong spread F conditions. Plasma flow around rapidly rising depletions is thought to exhibit behavior similar to two-dimensional Kolmogorov turbulence, but only on flux tubes with sufficiently small integrated ion-neutral collision frequencies. We found that one-dimensional spectra computed from vertical plasma

drift measurements made in such depletions on such flux tubes tend to display a -5/3 spectral index over scale sizes from about 1–100 km, suggesting the operation of an inverse energy cascade. This universal spectral form is evidence of an inertial regime of the underlying ionospheric interchange instability. Analytical and numerical magnetic flux tube integrated modeling were used to identify the local times and flux tubes where inertial effects are most likely to be important in equatorial spread F flows and were used determine the threshold convection speeds necessary.

Plasma drift data were taken from the Ion Drift Meter (IDM) onboard AE-E satellite. The IDM measured cross-track drifts in the vertical and horizontal directions. However, the drift measurements were sequential rather than simultaneous. Vector cross-track drift estimates therefore were not be obtained. In the spectral analysis mentioned above, we made use only of the vertical drift measurements and made the assumption that these drifts are dominated by perpendicular plasma drifts.

The nonuniform sampling of the vertical drift measurements due to coordinate switching was compounded by numerous dropouts in the data stream from the instrument. Due to this the AE-E plasma drift data were not ideal for spectral analysis purposes. Therefore, the conclusions made, based on the Lomb periodogram technique, about the spectral behavior of plasma drifts were tentative. To make definitive conclusions, we need to investigate the flow characteristics by looking into more data.

In the future, we will seek to obtain additional data from other satellites to expand the turbulence spectral analysis. In particular, spectral analysis would be conducted utilizing the ROCSAT-1 satellite's (Republic of China Satellite) equato-

rial plasma density and electric field fluctuation data. The ROCSAT-1 spacecraft is a low inclination (35°) circular orbit at about 600 km altitude and thus provides complete coverage in local time of the low latitude about every 90 minutes. Its IPEI (Ionospheric Plasma Electrodynamic Instrument) payload consists of four sensors that measure the ion number density, velocity vector, temperatures, and composition [*Yeh et al*, 2001]. We will also seek plasma density and drift data to perform spectral analysis from the upcoming low latitude satellite mission, C/NOFS (Communication/Navigation Outage Forecast System).

Appendix A

Spectral analysis of plasma drift measurements from the *AE-E* (Atmospheric Explorer - E) satellite: evidence of an inertial subrange in equatorial spread *F*

A.1 Introduction

While the cause of plasma irregularities associated with equatorial spread F (ESF) events was once controversial, it is now known that ionospheric interchange instabilities are responsible [*Woodman and La Hoz*, 1976]. The irregularities emerge first in the bottomside of the F region where ion-neutral collisions are frequent and where a balance between Pedersen currents and currents driven by gravity determines the dynamics of the instability; this is the collisional flow regime. The collisional regime has been shown to produce laminar flows in which the dominant nonlinear effect is plasma steepening [*Scannapieco and Ossakow*, 1976; *Costa and Kelley*, 1978; *Zargham and Seyler*, 1987; *Hysell et al.*, 1994b]. However, the action of the instability is such that depleted regions of plasma are convected rapidly upward, past the F peak and into the topside ionosphere where ion-neutral collisions are less frequent. It has been postulated that, at sufficiently high altitudes, polarization currents associated with ion inertia and strong convection may come into play and compete with or even dominate Pedersen currents in balanc-

ing currents driven by gravity and preserving quasineutrality in the vicinity of the rising depletions [*Ott*, 1978; *Kelley and Ott*, 1978]. If so, then the dynamics of the flow (in the so-called "inertial regime") might be expected to assume a turbulent state reminiscent of two-dimensional Navier Stokes turbulence [*Kintner and Seyler*, 1985; *Hassam et al.*, 1986; *Zargham and Seyler*, 1989]. In this case, the dominant nonlinear effect might be expected to be turbulent cascades leading to inertial range spectra. This effect could have important implications for radio scintillations caused by ESF since the irregularity spectra for collisional and inertial regime flows would differ [*Zargham and Seyler*, 1989]. However, experimental evidence for inertial regime flows in spread F is inconclusive. In the only experiment explicitly addressing the issue, *Jahn and LaBelle* [1998] found no evidence of inertial range spectra in data taken from a sounding rocket encounter with a spread F plume in project Guará. Conversely, Alfven wave signatures detected by *Aggson et al.* [1992] in a San Marco satellite encounter with ESF irregularities argues strongly for the importance of polarization currents in some ESF events.

This paper is the third in a series that argues that inertial regime flows can exist in fully-developed ESF. In the first, *McDaniel and Hysell* [1997] solved analytically and self-consistently for the flow around a rising depleted flux tube of circular cross-section in a realistic ionosphere. They found a window of local times and apex heights for which the depletion should rise sufficiently rapidly for polarization currents to become comparable in magnitude to Pedersen currents in the tube's vicinity. However, this only happened if the tube was deeply depleted. The irregularities seen by *Jahn and LaBelle* [1998] were neither deeply depleted nor rapidly moving, and it may therefore have been that the convection was too weak to excite inertial effects in that case. *McDaniel and Hysell* [1997] went on to

compute the power spectra of intense density irregularities observed by the DE-II spacecraft during ESF over many orbits and found that data corresponding to the prescribed window exhibited universal $k^{-5/3}$ one-dimensional power spectra for scale sizes greater than about 1 km, suggesting the existence of an inverse energy cascade. Expanding upon the idea, *McDaniel* [1998] used wavelet analysis and localized the regions of irregularities with -5/3 spectral indices to those with large amplitudes.

In the second paper in the series, *Hysell and Shume* [2002a] performed a theoretical analysis of the inertial interchange instability in a plasma. The necessity for the plasma to be inhomogeneous for inertial effects to be important means that the resulting flow must be essentially different from Navier Stokes turbulence, which occurs in homogeneous fluid flows. Nevertheless, *Hysell and Shume* [2002a] showed that an inverse energy cascade characterized by one-dimensional velocity spectra scaling as $k^{-5/3}$, still occurs in the inhomogeneous system. Similar results had been obtained earlier by *Zargham* [1988].

In this paper, we seek further evidence for inertial regime effects, plasma turbulence, and inertial range spectra in equatorial spread *F*. We use plasma drift data taken by ion drift meter (IDM) on the AE-E satellite. As predictions of inertial range spectra obeying specific scaling laws apply strictly to velocity spectra, these data should be more direct telltales of plasma turbulence than the DE II plasma density data examined previously. Furthermore, by working with drift measurements, we can assess how strongly driven the plasma flow is directly rather than relying on model predictions based on idealized flow geometries, as was done by *McDaniel and Hysell* [1997].

A.2 Data Presentation

We analyzed data from the AE-E satellite taken between 1978 and 1980 when the satellite had a nearly circular orbit with a mean altitude that varied between about 325 km and 450 km at different times in that interval. Because of its 19.7° inclination, the satellite probed magnetic flux tubes with a broad range of magnetic apex heights. Out of the entire AE-E data archive we identified approximately 35 distinct ESF events with deep density depletions (99% or more) and with velocity fluctuations suggesting active instabilities for our study. All longitudes were considered, but most of the data correspond to the Atlantic sector.

Plasma density and drift data were taken from the ion drift meter (IDM) [*Hanson and Heelis*, 1975]. The sample rates for densities and drift measurements are 16 and 32 Hz, implying a spatial resolution of about 480 and 240 m, respectively. The IDM measured cross-track drifts in the vertical and horizontal directions. However, the drift measurements were sequential rather than simultaneous, with one Cartesian component being sampled at a time for intervals of either 2/3 or 4 s. Vector cross-track drift estimates therefore cannot be obtained. For our studies, we made use only of the vertical drift measurements and made the assumption that these drifts are dominated by perpendicular plasma drifts ($\mathbf{E} \times \mathbf{B}$ drifts), a reasonable assumptions at small dip latitudes and a necessary one in any case.

The nonuniform sampling of the vertical drift measurements due to coordinate switching is compounded by numerous dropouts in the data stream from the instrument. In order to spectrally analyze the drift data, we utilized the Lomb periodogram technique, which can be viewed as a least-squares fit of harmonic basis functions (sinusoids) to the available data [*Lomb*, 1976]. While being computationally expedient, this technique is not a signal processing panacea; when applied

to our data, the algorithm has a tendency to produce spectral artifacts (spurs) at harmonics of the switching period. However, the predictability of the spurs in question makes them readily identifiable and excisable. We detrended the vertical drift data and then computed sliding window Lomb periodograms from them. The width of the sliding window was typically 256 s wide, a time span comparable to the eddy turnover time for the smallest scale features of interest in the flow under study and therefore small enough to satisfy the stationarity requirements for spectral estimation. The spectra of velocity fluctuations that resulted generally exhibited power law scaling from an outer scale of about 100 km to an inner scale of a few km, where the instrument noise floor caused the spectra to become flat. The slopes of the spectra in this scale size regime were determined through least-squares fitting.

Based on the analysis of *McDaniel and Hysell* [1997], we expect inertial effects to be most important for about an hour after sunset when the equatorial ionosphere is at its highest and on flux tubes with apex points above the F peak but not so high that the anomaly crests contribute significantly to the integrated Pedersen conductivity. In the 35 data sets we chose, there turn out to be only half dozen instances when the satellite passed through intense ESF irregularities within this approximate window of magnetic apex heights ($\sim$600–900 km) and local times ($\sim$20–21 LT). Three of the half dozen instances we identified are shown in Figures 1 through 3. The top and second panels of each present plasma density and ion drift measurements recorded by the spacecraft during its passage through spread F events. The continuous line in the latter is a smoothed curve intended as a rough proxy for a true zero, taking into account satellite pointing errors that can bias the drift velocity estimate. Spectrograms calculated with a sliding window Lomb

periodogram are depicted in the third panel. The fourth panel shows the slope of each spectrum in the range of scale sizes between about 1–100 km, determined with a Levenberg Marquardt fitting technique. Overall, the slopes for all the AE-E drift data generally fall between -1 and -3 and can vary rapidly and erratically in time.

As revealed in the fourth panels in each figure, however, the spectral index tends to gravitate toward values close to -5/3 (broken line) (within the range -5/3 $\pm$0.05) when the density irregularities are intense, the velocity fluctuations are significant, and when the satellite was in or near the window of local times and magnetic apex heights prescribed above. This trend is evident in all of the applicable datasets we examined. Below, we quantify the condition for inertial regime flow the ionosphere more precisely and argue that the AE-E dataset, limited as it is, offers tentative evidence that such a flow can exist in topside spread F.

A.3 Analysis

McDaniel and Hysell [1997] analyzed the plasma flow around rising, completely depleted flux tubes of circular cross section. The considered background currents due to gravity and the background electric field along with the resulting Pedersen currents driven by polarization charges accumulating on the depletion walls and polarization currents associated with irregular plasma flow around the rising depletions. Quasineutrality imposed the requirement that these currents be balanced so that:

$$\begin{aligned} \int dl \frac{n g_\perp}{\Omega_i} \frac{h}{h_\circ} &= \left(V_\circ - \frac{E_\circ}{B_\circ} \right) \int dl \frac{n \nu_{\rm in}}{\Omega_i} \frac{B_\circ}{B} \\ &+ 4 \frac{V_\circ^2}{R_\circ} \int dl \frac{n}{\Omega_i} \frac{B_\circ}{B} \end{aligned} \tag{A.1}$$

in which the first, second, and third terms correspond to currents driven by gravity, Pedersen currents, and polarization currents, respectively. Here, h is the scale factor for the longitude coordinate, $g_\perp$ is the component of gravity perpendicular to the geomagnetic field B, $V_\circ$ is the depletion convection speed, E is the background zonal electric field, $R_\circ$ is the radius of the depletion, and where the other terms have their usual meaning. A zero subscript designates values evaluated at the magnetic dip equator, and the integration is over a magnetic flux tube. This integration represents the application of Kirchhoff's law to the summation of transverse current components; magnetic field lines are treated as equipotentials. To incorporate the effects of multiple ion species, (A.1) can be generalized with $\nu_{\rm in}/\Omega_i \rightarrow \sum_j f_j \nu_{{\rm in},j}/\Omega_{ij}$ and $1/\Omega_i \rightarrow \sum_j f_j/\Omega_{ij}$, where f_j is the ion fraction for species j.

McDaniel and Hysell [1997] evaluated the integrals in (A.1) numerically, deriving plasma densities from the PIM model [*Peddie and Fabiano*, 1982], magnetic fields from the IGRF model [*Barton*, 1997], composition from IRI [*Bilitza et al*, 1993], background electric fields from curves published by *Fejer et al.* [1995], and temperatures necessary for computing collision frequencies according to formulas given by *Schunk and Walker* [1973] from MSIS90 [*Hedin*, 1991]. They solved the quadratic to predict depletion rise velocities $V_\circ$ for different background conditions and then, with that knowledge, compared the magnitudes of the second and third terms in (A.1) to assess the relative importance of ion inertia (polarization currents). They determined that depletions can be expected to rise as fast as 200–400 m/s at times just after sunset and on flux tubes with apex heights of about 600-900 km. In such events, polarization currents should be comparable to or slightly larger than Pedersen currents in the vicinity of the depletions. Plasma turbulence may then occur. It is important to note that plasma convection speeds

well in excess of 400 m/s are known to arise in narrow, elongated, depleted channels feeding low-density plasma into the topside. Convection speeds much greater than 1000 m/s have been observed in satellite datasets [*Aggson et al.*, 1992] and in radar observations in the "neck" of particularly intense radar plumes [*Hysell et al.*, 1994a]. However, the flow is laminar rather than turbulent in such cases, however, and inertial effects are unlikely to be important in such cases. The overwhelming majority of plasma depletions seen in the AE-E dataset have convection speeds less than about 400 m/s.

Having access to velocity data for the current study, we will skip the first of these steps. We will evaluate the terms on the right side of (A.1) numerically, equate them, and solve for the depletion convection speed $V_\circ$ for which polarization currents are as significant as Pedersen currents. This can be interpreted as an estimate of the threshold speed for plasma turbulence to set in. Neglecting $E_\circ/B_\circ$ by comparison to $V_\circ$, this threshold speed takes the simple, intuitive form:

$$V_\circ \approx \frac{1}{4} R_\circ \langle \nu_{\rm in} \rangle \tag{A.2}$$

where the averaging implied in (A.2) is determined by the integral forms in (A.1). The larger the flux-tube integrated collision frequency, the larger the threshold convection speed. The larger the radius of curvature of the depletion, the larger the threshold speed. The factor of 4 in (A.2) applies to circular depletions and will differ for different configurations.

We have evaluated the "threshold" convection speed $V_\circ$ according to (A.1) for conditions relevant to our AE-E data, retaining and estimating the background electric field from the model produced by *Scherliess and Fejer* [1999]. We interpret $R_\circ$ as the radius of curvature of the plasma flow, not just in excursions around a rising depletion, but in any eddy in the flow. The radius of an eddy if half its

diameter which is half again the scale size associated with and eddy in spectral analysis; since the outer scale of the flows we examined were typically no more than 100 km, we therefore set $R_\circ = 25$ km. The curves that result should be taken as rough indications of when and on what flux tubes inertial effects are most likely to be important in spread F events.

The results of the subsequent calculations are shown in Figure A.1 through Figure A.3. Figure A.1 was computed for conditions corresponding to the data in Figure A.4 and imply that inertial effects will be significant in the window of local times between about 19.5 and 21 LT and magnetic apex heights between about 600 and 900 km given the presence of convection speeds approaching 300 m/s. By significant, we mean that Pedersen and polarization currents in the vicinity of the depletions will have comparable magnitudes. The first four groups of deep depletions evident in Figure A.4 meet the criteria and, indeed, exhibit a -5/3 spectral index in their drifts. The event in Figure A.4 is unique in that it is predicted to fall almost entirely within the inertial regime. This is not the case for the data shown in Figure A.5. For this event, which is more typical of what we find in the AE-E database, the satellite just grazed but not cut through the most favorable contours in Figure A.2 with only the earliest two patches of irregularities having sufficient convection speeds for inertial effects to have any likelihood of being significant. As predicted, however, it is only these irregularities which exhibit a -5/3 spectral index in their one-dimensional velocity spectra. By favorable, we mean inertial flows are facilitated by the traits: early evening hours in a range of 19:00 - 21:00 LT hours, 600-900km apex height and plasma convection speed of about 200 - 400 m/s be all met for inverse cascade. The same can be said of the observation in Figure A.6. This time too, the satellite merely grazed

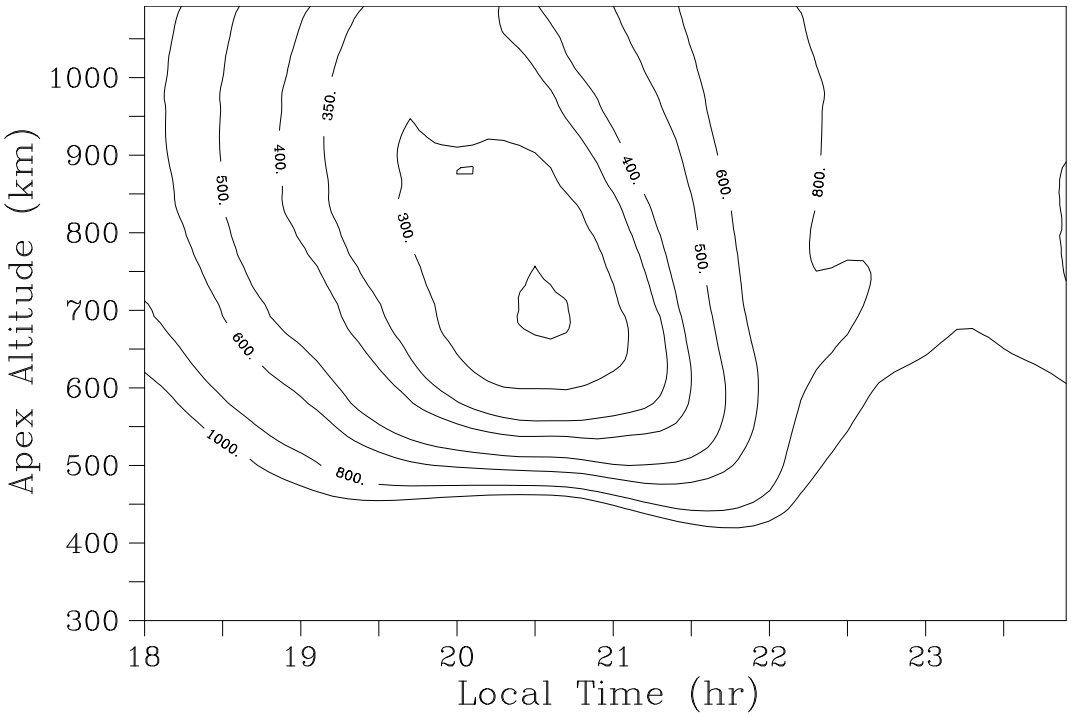

Figure A.1: Model run for February 25, 1978. Contours denote the velocity threshold arising from equating the last two terms in equation 1 (see text).

the most favorable contours in Figure A.3. Only the earliest patch of irregularities meet the criteria for significant polarization currents to be present, and only these irregularities diplay a spectral index close to -5/3. These three datasets, drawn from a pool of a half-dozen comparable ones, constitute tentative but compelling evidence for an inertial regime in equatorial spread F.

A.4 Summary and Conclusions

Using analytic and numerical modeling, we identified the local times and flux tubes where inertial effects are most likely to be important in equatorial spread F

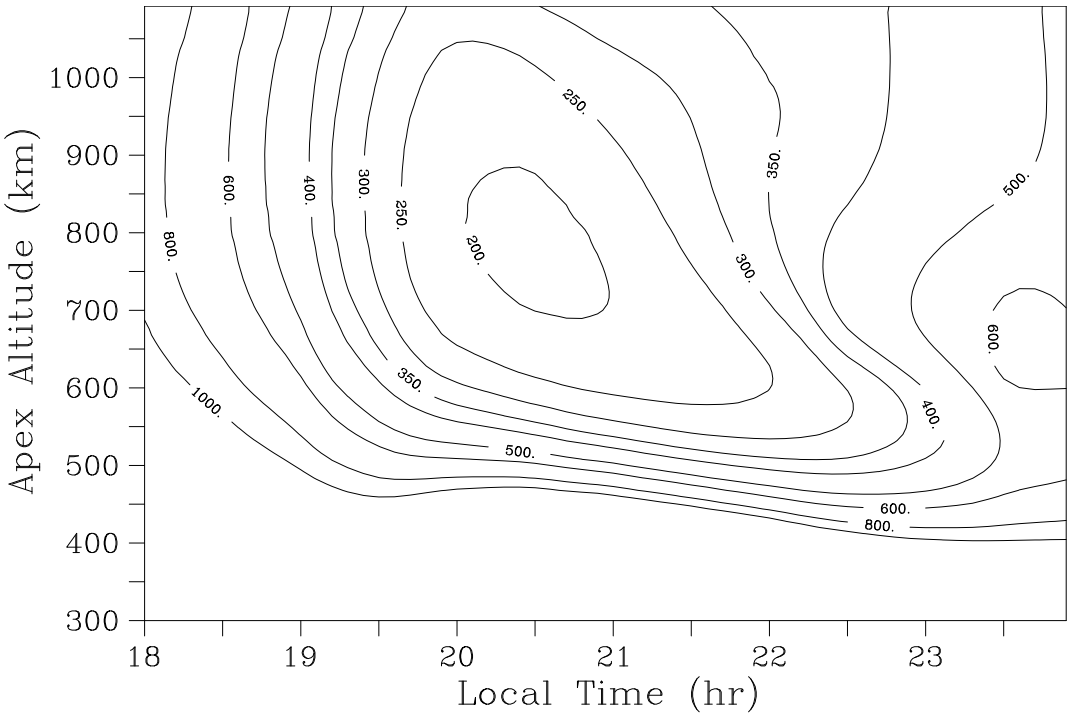

Figure A.2: Model run for January 29, 1979. Contours denote the velocity threshold arising from equating the last two terms in equation 1 (see text).

flows and determined the threshold convection speeds necessary. We then searched the AE-E satellite database for candidate plasma irregularities. Only a very few candidates could be found. This is not because inertial regime flows are necessarily rare in the equatorial ionosphere but more due to idiosyncrasies in the orbit and data collection schedule of the satellite. Nevertheless, the few datasets selected had velocity spectral indices close to -5/3 in the regions thought to be most prone to inertial effects. This spectral index is telltale of an inverse cascade of energy from intermediate scale sizes to long, similar to what occurs in two-dimensional Navier Stokes turbulence in homogeneous neutral fluids. The implication is that plasma flows in strongly-driven topside spread F occurring shortly after sunset should

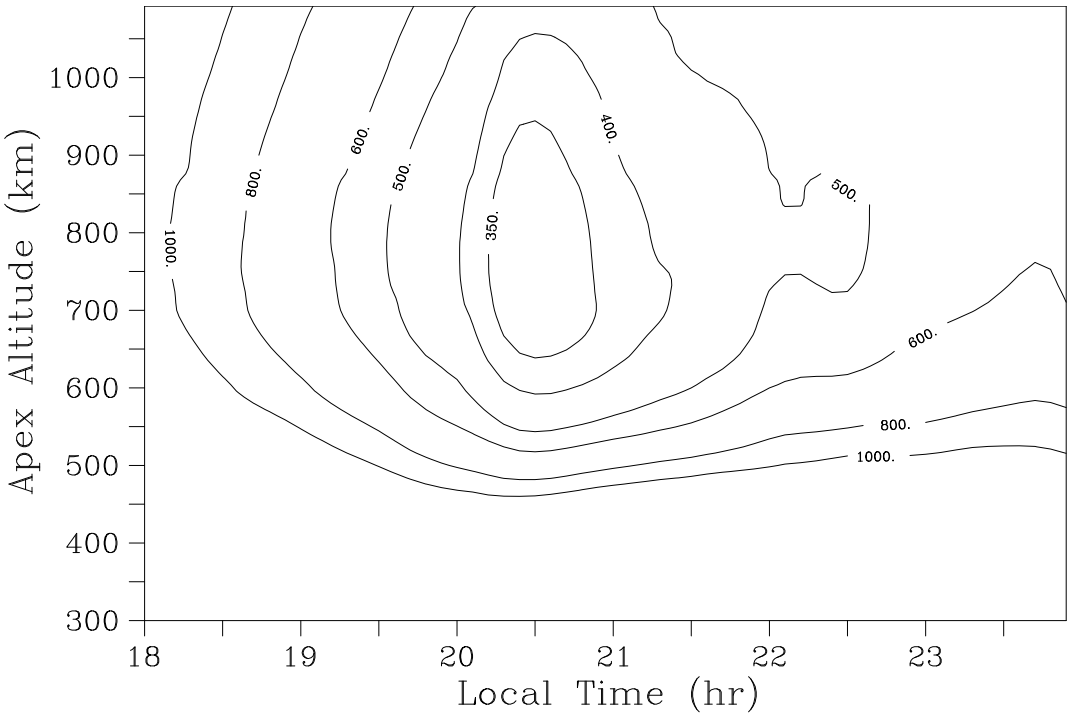

Figure A.3: Model run for January 26, 1980. Contours denote the velocity threshold arising from equating the last two terms in equation 1 (see text).

have characteristic spectral forms and give rise to characteristic radio scintillation spectra.

In the future, we hope to obtain additional data from satellites other than AE-E to expand this analysis. In particular, the impending launch of the C/NOFS satellite promises widespread availability of equatorial irregularity data, including vector plasma drifts, over a broad range of local times and magnetic apex altitudes. Furthermore, we can examine radio scintillation data for evidence of changes in the irregularity spectrum during spread F events when inertial regime flows are most likely. Finally, there is reason to believe that coherent scatter Doppler spectra received from scatter from irregularities in the inertial regime should have a pre-

dictable characteristic form [*Hysell and Shume*, 2002b]. These avenues of research will be pursued in the future.

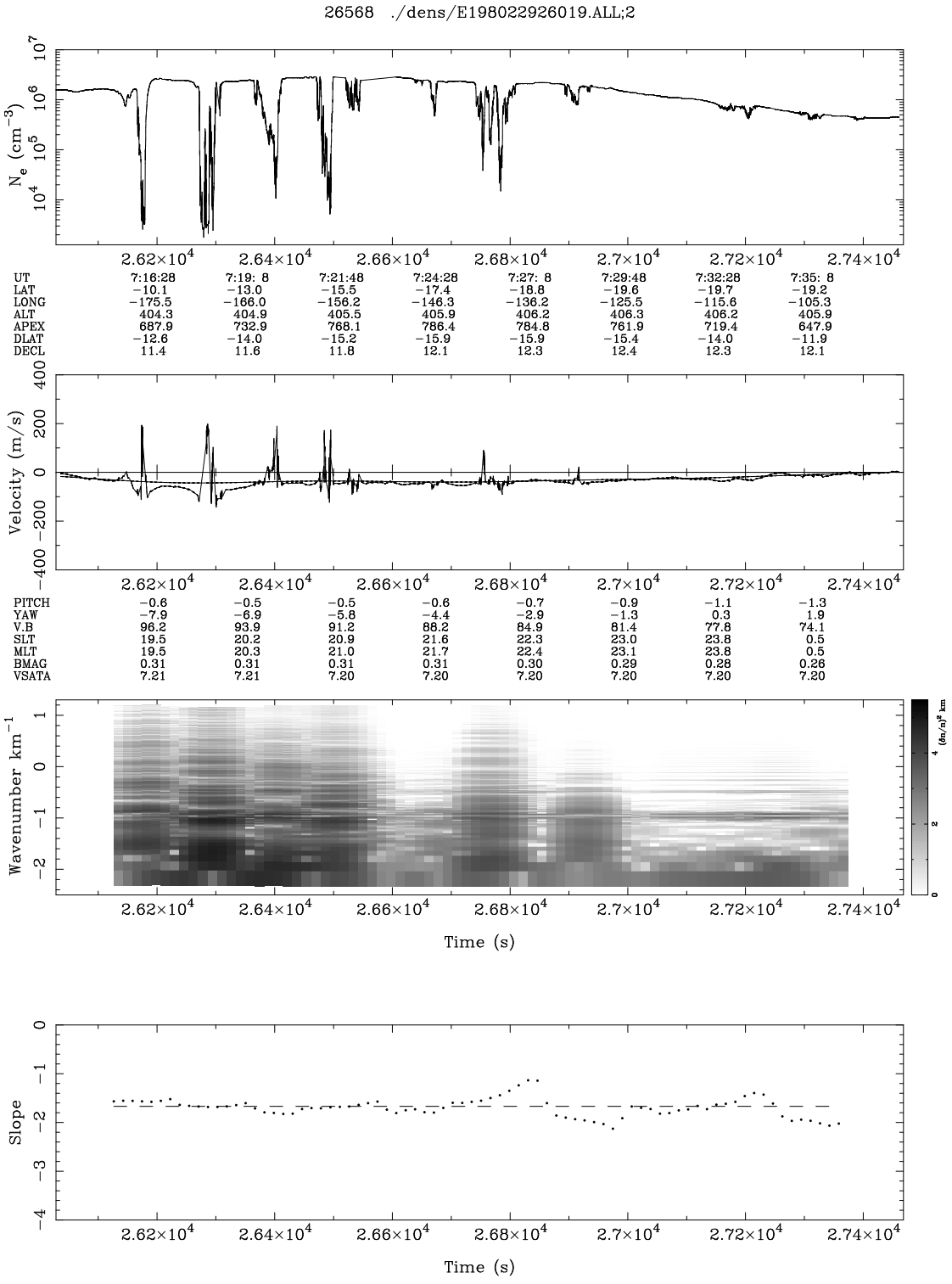

Figure A.4: *AE-E* satellite data for August 16, 1980.

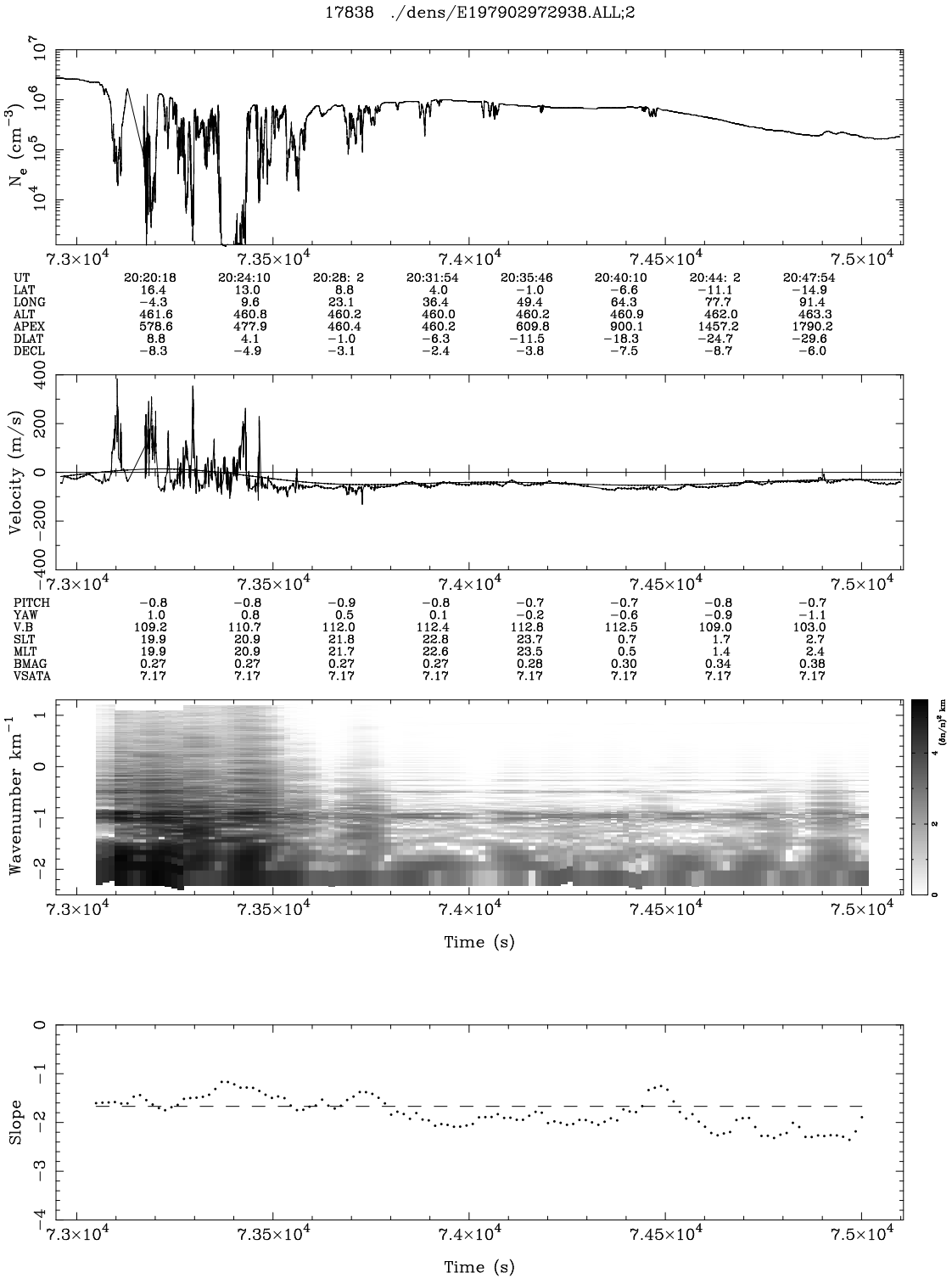

Figure A.5: *AE-E* satellite data for January 29, 1980.

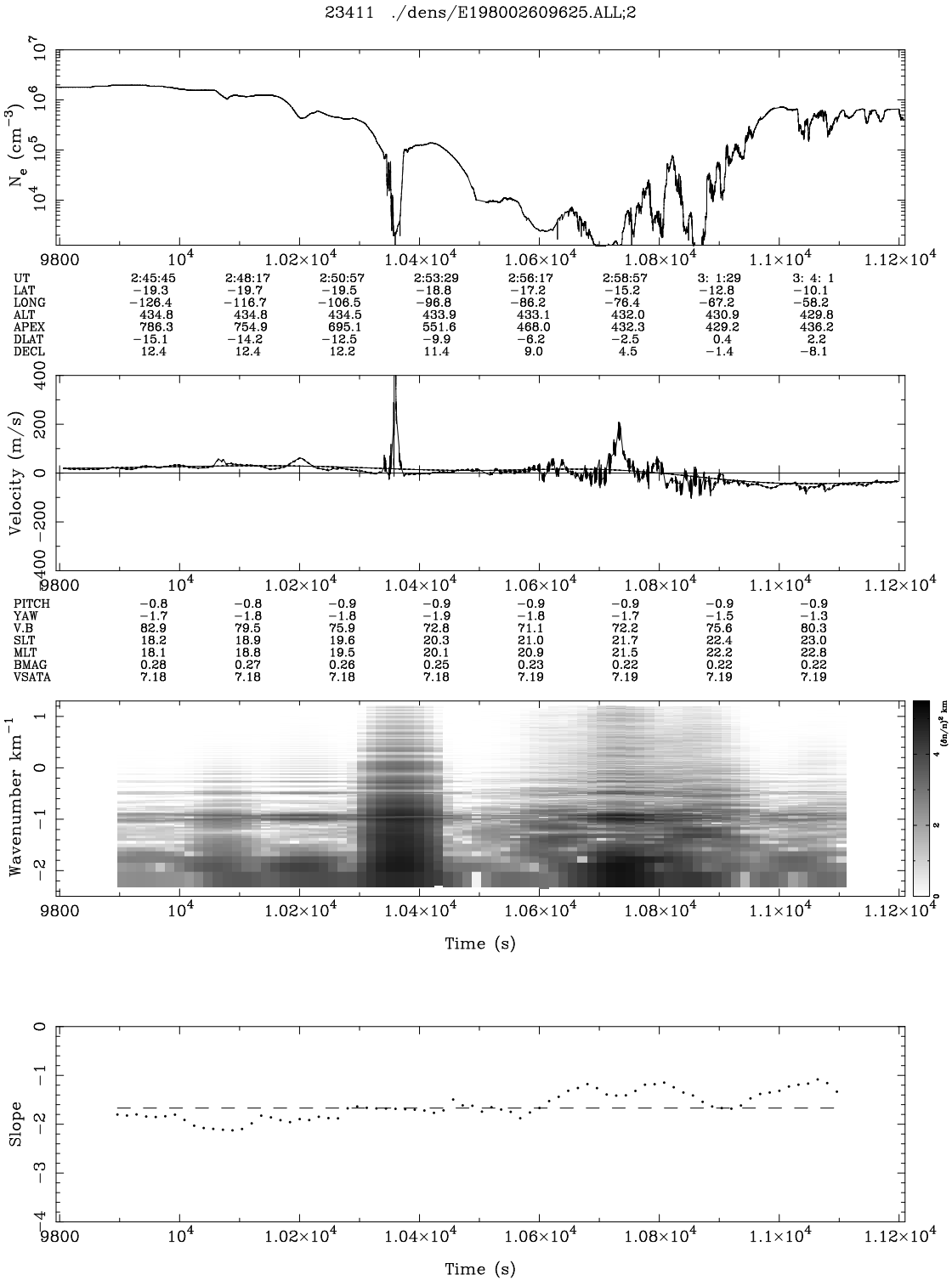

Figure A.6: *AE-E* satellite data for January 26, 1980.

BIBLIOGRAPHY

Adams, J. C., MUDPACK: Multigrid Software for Elliptic Partial Differential Equations, *http://www.scd.ucar.edu/css/software/mudpack/*, University Corporation for Atmospheric Research, Boulder. Co., 1998.

Aggson, T. L., W. J. Burke, N. C. Maynard, W. B. Hanson, P. C. Anderson, J. A. Slavin, W. R. Hogey, and J. L. Saba, Equatorial bubbles updrafting at supersonic speeds, *Journal of Geophysical Research*, *97*, 8581, 1992.

Appleton , E. V., Two Anomalies in the ionosphere, *Nature*, 157, 1946.

Balsley, B, B., Some characteristics of non two stream irregularities in the equatorial electrojet, *Journal of Geophysical Research*, *74*, 2333, 1969.

Balsley, B, B., Electric fields in the equatorial ionosphere: A review of techniques and measurements, *Journal of Atmospheric and Terrestrial Physics*, *35*, 1035, 1973.

Balsley, B, B., B. G. Fejer, and D. T. Farley, Blanc, Radar measurements of neutral winds and temperatures in the equatorial E region, *Journal of Geophysical Research*, *81*, A4, 1457, 1976.

Barton, C. E., International Geomagnetic Reference Field: The seventh generation, *Journal of Geomagnetism and Geoelectricity*, *49*, 123, 1997.

Bernard, R., and A. Spizzichino, Semi-diurnal wind and temperature oscillations in the E region observed by the Nancay incoherent scatter experiment, *Journal of Atmospheric and Terrestrial Physics*, *33*, 1345-1352, 1971.

Bernard, R., Tides in the E region observed by incoherent scatter over Saint Santin, *Journal of Atmospheric and Terrestrial Physics*, *36*, 1105 - 1120, 1974.

Bevington, P. R., *Data reduction and error analysis in the physical sciences*, McGraw Hill Book Company, New York, 1969.

Bilitza, D. (1990), International Reference Ionosphere 1990, *National Space Science Data Center 90-22*, Greenbelt, MD., 1990

Bilitza, D., K. Rawer, L. Bossy, and T. Gulyaeva, International Reference Ionosphere: - Past, present, future: I, Electron Density, *Advances in Space Research*, 13, no. 3, 1993.

Bilitza, D. (2001), International Reference Ionosphere 2000, *Radio Science*, 36, no. 2, 261-275, 2001.

Bittencourt, J. A., *Fundamentals of plasma physics*, 3^{rd} edition, J. A. Bittencourt, Sao Jose dos Campos, SP, Brazil, 2003.

Blanc, M. and A. Richmond, The ionospheric disturbance dynamo, *Journal of Geophysical Research*, 85, A4, 1669 - 1686, 1980.

Brekke, A., and C. Hall, Auroral ionospheric quiet summer time conductance, *Annales Geophysicae*, 6(4), 361-376, 1988.

Broche, P., M. Crochet, and J. Gagnepain, Neutral winds and phase velocity of the instabilities in the equatorial electrojet, *Journal of Geophysical Research*, *83*, 1145, 1978.

Budden, K. G., *Radio waves in the ionosphere*, Cambridge University Press, Cambridge, UK, 1961.

Buneman, O., Excitation of field aligned sound waves by electron streams, *Physical Review Letters*, 10, 285, 1963.

Chandra, H., H. S. S. Sinha, and R. G. Rastogi, Equatorial electrojet studies from rocket and ground measurements, *Earth Planet Space*, 52, 111-120, 2000.

Chapman, S. and R. S. Lindzen, *Atmospheric Tides: Thermal and gravitational*, Gordon and Breach/Science Publishers, New York, 1970.

Chau, J. L., and R. F. Woodman, Daytime vertical and zonal velocities from 150-km echoees: Their relevance to *F* region dynamics, *Geophysical Research Letters*, *31*, 2004.

Chen, F. F., *Introduction to plasma physics and controlled fusion*, Vol 1, Platinum Press, New York, 1984.

Costa, E., and M. C. Kelley, On the role of steepened structures and drift waves in equatorial spread *F*, *Journal of Geophysical Research*, *83*, 4359, 1978.

Devasia, C. V., and C. A. Reddy, Retrieval of east-west wind in the equatorial electrojet from local wind-generated electric field, *Journal of Atmospheric and Terrestrial Physics*, *57*, 11, 1233-1239, 1995.

Dougherty, J. P., and D. T. Farley, Ionospheric *E* region irregularities produced by nonlinear coupling of unstable plasma waves, *Journal of Geophysical Research*, 72(3), 895 - 901, 1967.

Drexler, J., *Convective* E *region irregularities at high latitude*, PhD Dissertation, University of Western Ontario, Canada, 2004.

Eccles, J. V., A simple model of low-latitude electric fields, *Journal of Geophysical Research*, 103, 26699 - 26708, 1998.

Eccles, J. V., Modeling investigation of the evening prereversal enhancement of the zonal electric field in the equatorial ionosphere, *Journal of Geophysical Research*, 103, A11, 26709 - 26719, 1998.

Fambitakoye, O., P. N. Mayaud, and A. D. Richmond, Equatorial Electrojet and regular daily variation S III, Comparision of observations with a physical model, *Journal of Atmospheric and Terresterial Physics*, 47, 8-10, 429-744, 1976.

Farley, D. T., A theory of electrostatic fields in a horizon tally stratified ionosphere subject to a vertical magnetic field, *Journal of Geophysical Research*, 64, 1225, 1959.

Farley, D. T., A theory of electrostatic fields in the ionosphere at nonpolar geomagnetic latitudes, *Journal of Geophysical Research*, 65, 869, 1960.

Farley, D. T., A plasma instability resulting in field-aligned irregularities in the ionosphere, *Journal of Geophysical Research*, 68, 6083, 1963.

Farley, D. T., Faraday rotation measurement using incoherent scatter, *Radio Science*, 4, 2, 143 - 152, 1969.

Farley, D. T. and B. B. Balsley, Instabilities in the equatorial electrojet, *Journal of Geophysical Research*, 78, 1, 227-239, 1973.

Farley, D. T., H. M. Ierkic, B. G. Fejer, Radar interferometry: A new technique for studying plasma turbulence in the ionosphere, *Journal of Geophysical Research*, 86, 1467 - 1472, A3, 1981.

Farley, D. T., Theory of Equatorial Electrojet Plasma Waves: New developments and current status, *Journal of Atmospheric and Terresterial Physics*, 47, 8-10, 429-744, 1985.

Farley, D. T., E. Bonelli, B. G. Fejer, and M. F. Larsen, The prereversal enhancement of the zonal electric field in the equatorial ionosphere, *Journal of Geophysical Research*, 94, 13723 - 13728, 1986.

Farley, D. T. and T. Hagfors, *Radar scatter probing of the ionospheric plasma*, Cornell Univeristy, Department of Electric and Computer Engineering, Ithaca, New York, 2004, a book in preparation.

Fejer, B. G. (1981), The equatorial ionosphere electric fields: a review, *Journal of Atmospheric and Terrestrial Physics*, 43, 377 - 386, 1981.

Fejer, B. G. (1991), Low latitude electrodynamic plasma drifts: a review, *Journal of Atmospheric and Terrestrial Physics*, 53, 677 - 693, 1991.

Fejer, B. G., D. T. Farley, B. B. Balsley, and R. F. Woodman, Vertical structure of the VHF backscattering region in the equatorial electrojet and the gradient drift instability*Journal of Geophysical Research*, *80*, 10, 1975.

Fejer, B. G., C. A. Gonzales, D. T. Farley, M. C. Kelley, and R. F. Woodman, Equatorial electric fields during magnetically disturbed conditions, 1, The effects of the interplanetray magnetic field, *Journal of Geophysical Research*, 84, 5797 - 5802, 1979.

Fejer, B. G. and M. C. Kelley, Ionospheric Irregularities, *Reviews of Geophysics and Space Physics*, 18, 2, 401-454, 1980.

Fejer, B. G., E. R. dePaula, R. A. Heelis, and W. B. Hanson, Global equatorial ionospheric vertical plasma drifts measured by the AE-E satellite, *Journal of Geophysical Research*, *100*, 5769, 1995.

Fesen, C. G., G. Crowley and R. G. Roble, Ionospheric effects at low latitude during the March 22, 1979, geomagnetic strom, *Journal of Geophysical Research*, 94, A5, 5405 - 5417, 1989.

Forbes, J. M. and R. S. Lindzen, Atmospheric Solar Tides and their electrodynamic effects-I The equatorial electrojet, *Journal of Atmospheric and Terrestrial Physics*, *38*, 897 - 910, 1976a.

Forbes, J. M. and R. S. Lindzen, Atmospheric Solar Tides and their electrodynamic effects-II The equatorial electrojet, *Journal of Atmospheric and Terrestrial Physics*, *38*, 911 - 920, 1976b.

Forbes, J. M., The equatorial electrojet, *Reviews of Geophysics and Space Physics*, *19*, 469-504, 1981.

Friedrich, M. and K. M. Torkar, FIRI: A semiempirical model of the lower ionosphere, *Journal of Geophysical Research*, 106, 21,409 - 21,418, 2001.

Fuller-Rowell, T. J., M. V. Codrescu, R. J. Moffett, and S. Quegan, Response of the thermosphere and ionosphere to geomagnetic stroms, *Journal of Geophysical Research*, 99, A3, 3893 - 3914, 1994.

Fuller-Rowell, T. J., M. V. Codrescu, H. Rishbeth, R. J. Moffett, and S. Quegan, On the seasonal response of the thermosphere and ionosphere to geomagnetic stroms, *Journal of Geophysical Research*, 101, A2, 2343 - 2353, 1996.

Fuller-Rowell, T. J., G. H. Millward, A. D. Richmond, and M. V. Codrescu, Storm-time changes in the upper atmosphere at low latitudes, *Journal of Atmospheric and Solar-Terresterial Physics*, 64, 1383 - 1391, 2002.

Gagnepain, J., M. Crochet, and A. D. Richmond, Comparion of equatorial electrojet models, *Journal of Atmospheric and Terrestrial Physics*, *39*, 1119, 1977.

Haerendel, G. and J. V. Eccles, The role of the equatorial electrojet in the evening ionosphere, *Journal of Geophysical Research*, 97, A2, 1181 - 1192, 1992.

Haerendel, G. J., V. Eccles, and S. Cakir, Theory of modeling the equatorial evening ionosphere and the origin of the shear in the horizontal plasma flow, *Journal of Geophysical Research*, 97, A2, 1209 - 1223, 1992.

Hanson, W. B., and R. A. Heelis, Techniques for measuring bulk gas motions from satellites, *Space Science Instrumentation*, *1*, 493, 1975.

Hanuise, C., M. Crochet, P. Gouin, and G. Ogubazghi, Radar observation of the equatorial counter-electrojet, *Annales Geophysicae*, 35,201-202, 1979.

Hargreaves, J. K., *The solar-terrestrial environment, an introduction to geospace*, Cambridge University Press, Cambridge, UK, first paperback edition, 1995.

Harper, R. M., R. H. Wand, C. J. Zamlutti, and D. T. Farley, *E* region ion drifts and winds from incoherent scatter measurements at Arecibo, *Journal of Geophysical Research*, *105*, 81, 1, 25 - 35, 1976.

Hassam, A. B., W. Hall, J. D. Huba, and M. J. Keskinen, Spectral characteristics of interchange instability, *Journal of Geophysical Research*, *91*, 13,513, 1986.

Hedin, A. E., Extension of the MSIS theromspheric model into the lower and middle atmosphere, *Journal of Geophysical Research*, *96*, 1159, 1991.

Heelis, R. A., Electrodynamics in the low and middle latitude ionosphere: a tutorial, *Journal Atmospheric and Solar-Terrestrial Physics*, *66*, 825 - 838, 2004.

Heelis, R. A., P. C. Kendall, R. J. Moffett, and D. W. Windle, Electrical coupling of the *E* and *F* regions and its effect on *F* region drifts and winds, *Planetary and Space Science*, *22*, 743 - 756, 1974.

Hysell, D. L., An overview and synthesis of plasma irregularities in equatorial spread *F*, *Journal of Atmospheric and Solar-Terrestrial Physics*, 62, 1037 - 1056, 2000.

Hysell, D. L., and J. Burcham, Ionospheric electric field estimates from radar observation of the equatorial electrojet Inferring, *Journal of Geophysical Research*, *105*, 2443, 2000.

Hysell, D. L., and J. L. Chau, Inferring E region electron density profiles at Jicamarca from Faraday rotation of coherent scatter, *Journal of Geophysical Research*, *106*, 30,371-30,380, 2001.

Hysell, D. L., J. L. Chau, and C. G. Fesen, Effect of large scale horizontal winds on the equatorial electrojet *Journal of Geophysical Research*, *107*, A8, SIA 27 (1-12), 2002.

Hysell, D. L., J. Chun, and J. L. Chau, Bottom-type scattering layers and equatorial spread *F*, *Annales Geophysicae*, *22*, 4061 - 4069, 2004.

Hysell, D. L., M. C. Kelley, W. E. Swartz, and D. T. Farley, VHF radar and

rocket observations of equatorial spread *F* on Kwajalein, *Journal of Geophysical Research*, *99*, 15,065, 1994a.

Hysell, D. L., C. E. Seyler, and M. C. Kelley, Steepened structures in equatorial spread *F*, 2, Theory, *Journal of Geophysical Research*, *99*, 8841, 1994b.

Hysell, D. L., and E. B. Shume, Electrostatic plasma turbulence in the topside equatorial F region ionosphere, *Journal of Geophysical Research*, 107, A10, 1269, doi:1029/2001JA000227, 2002a.

Hysell, D. L., and E. B. Shume, Plasma turbulence in topside equatorial spread F, *EGS, Nice, France* , April 22-26, 2002b.

Jahn, J. M., and J. LaBelle, Rocket measurements of high-altitude spread *F* irregularities at the magnetic dip equator, *Journal of Geophysical Research*, *103*, 23,427, 1998.

Kelley, M. C., and E. Ott, Two-dimensional turbulence in the equatorial spread *F.*, *Journal of Geophysical Research*, *83*, 4369, 1978.

Kelley, M. C, B. G. Fejer, and C. A. Gonzales, An explanation for anomalous equatorial ionospheric electric fields associated with a northward turning of the interplanetary magnetic field, *Geophysical Research Letters*, 6, 301-304, 1979.

Kelley, M. C., *The Earth's Ionosphere: Plasma Physics and Electrodynamics*, Academic Press, San Diego, 1989.

Kintner, P. M., and C. E. Seyler, The status of observations and theory of high-latitude ionospheric and magnetospheric plasma turbulence, *Space Science Review*, *41*, 91, 1985.

Kraichnan, R. H., Inertial ranges in two-dimensional turbulence, *Physics of Fluids*, 10, 1417, 1967.

Kudeki, E., D. T. Farley, B. G. Fejer, and H. M. Ierkic, Interferometer studies of equatorial *F* region irregularities and drifts, *Geophysical Research Letters*, 8, 4, 377 - 380, 1981.

Kudeki, E., D. T. Farley, and B. G. Fejer, Long wavelength irregularities in the equatorial electrojet, *Geophysical Research Letters*, 9, 6, 684-687, 1982.

Kudeki, E., D. T. Farley, B. G. Fejer, and C. Hanuise, The Condor equatorial electrojet campaign: Radar results, *Journal of Geophysical Research*, 92, A12, 13561-13577, 1987.

Larsen, M. F., A shear instability seeding mechanism for quasiperiodic radar echoes, *Journal of Geophysical Research*, *105*, A11, 24,931 - 24,940, 2000.

Larsen, M. F., Winds and shears in the mesosphere and lower thermosphere: Results from four decades of chemical release wind measurements, *Journal of Geophysical Research*, *107*, A8, SIA 28 (1-14), 2002.

Larsen, M. F., and C. D. Odom, Observation of altitudinal and latitudinal E-region neutral wind gradients near sunset at the magnetic equator, *Geophysical Research Letters*, *24*, 1711-1714, 1997.

Lomb, N. R., Least-squares frequency analysis of unequally spaced data, *Astrophysics and Space Science*, *39*, 447, 1976.

Luhmann, J. G., Ionospheres, In *Introduction to Space Physics, M. G. Kivelson and C. T. Russell (eds), Cambridge University Press, Cambridge*, 183 - 202, 1995.

Martyn, D. F., Theory of height and ionization density changes at the maximum of a Chapman-like region, taking account of ion production, decay, diffusion, and total drift, *Proceedings of the Cambridge Conference*, p 254, Physical Society, London, 1955.

McDaniel, R. D., *Plasma turbulence in the equatorial ionospheric* F *region*, Ph.D. dissertation, Clemson University, Clemson, South Carolina, 1998.

McDaniel, R. D., and D. L. Hysell, Models and DE II observations of inertial-regime irregularities in equatorial spread *F*, *Journal of Geophysical Research*, *102*, 22,233, 1997.

Nicolet, M., The collision frequency of electrons in the ionosphere, *Journal of Atmospheric and Terrestrial Physics*, *3*, 200, 1953.

National Space Science Data Center, MSIS-E-90 Atmosphere Model, *http://nssdc.gsfc.nasa.gov/space/model/models/msis.html*, National Space Science Data Center (NSSDC), Greenbelt, MD, 1990.

National Space Science Data Center, International Reference Ionosphere: - IRI-2001, *http://nssdc.gsfc.nasa.gov/space/model/models/iri.html*, National Space Science Data Center (NSSDC), Greenbelt, MD, 2001.

National Space Science Data Center, IGRF Geomagnetic Field Model, *http://nssdc.gsfc.nasa.gov/space/model/models/igrf.html*, National Space Science Data Center (NSSDC), Greenbelt, MD, 2002.

Ott, E., Theory of Rayleigh-Taylor bubbles in the equatorial ionosphere, *Journal of Geophysical Research*, *83*, 2066, 1978.

Peddie, N. W., and E. B. Fabiano, A proposed international geomagnetic reference field for 1965-1985, *Journal of Geomagnetism and Geoelectricity*, *34*, 357, 1982.

Pingree, J. E., *Incoherent scatter measurements and inferred energy fluxes in the equatorial* F *region ionosphere*, PhD Dissertation, Cornell University, Ithaca, NY, USA, 1990.

Pfaff, R. F., M. C. Kelley, E. Kudeki, B. G. Fejer, and K. D. Baker, Electric field and plasma density measurements in the strongly driven daytime equatorial electrojet, 2, the unstable layer and gradient drift waves, *Journal of Geophysical Research*, *92*,13,578, 1987.

Ratcliffe, J. A., *The Magneto-ionic theory and its application to the ionosphere*, Cambridge University Press, Cambridge, UK, 1959.

Reber, C. A., C. E. Trevathan, R. J. McNeal, and M. R. Luther, The Upper Atmosphere Research Satellite (UARS) Mission, *Journal of Geophysical Research*, *98*, D6, 10,643 - 10,647, 1993.

Reddy, C. A. and C. V. Devasia, Height and altitude structure of electric fields and currents due to local eat-west winds in the equatorial electrojet, *Journal of Geophysical Research*, 86, 5751 - 5767, 1981.

Reddy, C. A, B. T. Vikramkumar, and K. S. Viswanathan, Electric fields and currents in the equatorial electrojet deduced from VHF radar observations, I, A method of estimating electric fields, *Journal of Atmospheric and Terrestrial Physics*, *49*, 183, 1987.

Richmond, A. D., Numerical model of the equatorial electrojet, *Tech. Rep.*

AFCRL-72-0668, ERP 421, Air Force Cambridge Res. Lab. Hanscom AFB, Bedford, Mass, 1972.

Richmond, A. D., Equatorial electrojet-I. Development of a model including winds and instabilities, *Journal of Atmospheric and Terresterial Physics*, *35*, 6, 1083-1103, 1973a.

Richmond, A. D., Equatorial electrojet, II, Use of the model to study the equatorial ionosphere, *Journal of Atmospheric and Terrestrial Physics*, 35, 1103-1118, 1973b.

Richmond, A. D., Modeling equatorial ionospheric electric fields, *Journal of Atmospheric and Terrestrial Physics*, 57, 1103 - 1115, 1995.

Richmond, A. D., and S. Matsushita, Thermospheric response to magnetic storm, *Journal of of Geophysical Research*, 80, 19, 2839 - 2850, 1975.

Rishbeth, H., Polarization electric fields produced by winds in the equatorial F region, *Planetary and Space Science*, *1957*, 1357-369, 1971.

Rishbeth, H., The ionospheric E layer and F layer dynamos - a tutorial review, *Journal of Atmospheric and Solar-Terrestrial Physics*, *59*, 1873-1880, 1997.

Rogister, A., and N. D'Angelo, Type II irregularities in the electrojet, *Journal of Geophysical Research*, *75*, 3879 - 3887, 1970.

Ronchi, C., and Sudan, R. N., Effect of short-scale turbulence on kilometer wavelength irregularities in the equatorial electrojet, *Journal of Geophysical Research*, *95*, A1, 189-200, 1990.

Sastri, J. H., Equatorial electric fields of ionospheric disturbance dynamo origin, *Annales Geophysicae*, 6(6), 635 - 644, 1988.

Sato, T., Neutral winds and electrojet irregularities, *Journal of Geophysical Research*, *80*, 19, 2835-2838, 1975.

Scannapieco, A. J., and S. L. Ossakow, Nonlinear Equatorial Spread F, *Geophysical Research Letters* , *3*, 451, 1976.

Scherliess, L. and B. G. Fejer, Storm time dependence of equatorial disturbance dynamo zonal electric fields, *Journal of Geophysical Research*, 102, A11, 24037 - 24046, 1997.

Scherliess, L., and B. G. Fejer, Radar and satellite global equatorial F region vertical drift model, *Journal of Geophysical Research*, *105*, 6829, 1999.

Schunk, R. W., and J. C. G. Walker, Theoretical ion densities in the lower ionosphere, *Planetary and Space Science*, *21*, 1875, 1973.

Schunk, R. W., and A. F. Nagy, *Ionospheres: Physics, Plasma Physics and Chemistry*, Cambridge University Press, Cambridge, UK, 2000.

Shume, E. B. and D. L. Hysell, Spectral analysis of plasma drift measurements from the *AE-E* satellite: evidence of an inertial subrange in equatorial spread *F*, *Journal of Atmospheric and Solar-Terrestrial Physics*, *66, 57 - 65*, 2004.

Shume, E. B, D. L. Hysell, and J. L. Chau, Electron density profiles in the equatorial E region ionosphere derived from a bistatic coherent scatter radar experiment in Perú, *Geophysical Research Letters*, *32, L01107, doi:10.1029/2004GL021715*, 2005a.

Shume, E. B., D. L. Hysell, and J. L. Chau, Zonal wind profiles in the equatorial electrojet derived from phase velocities of type II radar echoes, *Journal of Geophysical Research*, *110, A12308, doi:10.1029/2005JA011210*, 2005b.

Spiro, R. W., R. A. Wolf, and B. G. Fejer, Penetration of high-latitude electric field effects to low latitudes during SUNDIAL 1984, *Annales Geophysicae*, 6(1), 39-49, 1988.

St.-Maurice, J. P., A unified theory of anomalous resistivity and Joule heating effects in the presence of ionospheric *E* region irregularities, *Journal of Geophysical Research*, *92*, A5, 4533-4542, 1987.

St.-Maurice, J. P., Wave-induced diffusion in the turbulent *E* region, In *Polar cap dynamics and High latitude turbulence: SPI conference proceedings and reprint series, T. Chang, G. B. Crew and J. R. Jasperse (eds), Scientific Publishers, Cambridge, Mass*, No. 8, 323 - 338, 1988.

Sudan, R. N., J. Akinrimisi, and D. T. Farley, Generation of small-scale irregularities in the equatorial electrojet, *Journal of Geophysical Research*, 78, 240, 1973.

Sudan, R. N., and M. J. Keskinen, Theory of strongly turbulent two-dimensional convection of low-pressure plasma, *Physics of Fluids*, 22, 2305, 1979.

Sudan, R. N., Unified theory of type I and type II irregularities in the equatorial electrojet, *Journal of Geophysical Research*, *88*, 4853, 1983a.

Sudan, R. N., Nonlinear theory of type I irregularities in the equatorial electrojet, *Geophysical Research Letters*, *10*, 983, 1983b.

Sudan, R. N. and M. J. Keskinen, Theory of strongly turbulent two dimensinonal convection of low-pressure plasma, *Physics of Fluids*, *22*, 2305, 1979.

Sugiura, M. and J. C. Cain, A model of the equatorial electrojet, *Journal of Geophysical Research*, 71, 1869 - 1877, 1966.

Trost, T. F., Electron Concentrations in the E and upper D Region at Arecibo, *Journal of Geophysical Research*, 94, 6, 1979.

Untiedt, J., A model of the equatorial electrojet involving meridional current, *Journal of Geophysical Research*, 72, 5799 - 5810, 1967.

Woodman, R. F., Vertical velocities and east-west electric fields at the magnetic equator, *Journal of Geophysical Research*, 75, 6249 - 6259, 1970.

Woodman, R. F., and C. La Hoz, Radar observations of F region equatorial irregularities, *Journal of Geophysical Research*, 81, 5447, 1976.

Yeh, H. C., S. Y. Su, and R. A. Heelis, Storm time plasma irregularities in the pre-dawn hours observed by the low-latitude ROCSAT-1 satellite at 600 km altitude, *Geophysical Research Letters*, *28*, 685, 2001.

Zargham, S., *Numerical simulations of the ionospheric interchange instability*, Ph.D. Dissertation, Cornell University, Ithaca, New York, 1988.

Zargham, S., and C. E. Seyler, Collisional interchange instability, 1, Numerical simulations of intermediate-scale irregularities, *Journal of Geophysical Research*, *92*, 10,073, 1987.

Zargham, S., and C. E. Seyler, Collisional and inertial dynamics of the ionospheric interchange instability, *Journal of Geophysical Research*, *94*, 9009, 1989.